Electrical Transport in Thin Films of Doped Silicon Nanocrystals

A THESIS
SUBMITTED TO THE FACULTY OF THE GRADUATE SCHOOL
OF THE UNIVERSITY OF MINNESOTA
BY

Ting Chen

IN PARTIAL FULFILLMENT OF THE REQUIREMENTS
FOR THE DEGREE OF
DOCTOR OF PHILOSOPHY

Uwe R. Kortshagen, Advisor

June, 2015

Acknowledgements

I have many people to thank for their help along the way to my degree. Without their efforts, this thesis would not have been possible.

First of all, I want to sincerely thank my excellent advisor, Prof. Uwe Kortshagen, for giving me guidance and support, and allowing me the freedom to explore my own ideas in this PhD research.

I need to especially thank Prof. Boris Shklovskii, for laying the theoretical foundation for my experimental work, offering me inspiration, advice and encouragement during our collaboration. This is a precious learning experience, it is my great honor to work with him.

I want to acknowledge the help I have received from my collaborators, in particular Brian Skinner and Konstantin Reich, who have made extremely important contributions to the theory part in my thesis, and Nicolaas Kramer, who has nicely provided doped nanoparticles for my experiments. They have been very helpful collaborators, I wish them best luck for the future.

I thank Prof. Dan Frisbie, for kindly giving me access to his lab, where I have performed the majority of my electrical measurements, and Prof. Eray Aydil, for sharing a few of his instruments, Prof. Stephen Campbell and Prof. Chris Leighton for stimulating discussions in my research.

Also I want to thank all my colleagues and collaborators. Rebecca Anthony, for leading me into the plasma synthesis of nanocrystals, David Rowe, for helping with initial electrical measurements, Lance Wheeler, Richard Liptak, Jihua Yang, Song Guo for

their guidance and encouragement during my first few years in the group, and all my other colleagues and collaborators, Kaiyuan Cheng, Andrew Wagner, Elijah Thimsen, Zuoti Xie, Xin Zhang, Mengqun Li, Ryan Gresback, Ben Greenberg, Brian Benton and Katelyn Schramke. Special thanks to Jeslin Wu, for all the invaluable support and friendship.

I would like to thank the research scientists, Jason Myers, Jacob Warner and Nick Seaton for their substantial assistance with characterization of tiny nanoparticles in the Characterization Facility, Rick Knurr for his efforts with elemental analysis and also engineers in the Nanofabrication Center for their help with equipment.

Most importantly, I would like to thank my husband Wei Xie for his continuous support through the years that we have been in Graduate School. Thanks for pushing me farther than I thought I can go. I deeply appreciate everything he has done for me, I am very lucky to have him by my side. I am also grateful to all my friends and family for helping me survive all the stress from these years and not letting me give up.

Abstract

Colloidal semiconductor nanocrystals (NCs) have shown great potential for thin-film optoelectronics, such as solar cells and light emitting diodes (LEDs), due to their size-tunable electronic properties and solution processability. Significant progress has been made in developing synthetic methods to prepare high quality NCs, achieving controllable doping, and integrating NCs into high performance electronic devices. Most electronic applications rely on the electrical conduction through NC films, therefore, fundamental understanding of the carrier transport in NC films is required to further improve device performance and provide guide for future device design.

My research is inspired by the successful achievement of a highly efficient LED with hydrosilylated Si NCs as the emissive layer. To better understand the electrical conduction in the Si NC system, a systematic study of the temperature and electric-field dependence of the film conductivity is performed. It shows that the conductivity of the Si NC film is limited by the ionization of rare NCs containing donor impurities and the carrier transport follows nearest neighbor hopping. The Si NCs are inherently doped with a very small concentration (estimated to be $\sim 10^{15}$ cm^{-3}) of impurities. This is also the first study of carrier transport in a lightly doped NC system, and results obtained in this work can apply to other NC materials as well. The organic ligands used to passivate NC surface are necessary to achieve strong photoluminescence, however, they inhibit the carrier transport due to the resulting large tunneling barrier between neighboring NCs. The localization length estimated from the temperature data in the high electric field regime is about 1 nm. In addition, the activation energy required for conduction also depends on the surrounding medium of NCs, the electrical conduction can be improved by reducing the activation energy through engineering of the matrix of NC arrays.

Doping is critical to enable electrical transport in semiconductor NC films which are otherwise insulating materials. Significant efforts have been made to intentionally introduce substitutional impurities into the NCs, however, only a few attempts have succeeded. One is controllable doping with phosphorus (P) in Si NCs synthesized from a nonthermal plasma gas-phase method. This NC system provides a platform for studying the doping effects on the electronic properties of NCs. In contrast to the Si NCs lightly

doped with inherent impurities, the intentional doping with P can easily achieve heavily doped NCs so that each Si NC is metallic. Efros-Shklovskii variable range hopping (ES-VRH) is observed in dense films of P-doped, ligand-free spherical Si NCs over a wide range of doping concentration. The localization length increases with increasing doping concentration and exceeds the diameter d of a NC, indicating the approach to the metal-insulator transition (MIT) in the NC film. A theoretical criterion is developed to predict the critical doping concentration (n_c) for the MIT in a NC film, and $n_c = 9\times10^{20}$ cm^{-3} for Si NCs under study. It reasonably explains a doping-dependent localization length at doping concentration lower than 3×10^{20} cm^{-3} as observed in experiments. Additionally, by varying the separation δ between NCs through controlled oxidation, the localization length ξ decreases with increasing δ as $\xi \simeq ad/\delta$ in agreement with the cotunneling theory.

Boron (B) doping has also been achieved in the plasma synthesis method, and the electrical properties have shown strong dependence on the surface treatment since most B atoms are sitting on the NC surface. In dense films of B-doped Si NCs, the carrier transport still exhibits ES-VRH conduction but the localization length is doping-independent. The highest doping concentration achieved in this system is actually close to the theoretical critical doping concentration for the MIT in NC films, however, the expected divergence of the localization length does not occur. It is proposed that the degeneracy of conduction band minima or valence band maxima plays a key role in the carrier transport of NC films. Therefore, the hole transport can be completely different from the electron transport in Si NC films. The critical doping concentration derived for P-doped Si NCs cannot be applied to B-doped Si NCs. Moreover, the air stability of Si NCs is significantly affected by the doping. A modified atomic layer deposition (ALD) method is developed to infill B-doped Si NC films and excellent air stability is obtained with a few nanometers coating with alumina.

In summary, this thesis focuses on the electrical transport in thin films of doped Si NCs, which are synthesized from a nonthermal plasma gas phase method. Both of inherent and intentional doping have been investigated, and the pictures for carrier transport physics from light doping to heavy doping have been illustrated. This work explores the doping effects on the electrical properties of Si NCs, and also provides a roadmap for the electrical conduction in NC films over a wide range of doping concentration.

Contents

List of Tables

List of Figures

Chapter 1

Introduction

1.1 Research motivation

Colloidal semiconductor nanocrystals (NCs) have emerged to be promising candidates for applications in electronics[1], optoelectronics[2,3], and thermoelectrics[4], because of their size-tunable optical and electrical properties, and low-cost solution-based processing techniques. For most electronic applications, conducting thin films assembled from quantum confined individual NCs are required. To preserve the tunability of the electronic structure, the size of NCs needs to remain sub-10 nm. On the other hand, strong coupling and high carrier concentration are necessary to achieve useful conductivity in the NC films. This leads to two challenging topics in NCs: one is surface engineering to realize close-packed NC solids; the other one is doping of NCs to reach high carrier concentration.

Depending on synthetic methods, strategies for surface engineering and doping in NCs can be significantly different. Group II-IV and IV-VI metal-based NCs, synthesized from well-established wet chemistry synthesis method, are usually capped with long-chain organic ligands, since they serve to control the reactivity of precursors and provide steric barrier to agglomeration. Although these organic ligands play an important role in the wet chemistry synthesis of NCs and the formation of stable colloids for thin film fabrication, their insulating nature and the resulting large interparticle distance ($\sim$ 1 nm) dramatically hinder the carrier transport in the NC films[1,5]. Thus ligands

exchange is necessary to replace the native long-chain organic ligands with shorter organic or inorganic ligands, and this exchange process can be performed in a NC thin film or even in a NC solution[5–7]. Therefore, strong coupling in NC films can be achieved. Considerable efforts have been made to introduce electronic impurities into NCs, however, little progress has been achieved even after decades of research, primarily due to the synthetic challenge of incorporating an impurity into a nanoscale particle during relatively low-temperature ($\sim$ 300 °C) wet chemistry synthesis[8]. Instead, other doping strategies, such as remote doping, electrochemical doping and stoichiometric inbalance doping, have been developed in Cd/Pb chalcogenide NCs synthesized from the wet chemistry method.

On the other hand, gas phase methods are more favorable to synthesize group IV NCs, typically for Si NCs[9–11], because of high crystallization temperature. Since the first observation of efficient photoluminescence from nanoscale Si[12,13], Si NCs have attracted substantial interest in optoelectronic applications. Compared with group II-VI and IV-VI metal-based NCs which raise concerns over availability and toxicity, Si is an important alternative with wide abundancy and low toxicity. Among a number of gas phase synthesis methods, nonthermal plasmas have become an attractive technique to produce high-quality Si NCs[14]. The surface of as-produced NCs largely depends on the precursors and further surface treatment. For instance, Si NCs made from silane are usually terminated with H atoms due to excess H from SiH_4[15]. These NCs can be directly assembled into films using a supersonic gas jet to accelerate and impact NCs onto substrates[16]. Moreover, post-synthesis surface treatment can be performed to attach organic ligands and make colloidal NCs which are compatible with solution-based processes, such as spin-coating, spray coating, roll-to-roll printing, etc. Alkenes are common ligands used for Si NCs. They not only provide colloidal stability, but also passivate surface defects. Si NCs with ensemble photoluminescent quantum yield higher than 60% were achieved with 1-dodecene passivation[17]. Furthermore, hybrid organic-NC light emitting diodes with external quantum efficiency approaching 9% were fabricated from these Si NCs[18]. Although excellent surface passivation can be provided by alkenes, they are very insulating and most other materials offer lower barriers for electrical transport[19]. In addition, the attachment of alkenes forms Si-C covalent bonds

through hydrosilylation reaction[20], preventing further surface manipulation. More versatile NC surface has been realized using precursors containing Cl, such as $SiCl_4$. With Cl termination, NCs can be directly dispersed into solvents to form stable colloids and improved electrical performance has been observed in the films cast from these NC colloids[21,22]. Doping is also different in group IV NCs. The doping strategies developed in group II-VI and IV-VI NCs cannot be applied to Si NCs due to completely different NC surface. In contrast, some progress has been made in the electronic impurity doping accomplished in the plasmas by feeding gases containing dopants, such as phosphine (PH_3) or diborane (B_2H_6). By varying the flow rates of dopant gases, controllable doping has been achieved in Si NCs[23]. It is noted that the nonthermal plasma method can achieve much higher doping concentration in the NCs than the wet chemistry method. For example, more than ~ 50 electrons per NC can be easily obtained in P-doped Si NCs[23] while the highest doping concentration reported for CdSe NCs is 6 electrons per NC in an electrochemical cell[24]. At such a high doping concentration, the approach to the metal-insulator transition (MIT) in the NC arrays is possible.

Although there are a number of studies directed towards the electrical transport in NC solids, the effects of impurity doping still remains unexplored due to a lack of good NC system with tunable doping concentration of impurities. In this thesis work, we investigate the electrical transport in doped Si NCs from a small doping concentration with number of donors per NC $\nu \ll 1$ to a large doping concentration with $\nu \gg 1$. Our goal is to understand the doping effects on the electrical properties in NC systems. Different transport mechanisms have been found in different doping regimes, and the approach to the MIT is observed at $\nu \simeq 50$.

In the lightly doped Si NCs, we present, for the first time, a complete picture of the donor/acceptor ionization process in the NCs and illustrate the role played by temperature and electric field in this process. This work represents an important demonstration of the applicability of conventional ideas from bulk semiconductors, including Pool-Frenkel optimization and cold ionization, in a new context. These concepts have never been applied to the study of transport in NC arrays. We clearly demonstrate their effectiveness for describing these systems and this allows us to provide deeper insights into the physics of charge transport in NC systems.

In the heavily doped Si NCs, we address the fundamental question: what is the

condition for the MIT in a NC film? We develop a theory that gives the criterion for the MIT in NC films and also verify it from the electrical transport study in P-doped, ligand-free Si NCs over a wide range of doping concentration. This is the first theory developed to describe the criterion for the MIT in semiconductor NC systems. Also, this is the first time to experimentally observe a doping-dependent localization length which exceeds the diameter of a NC above a certain doping concentration. Additionally, B-doped Si NCs exhibit significantly different electrical behavior compared with P-doped Si NCs. We found that the dopant location plays a key role. Doping also affects the oxidation of Si NCs, and the air stability issue can be easily solved by coating a thin layer of alumina through atomic layer deposition method.

Overall, this is a fundamental work on the relationship between material structure and electrical properties, and it contributes to the understanding of the physics of electrical transport in doped NCs. The most important result from this thesis work can be summarized through the dependence of localization length on the doping concentration in NCs as shown in Figure 1.1. In the lightly doped Si NCs, terminated with alkyl ligands, the localization length is about 1 nm. The carrier transport in this system is limited by the ionization of the few donors and nearest neighbor hopping has been observed. In the P-doped Si NCs, packed in dense films, the localization length increases steeply with increasing doping concentration and NC films exhibit the approach to the MIT. A theoretical critical doping concentration for the MIT $n_c = 9 \times 10^{20}$ cm^{-3} is given based on the model that donors are randomly distributed inside the NCs. Our experimental results reasonably agree with this theoretical prediction. In the B-doped Si NCs, the localization length does not have a strong monotonic dependence on the doping concentration, which is still poorly understood. The system of B-doped Si NCs is completely different from P case. The doping mechanism is probably different from conventional substitutional doping. Moreover, the carrier type can also change the transport picture. Efros-Shklovskii variable range hopping has been observed in P- and B-doped Si NCs over the wide range of doping concentration, consistent with the theoretical studies for the electrical transport in doped NCs.

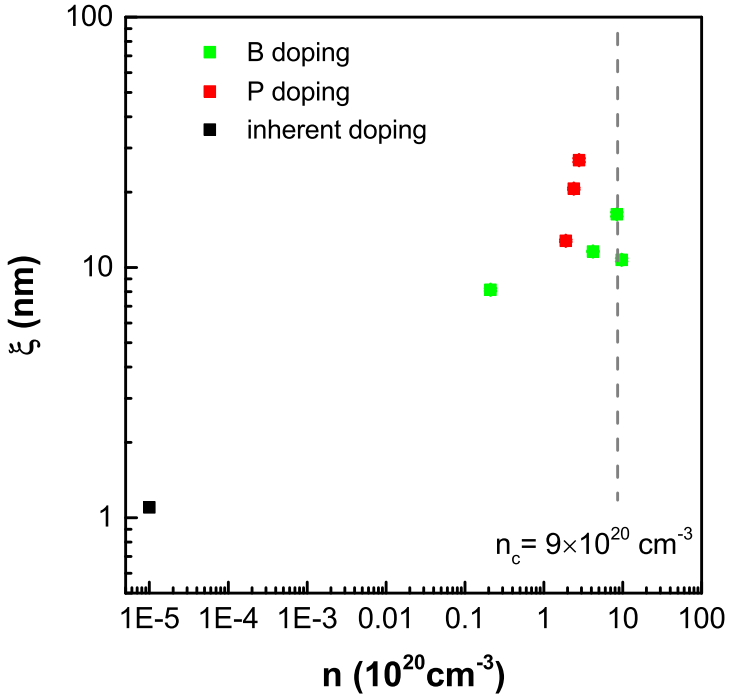

Figure 1.1: The dependence of localization length ξ on the doping concentration n in Si NCs. Inherent doping refers to the alkyl-ligand-terminated Si NCs which are unintentionally and lightly doped. The localization length in this system is about 1 nm, which is close to the value reported in literature for CdSe NC system[24]. In P-doped Si NCs, the localization length increases with increasing doping concentration, and exhibits approaching to the MIT. The dash line represents the the critical doping concentration for the MIT $n_c = 9 \times 10^{20}$ cm^{-3}, which is predicted from the theory based on NC systems with dopants randomly distributed inside the NC. The doping concentration in B-doped Si NCs already crosses the critical doping concentration, but no divergence of ξ occurs. The system of B-doped Si NCs is completely different from P-doped Si NCs in terms of carrier type and the doping mechanism. Therefore, the critical doping concentration developed in P-doped Si NCs does not apply to the B case. A new theory is needed.

1.2 Outline for this research

In this thesis work, we focus on the electrical transport in thin films of doped Si NCs synthesized from a nonthermal plasma gas phase method. Depending on the average number (ν) of dopants per NC, doped Si NCs are divided into two groups: lightly doped with doping level $\nu \ll 1$ and heavily doped with doping level $\nu > 1$. Light doping in Si NCs is achieved from inherent doping during synthesis while P and B atoms are intentionally introduced to realize heavy doping in Si NCs.

- Chapter 2 gives an introduction for the electrical transport in NC solids and illustrates the importance of surface engineering and doping in NCs to achieve conductive NC solids.

- Chapter 3 briefly describes the nonthermal plasma synthesis of Si NCs and the surface passivation via hydrosilylation reaction to achieve highly efficient photoluminescence. Lightly doped Si NCs were produced from this reactor and these particles have been successfully integrated into hybrid organic-NC based LEDs with high external quantum efficiency.

- Chapter 4 investigates the electrical transport in lightly doped Si NCs. Temperature- and electric-field-dependent conductance is examined in this chapter and a phase diagram is presented to reveal the carrier transport mechanisms in different regimes of temperature and electric field. This chapter is adapted from a publication in Journal of Physical Chemistry C[25] entitled: "Carrier Transport in Films of Alkyl-Ligand-Terminated Silicon Nanocrystals". Wei Xie, Brian Skinner, Boris Shklovskii and Uwe Kortshagen are co-authors on this work. Wei helped with preliminary low temperature experiments, and Brian and Boris developed the transport model to interpret the transport data.

- Chapter 5 studies the P doping effects on the electrical properties in Si NCs. This work is inspired by the previous study on lightly doped Si NCs. The carrier transport in heavily P-doped Si NCs follows a different conduction mechanism and the carriers become more delocalized with increasing the doping concentration, indicating the approach to the MIT. A theoretical model is developed to predict the MIT in NC solids and the results agree well with our experimental

observations. A manuscript entitled: "How Many Electrons Make Semiconductor Nanocrystal Films Metallic?" is under consideration. Konstantin Reich and Han Fu contributed to the theoretical part, Nicolaas Kramer provided the P-doped Si NCs used in the work, Boris Shklovskii and Uwe Kortshagen are also co-authors on this work.

- Chapter 6 continues with B doping effects on the electrical properties and addresses the air stability issue in Si NC films. The electrical properties of B-doped Si NCs strongly depend on the surface treatment since most B atoms are located on the NC surface. A postsynthesis approach is employed to improve the carrier transport as well as air stability in B-doped Si NCs. Again, B-doped Si NCs used in this work were synthesized by Nicolaas Kramer, Xin Zhang helped with part of the low temperature experiment in this chapter and Mengqun Li assisted the thermopower measurements. A manuscript based on the work in this chapter is in preparation.

Chapter 2

Electrical Transport in Nanocrystal Arrays

Nanocrystal (NC) arrays represent a novel class of artificial materials with combined properties of individual NCs and collective properties of a coupled NC array. With advanced synthetic methods and proper surface engineering, unique size-tunable properties of the NCs can be retained while the high carrier mobilities and conductivities can be achieved in NC arrays. After decades of research, NCs have found their applications in commercial displays[26]. To explore the adventure of NCs from a lab to our real life, in this chapter, we present an overview for the fundamental aspects of the electrical transport in NC arrays.

2.1 Electronic structure in nanocrystals

When the size of a crystal is reduced to a few nanometers, the electronic structure is strongly affected by the quantum confinement effect. Different from the quasi-continuous band structure in bulk semiconductor, the energy levels in NCs are discrete and size-dependent. As a consequence, the electrical, optical and magnetic properties can be tuned by varying the physical size of the crystal in this regime.

Figure 2.1a shows a comparison of the electronic structure between a bulk semiconductor and a semiconductor NC. Bulk semiconductors have bands consisting of levels closely spaced in energy, and these bands are either completely filled or completely

empty. The highest filled band is the valence band (VB); the lowest empty band is the conduction band (CB). Due to the scattering of electrons within the periodic potential of the crystal lattice, a forbidden energy gap (E_g) as a key characteristic for semiconductors is present between VB and CB. For bulk Si, E_g is 1.1 eV at room temperature. In a NC, the electron wave with low wavenumbers extends over the entire volume of the NC, and thus experiences "confinement" effect. Electrons at higher energy levels are less confined than electrons at lower energy levels, since the greater the electron energy, the smaller the relative importance of the periodic potential within the crystal. This quantum confinement effect results in quantized energy levels as well as size-dependent E_g. The smaller the NC size, the larger band gap. For example, Si NCs with diameter 4 nm have $E_g \sim 1.4$ eV, while Si NCs with diameter 3 nm have $E_g \sim 1.6$ eV. This effect is illustrated in Figure 2.1b.

In the uncharged ground state, there are no conduction electrons in a NC, and the NC array behaves as an insulator. The first added electron from external source or excitation event will occupy the lowest electron level $1S$. This electron wave function has no nodal plane and fills the entire NC. One more electron with opposite spin is allowed at the $1S$ level (spin degeneracy). For crystals with multiple equivalent conduction-band minima, their lowest conduction states are multi-fold degenerate and more electrons can be accommodated. For example, 12 electrons can be added to $1S$ level in Si since it is six-fold degenerate. The next higher energy level is $1P$, which has one nodal plane and P-type symmetry. The notation for energy levels comes from the analogy with atomic physics.

The single-electron energy levels of a NC can be calculated by solving the time-independent Schrödinger equation:

$$\left[-\frac{\hbar^2}{2}\nabla_r \frac{1}{m^*(r)}\nabla_r + V(r)\right]\varphi(r) = E\varphi(r) \tag{2.1}$$

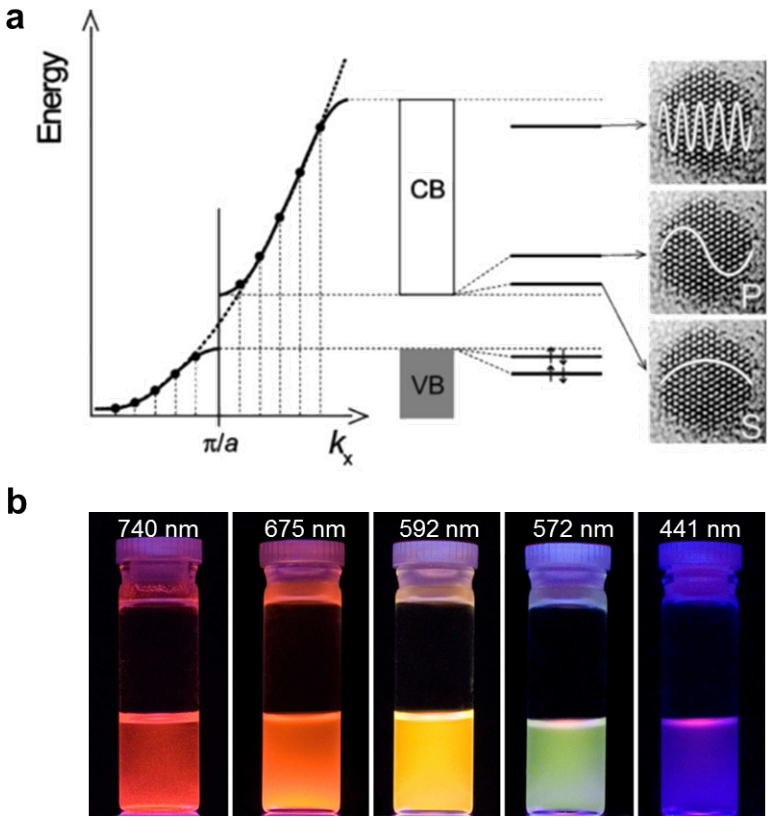

Figure 2.1: (a) Comparison of electronic structure between a bulk semiconductor and a semiconductor NC. Left: The dispersion relationship between electronic energy and electron wavenumber k (for the x-direction) in bulk semiconductor. Middle-left: The completely filled valence band and completely empty conduction band of a macroscopic insulator crystal. Bottom-right: The electron orbital with S and P symmetry. Top-right: The energy levels at higher energy in the band[27]. (b) As the size of Si NCs decreases (from left to right), the photoluminescence shifts from red to blue, which indicates the increase of bandgap[28].

One can assume a simplest model with an electron in an infinite 3D square potential well because of the relatively large work function for the NCs. The use of effective mass m^* approximation takes scattering within lattice into account. The energy level E_Q(n)

for the nth lowest electron is described as following[29]:

$$E_Q(n) = \frac{\hbar^2}{m^* d^2} \begin{cases} 0, & n = 0 \\ 19.74, & n = 1, 2 \\ 40.38, & 3 \leqslant n \leqslant 8 \\ 66.43, & 9 \leqslant n \leqslant 18 \end{cases} \tag{2.2}$$

where $\hbar$ is the reduced Planck constant, m^* is the effective mass of electron and d is the diameter of a NC.

In a spherical NC, the first three nonzero energy levels are $1S$ level with two-fold degeneracy, $1P$ level with six-fold degeneracy, and $1D$ level with ten-fold degeneracy. Again, a six times higher degeneracy holds for Si NCs with diamond structure. With a clear picture for the electronic structure of a single NC, we can continue our endeavor to carrier transport in NC arrays.

2.2 Site dispersion, exchange coupling energy and Coulomb charging energy

Generally speaking, carrier transport in a NC array depends on the following factors[1,30,31]:

- Dispersion of site energies $\Delta\alpha$ (matching of energy levels of neighboring NCs)
- Exchange coupling energy β
- Coulomb charging energy E_c

Dispersion of site energies $\Delta\alpha$ (e.g., $1S$ levels) arises from the inevitable finite distribution of size and shape in NCs. Even for a small dispersion within a single atomic layer[32], which can be achieved from the advanced synthetic techniques and size selection, a standard deviation of a few percentages still exists. The confinement energy scales approximately as $1/\mathrm{r}^2$ [27,33] at low energy where the bulk band dispersion is parabolic. For CdSe or PbSe NCs, the most studied systems, the confinement energy for electrons is $0.2 - 0.5$ eV. For Si NCs with diameter ~ 4 nm, the confinement energy is ~ 0.2 eV for electrons. A size distribution $5 - 10\%$ will give an inhomogeneous energy standard

deviation $\delta E/E = 2\delta r/r \approx 10 - 20\%$, leading to a $\Delta\alpha \sim 0.02 - 0.1$ eV which is larger than the thermal broadening at temperatures below room temperature.

To conduct current through the NC arrays, carriers should commute between NCs separated by the interparticle medium, which comprises organic ligands in most cases. These ligand molecules behave as dielectric tunneling barriers and play a critical role in the electronic coupling between NCs. In the regime of weak coupling, electron wave functions are localized on individual NCs[33,34]. When they get close to each other, these wavefunctions can interact, becoming delocalized over a few NCs or even the entire NC array. In other words, the system is in the regime of strong coupling. The exchange coupling energy β describes this quantum mechanical coupling between energy levels on neighboring NCs, and it is defined as $\beta \approx h\Gamma$, where h is Planck's constant and Γ is the tunneling rate between two orbitals of NC neighbors[27,35]. The tunneling probability through a barrier with height ΔE and width Δx can be approximated as[36]

$$\Gamma \approx \exp\left\{-2\sqrt{\frac{2m^*\Delta E}{\hbar^2}}\Delta x\right\} \tag{2.3}$$

where again m^* is the effective mass for electron. With the definition of decay length a, the above equation can be rewritten as

$$\Gamma \approx \exp\left\{-\frac{2\Delta x}{a}\right\} \tag{2.4}$$

where

$$a = \sqrt{\frac{\hbar^2}{2m^*\Delta E}} \tag{2.5}$$

As one can see from equation 2.3, the tunneling rate is exponentially dependent on the edge-to-edge distance Δx between NCs. It also has a weaker dependence on the barrier height ΔE. To improve the electronic coupling between neighboring NCs, one can reduce Δx by exchanging long-chain organic ligands with shorter ones, or lower ΔE by using conjugated ligands or inorganic materials with smaller effective band gap. Figure 3.2 displays two examples for tuning the electronic coupling through inter-NC separation. In Figure 3.2a, the array conductivity of 2.2 nm Au NCs cross-linked with $HS(CH_2)_nSH$ molecules scales as $\sigma \approx \exp(-\kappa n)$[37,38], and in Figure 2.2b the field-effect

mobility of PbSe NCs capped with $HS(CH_2)_nSH$ shows exponential dependence on the ligand length[39].

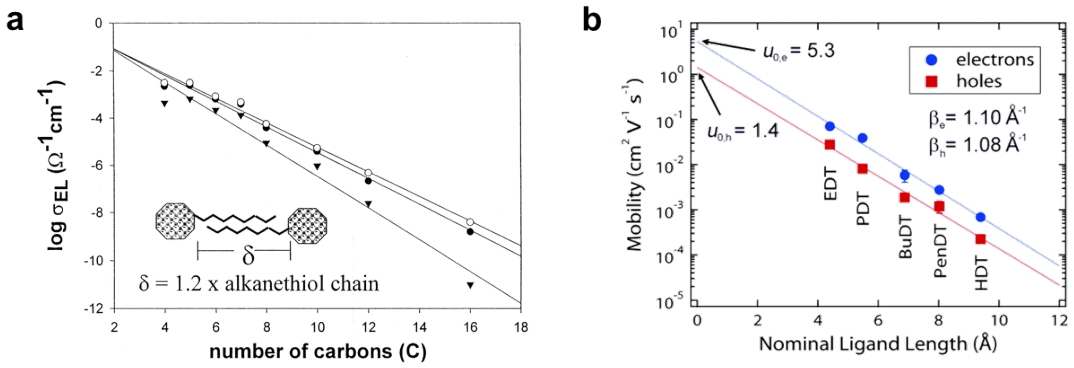

Figure 2.2: (a) Figure extracted from Wuelfing *et al.*[38] to illustrate the exponential dependence of array conductivity on the inter-NC separation in Au NCs. (b) Carrier mobility as a function of ligand length in ambipolar PbSe NC field-effect transistors[39].

With long-chain organic capping ligands exchanged with short-chain organic ligands or even conjugated ligands, significant improvement in electrical conductivity of NC arrays has been achieved. Increase of 12 orders of magnitude in array conductivity was reported in PbSe NC array[1] as shown in Figure 2.3a. A similar increase in CdSe NC array[40] was observed with introducing conjugated ligands between NCs and a conductivity of 10^{-2} S/cm was demonstrated in Figure 2.3b.

In these systems, decrease of inter-NC separation or lowering of barrier height improves the electronic coupling between NCs, resulting in conductive arrays from original insulating NC arrays. In semiconductor NC films, the increase in electronic coupling between neighboring NCs is usually consistent with broadening and redshift of the excitonic features in the abosorption spectra[6,41], and this can be used as an experimental evidence for stronger electronic coupling.

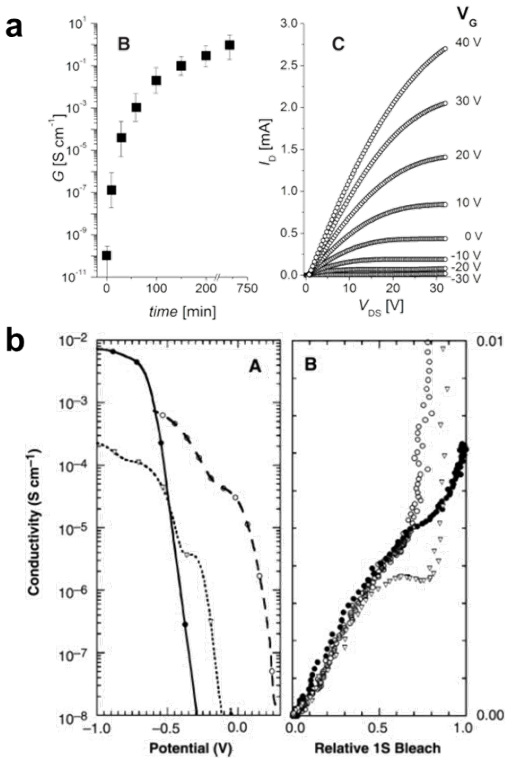

Figure 2.3: (a) Current-voltage characteristics of a field-effect transistor made from 8 nm PbSe NCs. Left: array conductance vs exposure time of hydrazine. Right: the drain current I_D versus the source drain voltage V_{DS} can be modulated by a gate voltage V_G[1]. (b) Conductivity of an array made from 6.4 nm CdSe NCs as a function of the potential for different ligands in the electrochemical cell. The highest conductivity $\sim 10^{-2}$ S/cm was achieved in pyridine-capped NCs, film cross-linked with 1,7-heptanediamine[40].

Another class of widely used short ligands is soluble molecular metal chalcogenide complexes (MCCs), such as Zintl ions (e.g., SnS_4^{4-}, $Sn_2Se_6^{4-}$, $In_2Se_4^{2-}$, $Ge_4S_{10}^{4-}$) and one-dimensional metal chalcogenide chains solvated by hydrazinium cations and/or neutral hydrazine molecules (e.g., $(N_2H_4)_2ZnTe$)[6]. MCCs not only provide excellent colloidal stability for a variety of NCs (e.g., Au NCs, CdSe nanowires), but also significantly improve charge transport in NC arrays. As shown in Figure 2.4a-c, the inter-NC distance is reduced from 2 to 0.5 nm with replacement of original dodecanethiol molecules by

$Sn_2S_6^{4-}$ molecules. Figure 2.4d compares the current-voltage characteristics for an array of Au NCs capped with dodecanethiol and an array of Au NCs stabilized with $Sn_2S_6^{4-}$. Dramatic increase in array conductivity of ~ 11 orders of magnitude is observed, and this effect cannot only be attributed to the decrease of inter-NC separation since MCCs also act as electronically transparent "glue" for NCs[6]. MCCs can decompose upon gentle heating $\sim 180 - 200$ °C, and form high-mobility compound which can participate in the charge transport.

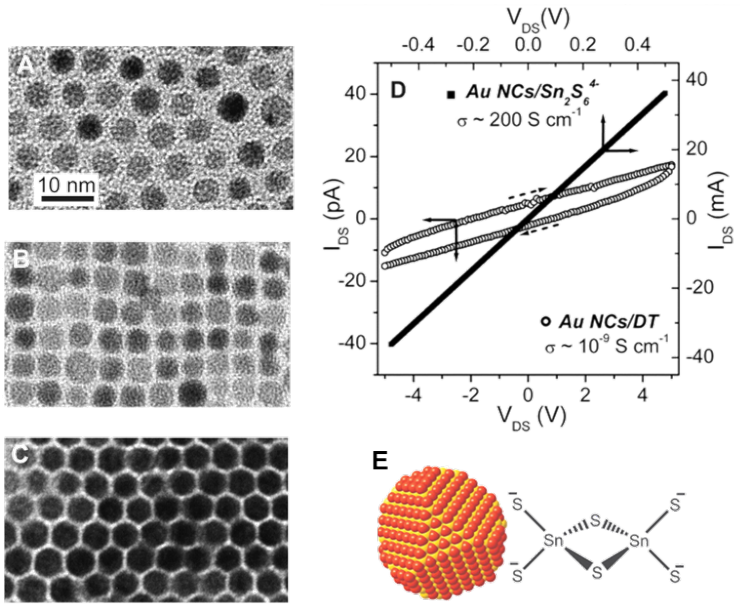

Figure 2.4: Figure extracted from Kovalenko *et al.*[6]. (a) TEM image for ~ 5 nm Au NCs capped with dodecanethiol. (b) TEM image for a layer of Au NCs capped with $(N_2H_5)_4Sn_2S_6$. (c) TEM image of a three-dimensional superlattice of Au NCs capped with $(N_2H_5)_4Sn_2S_6$. (d) Current-voltage scans for an array of dodecanethiol-capped 5 nm Au NCs (open circles) and for an array of the same Au NCs capped with $(N_2H_5)_4Sn_2S_6$ (black squares). (e) A schematic for 5 nm Au NC stabilized by $Sn_2S_6^{4-}$.

More recently, a post-synthesis colloidal atomic layer deposition (PS-cALD) was developed by Kagan *et al*[42] to produce short-range ordered, conductive lead chalcogenide

NC superlattices. The NC film was first immersed in a chalcogenide salt solution to replace the original long-chain ligands and create chalcogen-rich NC surface. This "ligand exchange" reduces the inter-NC separation and drives NCs to fuse into short-range ordered structure as shown in Figure 2.5. Further treatment with $PbCl_2$ enriches the NC surface with Pb, which structurally and oxidatively stabilizes the NC thin arrays. Electron mobility as high as ~ 4.5 $cm^2V^{-1}s^{-1}$ was demonstrated in lead chalcogenide NC arrays treated with this method. Manipulating surface ligands to create "confined-but-connected" NC superlattices was also reported by Hanrath *et al*[43], and more than 4 orders of magnitude increase in array conductivity was observed.

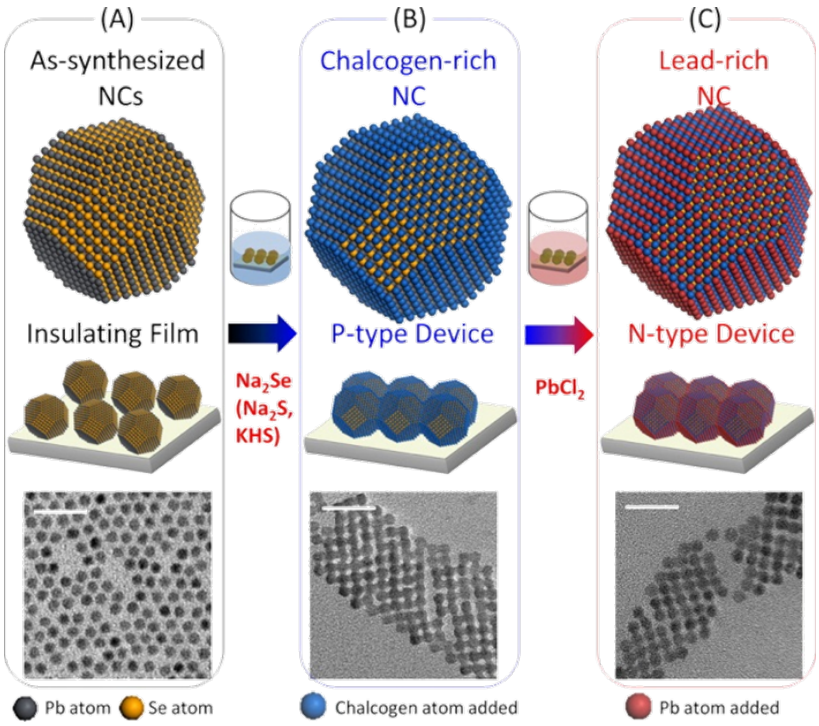

Figure 2.5: PS-cALD of lead chalcogenide NC thin films[42]. (a) As-synthesized, spin-cast NC film with oleic acid as surface ligands. (b) NC films treated in solution of either Na_2Se, Na_2S, or KHS to exchange oleic acid and to chalcogen enrich the NC surface. (c) The NC film was further treated with $PbCl_2$ to enrich the NC surface with Pb.

As mentioned above, there are no conduction electrons present in a NC without doping. In order to conduct current, electrons need to be added into NCs. When the first electron is introduced to $1S$ level of a neutral semiconductor NC, the electron charge will polarize the dielectric medium of the NC (ε_{NC}) and the dielectric medium outside of the NC (ε_i). This dielectric response of the incoming charge induces a negative charge density on the NC surface, and the repulsion between the incoming electron charge and its induced surface charge is accounted for by the Coulomb charging energy E_c[27]. It is also referred to as self-energy or self-capacitance of individual NCs. Coulomb charging energy E_c can be described as:

$$E_c = \frac{e^2}{4\pi\varepsilon_0\varepsilon_i d} \tag{2.6}$$

where ε_0 is the permittivity of vacuum and d is the diameter of NC.

This is an upper estimate of E_c since only the dielectric response of the surrounding medium is taken into account. For alkane matrix, $\varepsilon_i \approx 2$, giving $E_c \approx 0.36$ eV for NCs with 4 nm diameter.

A better estimate[19] for E_c is

$$E_c = \left(\frac{\Delta x}{d/2 + \Delta x}\right) \frac{e^2}{4\pi\varepsilon_0\varepsilon_i d} \tag{2.7}$$

For NCs with long-chain capping ligands, the NC edge-to-edge separation Δx can be $0.5 - 1$ nm and $E_c \approx 0.072 - 0.12$ eV.

In this thesis work, we use an effective dielectric constant ε_r to estimate the charging energy. Since both of the NC and surrounding medium are polarized in response to the incoming charge, the decrease in charging energy can be taken into consideration by using a renormalized dielectric constant as described in the canonical Maxwell-Garnett formula[44]

$$\varepsilon_r \simeq \varepsilon_i \frac{\varepsilon_{NC} + 2\varepsilon_i + 2\phi(\varepsilon_{NC} - \varepsilon_i)}{\varepsilon_{NC} + 2\varepsilon_i - \phi(\varepsilon_{NC} - \varepsilon_i)} \tag{2.8}$$

For Si NCs, if one assume a cubic lattice for the NC arrays and $\varepsilon_i \approx 1$, the effective dielectric constant ε_r can be plotted as a function of the array density ϕ as shown in Figure 2.6. For a given NC system, the effective dielectric constant ε_r increases as the array density increases.

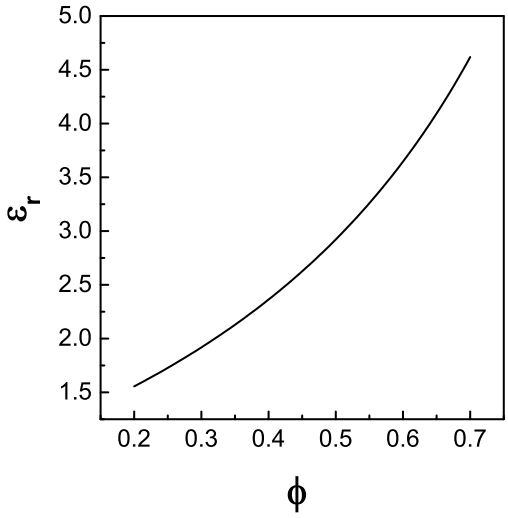

Figure 2.6: Effective dielectric constant ε_r is plotted as a function of Si NC array density ϕ based on equation 2.8, and $\varepsilon_{NC} = 11.7$ is used for Si.

Again, for Si NCs with diameter 4 nm and array density ~ 0.4, the estimated E_c is 0.14 eV. This estimation is in excellent agreement with experimental result [25]. As shown from the above equations, the charging energy for a NC is size-dependent. The charging energy can be experimentally determined by current-voltage measurements through scanning tunneling microscopy (STM) [45,46]. For instance, the measured value for 3 nm Ag NC is 340 meV from STM [46].

2.3 Electrical conduction mechanisms

Now let us construct a picture for different regimes of electronic coupling. If the coupling energy is smaller than thermal energy ($\beta \ll k_B T$), the system is in the weak coupling regime in which electrons can only tunnel between neighboring NCs. The conduction occurs through sequential tunneling [27,33]. In the strong coupling regime, $\beta \geq k_B T$; the delocalized states extend over a few NCs or the entire NC arrays. Therefore, the strong coupling regime can, in principle, be realized by a sufficient reduction of the temperature for a given NC array [33]. In a NC array with strong coupling, discrete wave functions on individual NCs form a band with bandwidth proportional to the exchange

coupling energy β[27]. This effect is illustrated in Figure 2.7a. As the inter-NC separation decreases, the coupling energy between NCs becomes larger, and thus the bandwidth increases. In the strong coupling regime, we can define two sub-regimes by comparison of the coupling energy β and the site dispersion $\Delta\alpha$. If $\beta < \Delta\alpha$, the system is consisted of small isolated domains with strong coupling, separated by weakly conducting domains. This is Anderson localization due to fluctuations in electron energy from one NC to another[47]. Figure 2.7b gives a schematic of the Anderson localization. If $\beta > \Delta\alpha$, the coupling energy is sufficient to overcome the site dispersion, extended wavefunctions exist over the entire NC arrays and the Anderson metal-insulator transition occurs.

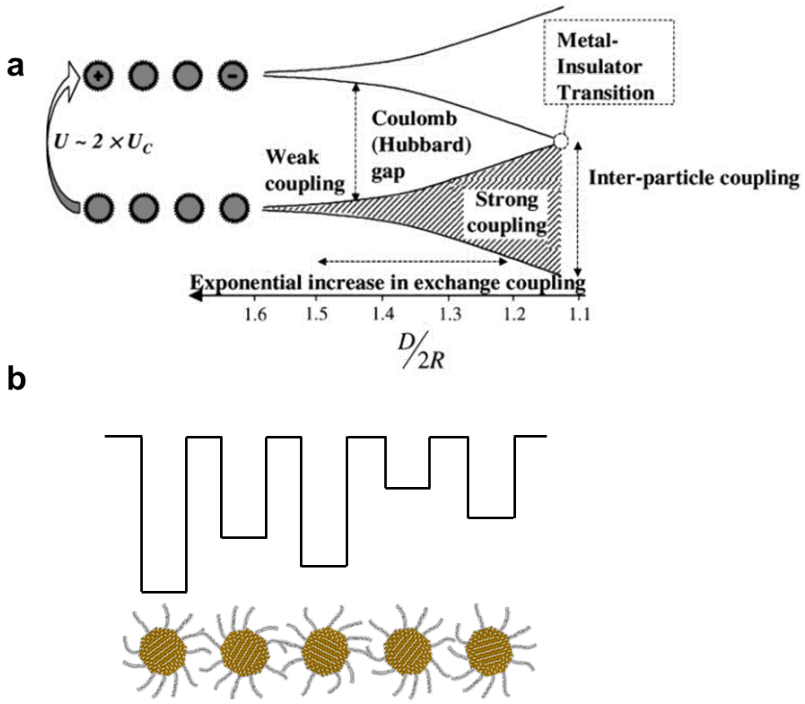

Figure 2.7: (a) Electronic structure and interparticle interactions in a NC array. As inter-NC separation Δx decreases, the NCs experience stronger exchange interactions and a band is formed from the discrete wave functions. At the point where the coupling energy exceeds the charging energy, the NC array undergoes a metal-insulator transition. Figure is extracted from Murray *et al.*[48]. (b) A schematic for Anderson localization in a NC array.

In a weakly coupled system, the charging energy creates the Coulomb energy gap, also named as Hubbard gap with energy $\sim 2E_c$ (see Figure 2.7a), suppressing low-bias conduction as observed in the Coulomb blockade effect[33,49]. Current can only flow through such a NC array when applying sufficiently large voltage to overcome the Coulomb blockade. In a strongly coupled system, if $\beta > E_c$, the Coulomb gap will be closed as shown in Figure 2.7a and carriers can move freely throughout the NC arrays, leading to Mott metal-insulator transition[50].

Mott and Anderson metal-insulator transitions describe two extreme cases. The former model predicts the disappearance of Coulomb gap by sufficient exchange coupling under an assumption of no site disorder. Anderson model shows that sufficiently large site disorder can cause localization of carriers. Metal-insulator transition has been experimentally demonstrated near room temperature in metallic NCs through manipulating inter-NC separation. Heath *et al.* observed a reversible metal-insulator transition in monolayers of propanethiol-capped 3 nm silver NCs through optical responses[31]. The transition occurred when the inter-NC separation was below $\sim$ 5 Å. Zabet-Khosousi *et al.* investigated resistance versus temperature in arrays of Au NCs linked by $HS(CH_2)_nSH$ ($n = 2 - 10$)[51]. When the inter-NC separation approaches 1.1 nm ($n = 5$), the NC array experiences Mott metal-insulator transition.

So far we only consider one type of disorder in NC arrays, the site dispersion $\Delta\alpha$, another typical disorder in NCs is packing disorder which leads to variation of inter-NC separation. Remacle *et al.* theoretically examined the effects of $\Delta\alpha$, β, E_c and packing disorder on the transport properties of NC arrays[33]. Figure 2.8 shows a phase diagram summarizing different coupling regimes for a NC array. When large disorder (site dispersion and/or packing disorder) is present in a NC array, the electronic states are localized on individual NCs. As the disorder is reduced, exchange coupling occurs between neighboring NCs and delocalized states are formed with sufficient electronic coupling. At very small disorder, the NC array can behave as a Mott insulator when $E_c > \beta$. Between the fully delocalized states and fully localized states, the NC system has an intermediate regime (domain localized) with delocalized states extended over a few NCs.

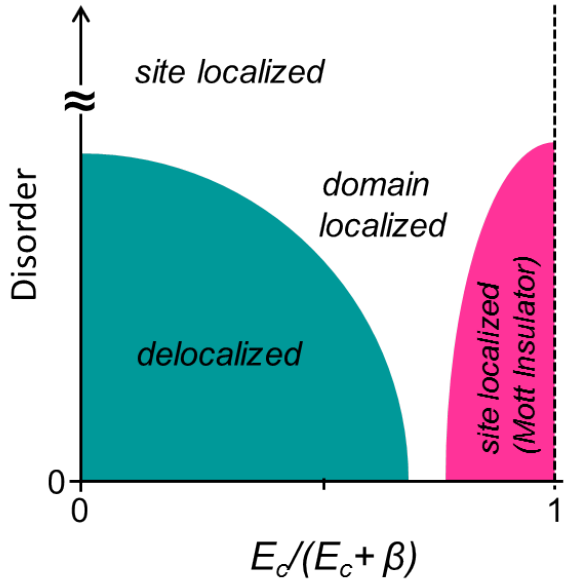

Figure 2.8: A phase diagram of different coupling regimes for a NC array with site dispersion and/or packing disorder[33].

Different transport mechanisms dominate in regimes with different coupling between neighboring NCs. Temperature dependences of array conductivity or carrier mobility have been used as a typical method to probe the electrical transport in NC arrays. Metallic behavior in which resistance increases with increasing temperature was reported in Ag NCs[52] and Au NCs[51]. In semiconductor NCs, "band-like" transport has been observed in strongly coupled CdSe NCs. The primary evidence for possible band transport in the current research is the apparent negative temperature coefficient of the mobility ($\mathrm{d}\mu/\mathrm{d}T < 0$) measured from field-effect transistors[41,53]. Figure 2.9 shows the bandlike transport in CdSe NCs capped with inorganic ligands ammonium thiocyanate and doped with indium[41]. With engineering trap states at the interface of NC array and dielectrics, the temperature regime for band-like transport can extend to 140 K. Also, this CdSe NC system exhibits the record electron mobility as high as 27 $\mathrm{cm^2V^{-1}s^{-1}}$. A similar behavior of negative temperature coefficient for electron mobility was observed in MMC-capped CdSe NCs with $\mu \sim 16$ $\mathrm{cm^2V^{-1}s^{-1}}$[53].

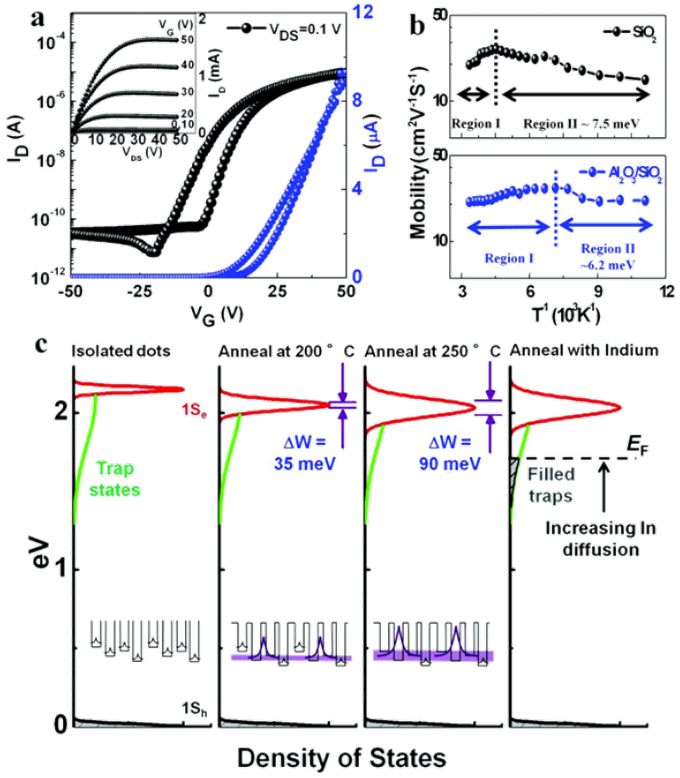

Figure 2.9: Figure extracted from Choi *et al.*[41]. (a) Transfer characteristics of CdSe field-effect transistors. (b) Temperature dependence of mobility in devices with SiO_2 and Al_2O_3/SiO_2 as gate insulators. (c) Electronic structure of CdSe NCs as isolated, annealed and In-doped. In an isolated NC array, electron wavefunctions are localized on individual NCs. After annealing, strong coupling is present in the NC array and a miniband is formed. With In doping, traps within the bandgap are filled, and band-like transport is observed.

However, Guyot-Sionnest pointed out that hopping transport can also lead to mobility increase with decreasing temperature at $T > E_a/k$, since the carrier mobility has an exponential dependence on the activation energy E_a as described[19]:

$$\mu = \frac{ed_{cc}^2 E_a}{3hk_BT}\exp\left[-\frac{2\Delta x}{a} - \frac{E_a}{k_BT}\right] \tag{2.9}$$

where d_{cc} is center-to-center distance for NCs and again, Δx is edge-to-edge separation.

For a field-effect transistor, the temperature dependence of mobility based on equation 2.8 is plotted in Figure 2.10.

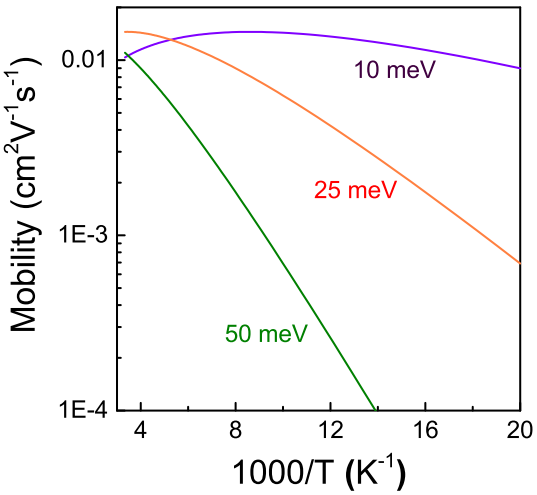

Figure 2.10: Temperature dependence for mobility in a FET with $d_{cc} = 7$ nm, $e^{-2\Delta x/\alpha} = 10^{-3}$ and $E_a = 10, 25, 50$ meV. Figure replotted from Guyot-Sionnest[19].

In a weakly coupled NC array, the carriers are localized on individual NCs and the electrical transport occurs by sequential tunneling between neighboring NCs. This is hopping transport. In general, the ohmic conductance G of an insulating disordered system is determined by the probability of tunneling between localized sites in distance r:

$$G \propto \exp\left[-\frac{2r}{\xi} - \frac{E_a}{k_B T}\right] \tag{2.10}$$

where E_a is the energy mismatch between initial and final states (activation energy) and ξ is the localization length. The first term $\exp(-2r/\xi)$ describes the probability of tunneling in distance r while the second term $\exp(-E_a/k_B T)$ is the activation probability with energy mismatch E_a.

At relatively high temperature, the thermal energy is sufficient to overcome the energy mismatch between neighboring NCs, and an electron can always hop to a neighbored NC with assistance of a phonon. This transport mechanism is named as nearest

neighbor hopping (NNH) or activated conduction. In the density of ground states, the activation energy E_a in this process opens a hard gap of width E_a centered at the electron Fermi level (see Figure 2.11). As a result, the array conductance follows the Arrhenius law:

$$G \propto \exp\left[-\frac{E_a}{k_B T}\right] \tag{2.11}$$

This behavior has been observed in NC arrays at moderate temperature (above $\sim$ 120 K)[25,54]. The charging energy dominates the activation energy in this regime.

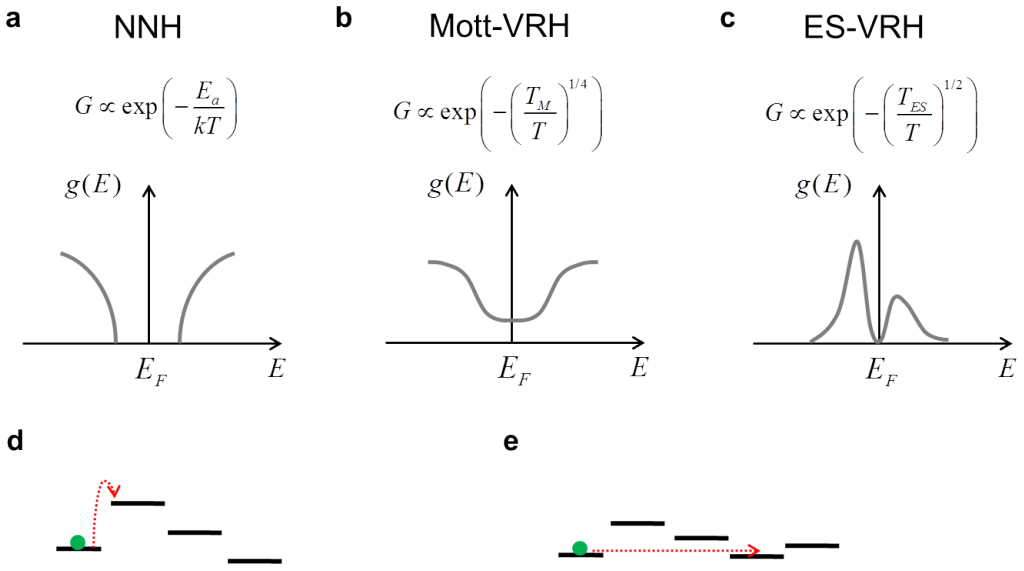

Figure 2.11: Comparison between different transport mechanisms. (a)-(c) illustrates the temperature dependence of ohmic conductance and the distribution of density of states near Fermi level in NNH, Mott-VRH, and ES-VRH, respectively. (d) A schematic for nearest neighbor hopping between NCs. (e) A schematic for variable range hopping between NCs.

At sufficiently low temperature, the electrical transport usually deviates from the Arrhenius behavior, since the thermal energy cannot provide the required activation energy for an electron to jump to neighboring NC. Instead of hopping to a neighboring

NC with large activation energy E_a, the electron prefers to tunnel to a distant site with small E_a, leading to variable range hopping (VRH). This model was originally developed for lightly doped semiconductors and the localization length ξ was introduced to describe the wave function decay between distant states. The tunneling probability between neighboring NCs is defined as $\Gamma \approx \exp(-2\Delta x/a)$ (see equation 2.4), it exponentially depends on the barrier width (edge-to-edge separation of NCs). When an electron tunnels to a NC at a distance with r, the path for the electron is to travel primarily through n nearest-neighboring NCs[29]. Therefore, the tunneling probability through n NCs in this process is Γ^n:

$$\Gamma^n \propto \exp\left[-\frac{2n\Delta x}{a}\right] = \exp\left[-\frac{2r}{\xi}\right] \tag{2.12}$$

where $\xi = a\left[(D + \Delta x)/\Delta x\right]$. It is as if the wave function had an exponential decay of length ξ, and this parameter is called the "localization length" in VRH.

Assume a constant density of states g_0 near the Fermi level, Mott pointed out the energy mismatch is given by $E_a \sim 1/g_0 r^n$, where n is the dimension of the material. An electron will always try to find the lowest activation energy and the shortest tunneling distance. By maximizing the tunneling probability (equation 2.10), we get Mott's law[50]:

$$G \propto \exp\left[-\left(\frac{T_M}{T}\right)^{1/(n+1)}\right] \tag{2.13}$$

where T_M is the characteristic temperature. In 3D system, the array conductance is proportional to $\exp[-(T_M/T)^{1/4}]$ and T_M is given by

$$T_M = \frac{\beta}{k_B g_0 \mu^3} \tag{2.14}$$

This behavior has been observed in various bulk lightly doped semiconductors, and more recently, reported in CdSe NCs[24].

Efros and Shklovskii expanded this model by including Coulomb interactions between electrons[55]. They modified Mott's law as

$$G \propto \exp\left[-\left(\frac{T_{ES}}{T}\right)^{1/2}\right] \tag{2.15}$$

where T_{ES} is

$$T_{ES} = \frac{Ce^2}{4\pi\varepsilon_0\varepsilon_r k_B \xi} \tag{2.16}$$

C is a numerical factor. For 3D bulk semiconductor, $C = 2.8$; for 3D NC arrays, $C = 9.6$[29].

This behavior, known as Efros-Shklovskii variable range hopping (ES-VRH), arises from the Coulomb gap in the density of states near Fermi level. In Mott's law, constant density of states are assumed; but a soft gap is present in density of states for ES-VRH[55] (see Figure 2.11). Recent experiments on weakly coupled NCs have shown agreement with ES-VRH[54,56,57] . The localization length reported in CdSe NCs is ~ 1 nm[24]. In NC systems, ES-VRH behavior originates from the charging of a substantial fraction of NCs[29,55]. This charging introduces a random Coulomb landscape that shifts up and down the electron energy at different NCs. Therefore, the hard gap in the density of states is smeared and filled, resulting a soft gap at the Fermi level. Some electron states are very close to the Fermi level, one can always find a pair of empty and filled states separated by an energy $E < E_c$ and hopping occurs between these two states. At high bias (non-Ohmic regime) and low enough temperature, the external electric field F effectively reduces the barrier to down field NCs, leading to temperature-independent conductance (G)

$$G \propto \exp\left[-\left(\frac{F_{ES}}{F}\right)^{1/2}\right] \tag{2.17}$$

where the characteristic electric field F_{ES} is defined as

$$F_{ES} = \frac{k_B T_{ES}}{2e\xi} \tag{2.18}$$

Figure 2.12 shows the temperature dependence of the ohmic conductance and the electric field dependence of conductance for CdSe NCs capped with pyridine[54]. As mentioned above, different transport mechanisms may dominate in different regimes. Increasing the temperature will reduce the effects of the Coulomb gap and cause transition from ES-VRH to Mott-VRH. If the temperature goes higher, one can see NNH.

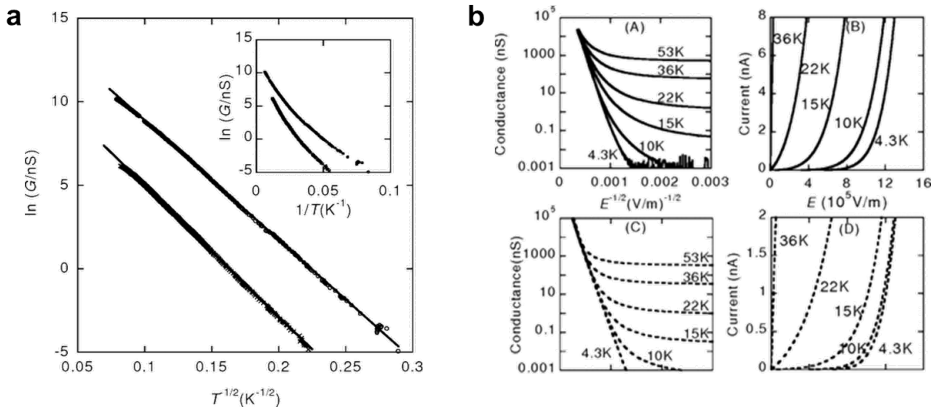

Figure 2.12: (a) Temperature dependence of the low-field conductance (bias = 1 V) in the range $11 < T < 160$ K. (b) Field dependence of conductivity[54].

The transport mechanisms in a weakly coupled NC array can be summarized as follows:

$$G \propto \exp\left[-\left(\frac{T_0}{T}\right)^{\gamma}\right] \tag{2.19}$$

where the temperature exponent γ depends on the transport mechanism, and T_0 is a characteristic temperature. The exponent γ can be determined from Zabrodskii reduced energy analysis[58]. One can plot $w = d(\log G)/d(\log T)$ against temperature T on the double logarithmic scale, and γ can be fit from the slope[24].

Additionally, a cotunneling model was proposed to describe the electrical transport in weakly coupled metal NCs[59]. In sequential tunneling (e.g., VRH), an electron hops from an initial NC to final NC through nearest neighbors along the path. In inelastic cotunneling, electrons move cooperatively that each one goes to the nearest neighbor but are synchronized to move charge. This transport mechanism has the same form for temperature dependence as ES-VRH. An exponent of 2/3, independent of charge concentration and dielectric environment, was reported in ZnO[60]. An identical temperature dependence was observed in Au NCs[51].

The electrical transport study for intrinsic semiconductor NCs has been primarily performed on two different platforms, one is the electrochemical cell and the other one is

the field-effect transistor. Both of them can introduce electrons to semiconductor NCs, enabling electron conduction in a NC array. In an electrochemical cell, electrons are injected into the conduction levels of the NCs by control of the electrochemical potential. The positive counterions can penetrate the NC array, and are brought in close proximity with NCs to compensate the negative charge. With freezing the electrolyte in the cell, the positive ions remain in place, enforcing the local charge of NCs to remain[27]. Therefore, the electrical conduction can only be studied below the melting point of electrolyte, usually below 160 K[54]. This is also called "electrochemical gating". It enables the charging of a specific level in NCs which can be determined from the optical bleach spectrum[61]. The temperature dependence of conductivity in NCs assembled in an electrochemical cell is still studied in a two-terminal measurement. The contact resistance is usually ignored due to the much larger resistance of NC arrays. The field-effect transistor is another platform used for electrical transport study. A typical transistor is a device with three terminals: source, drain and gate. Carriers can be injected into NCs by manipulating the gate voltage. This applied electrical field adjusts the conduction/valence levels in NCs, and acts as a gate for the electrons flowing from the source through NCs to the drain. The concentration of injected carriers can be calculated from the capacitance of the dielectric material and the applied gate voltage based on the transistor working principles[62]. The transistor structure also allows the measurement of the carrier mobility. This mobility is the field-effect transistor mobility for two dimensional transport, since only the first $\sim$ 10 nm of NC array (about two monolayers of NCs) are involved under most bias conditions[63]. The differences between a field-effect mobility and the field-free mobility in a NC device (e.g., solar cell) are discussed in Law *et al.*[63].

2.4 Doping in nanocrystal arrays

To achieve bulk-type transport in a NC array for electronic applications, three requirements need to be met. The first one is to form minibands through strong interparticle coupling as discussed in the previous section. It can be achieved by shrinking the distance between NCs down to subnanometer, lowering the tunneling barrier with proper design of ligands, or fusing NCs to form "confined-but-connected" structure. Secondly,

one needs to minimize the number of trap states associated with dangling bonds at NC surfaces or caused by other structure defects. Moreover, additional carriers should be introduced into the NC array to conduct currents, and this leads to doping in NCs.

Doping of bulk semiconductors by impurity atoms enables electrical transport in an otherwise insulating material, resulting in a wide range of technological applications in microelectronics and optoelectronics. A substitutional impurity atom occupies a host atom position in the lattice, and behaves as n-type donor if having one more valence electron than the host atom. Similarly, an impurity with one less valence electron acts as p-type acceptor, providing an extra hole for transport. Stimulated by doping in bulk semiconductors, extensive efforts in the past decades have been devoted into the doping in semiconductor NCs. Here we summarize several strategies reported in literature to dope semiconductor NCs.

- Remote doping
- Electrochemical doping
- Stoichiometric inbalance doping
- Electronic impurity doping

Remote doping, also called surface transfer doping, is achieved through electron-donating molecules or atoms in the vicinity of the NC surface. Figure 2.13 illustrates this effect using acceptors. If the lowest unoccupied molecular orbital (LUMO) of the surface acceptors is close to the valence band maximum of the semiconductor, it will easily get an electron from the semiconductor, just as the classical acceptors do. As a result, there are holes left in the semiconductor and negative charges localized on the surface acceptors. This is p-type surface transfer doping. Equivalently, the surface donors can donate electrons from their highest occupied molecular orbital (HOMO) to the conduction band minimum of the semiconductor, leading to n-type surface transfer doping. This is the one typically observed in semiconductor NCs.

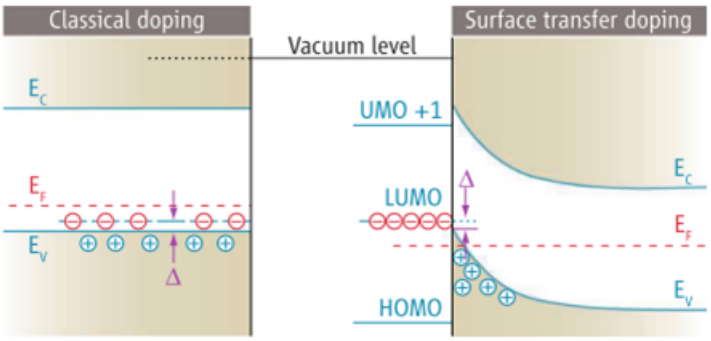

Figure 2.13: Band diagrams for classical p-type doping (left) and p-type surface transfer doping (right)[64]. E_c and E_v are the energies of the conduction band minimum and the valence band maximum, respectively. LUMO and HOMO are the lowest unoccupied and highest occupied molecular orbitals of the surface acceptors, respectively.

Sodium biphenyl was first reported as an electron-transfer reagent in CdSe NCs system in 2000 by Shim and Guyot-Sionnest[65]. Then Guyot-Sionnest *et al*[40] observed electron transfer from potassium to CdSe NCs, leading to occupation of first two electronic shells, $1S_e$ and $1P_e$. In 2005, Talapin and Murray showed that hydrazine behaves as a charge-transfer n-type dopant in PbSe NCs, and reversible p-type conduction is achieved by stripping hydrazine from surface of NCs[1]. However, this may also be related to doping from stoichiometry inbalance which will be addressed later.

Electrochemical doping (or electrochemical gating) introduces electrons by control of electrochemical potential as discussed in previous section. This method has been widely used in group II-VI compound semiconductor NCs. It requires a porous structure to allow diffusion of counterions, which limits the materials and structures to be explored.

Doping by stoichiometry control has attracted significant attention recently, especially for PbS or PbSe NCs. In bulk lead chalcogenides of PbS, PbSe, and PbTe[66], the majority carrier type can be tuned by stoichiometric inbalance. Pb-rich layers lead to n-type doping while X (X = S, Se, Te)-rich layers result in p-type doping[67–69]. Similar behavior was observed in PbSe NCs and the stoichiometric inbalance was controlled by the chemistry of surface ligating compounds. Beard *et al* found that hydrazine-treated PbSe NC arrays have Pb-rich stoichiometry while 1,2-ethanedithiol (EDT) shifts the

stoichiometry toward Se-rich[70]. Based on this stoichiometric inbalance concept, novel postsynthesis approaches have been developed to control the majority carrier type in PbSe NCs from Murray and Kagan groups. One is the direct thermal evaporation of Pb or Se atoms onto NC arrays[71], and the other one is colloidal atomic layer deposition[42].

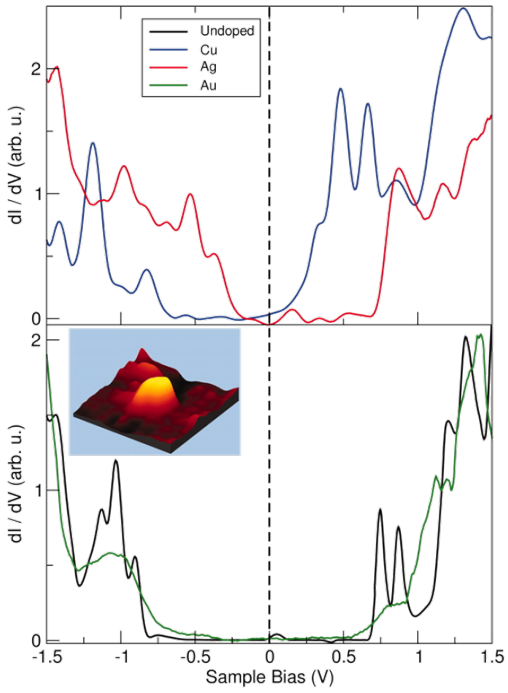

Figure 2.14: The doping effects on the STM tunneling spectra extracted from Banin *et al*[72]. The vertical dash line is to guide the relative shifts of the band edge in doped samples.

Electronic impurity doping is the process to intentionally incorporate impurities into the lattice of single NC. Due to the synthetic challenges, little progress has been made even after decades of research. While substitutional doping for color center impurities[73] and magnetic impurities[74–76] (e.g., Mn and Co) has seen some success, these dopants are isovalent with cations they replace and no extra carriers are added into NCs. Banin *et al*[72] explored Cu-, Ag-, and Au-doped InAs NCs, and displayed shifts in the valence and conduction bands through scanning tunneling microscopy on individual NCs as shown in Figure 2.14. In bulk semiconductor, n-type doping shifts the Fermi level close to the

conduction band and p-type doping moves the Fermi level towards the valence band. This effect was clearly identified in STM tunneling spectra of doped InAs NCs, and a simple model was proposed to explain the data: interstitial Cu gives n-type doping, substitutional Ag leads to p-type doping and substitutional Au may adopt a +3 valence state, thus no doping effect was observed.

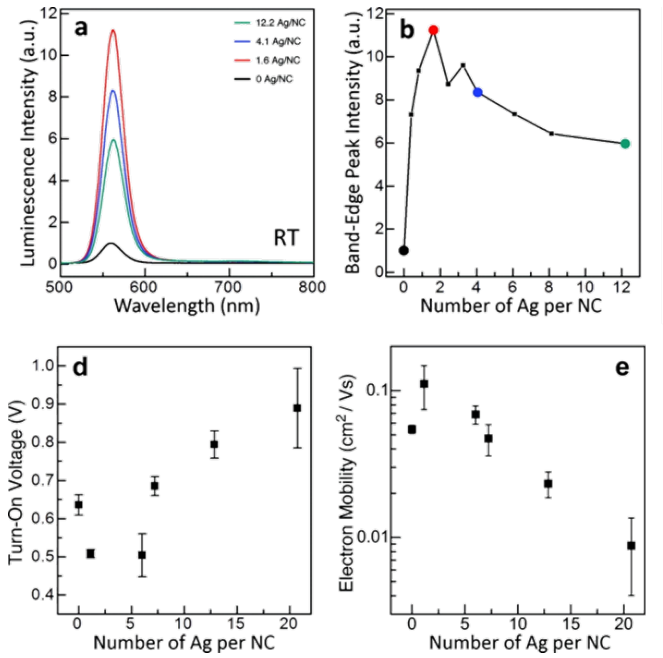

Figure 2.15: Doping effects on the optical and electrical properties for CdSe NCs[77]. (a) and (b) Room-temperature fluorescence of CdSe NCs with different Ag doping levels. (d) and (e) Turn-on voltage and electron mobility for the ion-gel-gated thin-array transistors used to characterize the electrical properties of doped CdSe NCs.

More recent work by Norris *et al*[77] demonstrated successful Ag doping in prototype CdSe NC system and revealed unexpected complexity in optical and electrical properties. It was found that the addition of a few Ag (around 2) atoms causes a large unexpected enhancement in the fluorescence, and further addition of Ag atoms quenches the fluorescence (see Figure 2.15a and b). They concluded that Ag occupies interstitial position (n-type) at low doping level and behaves as substitutional impurity (p-type) at

high doping level as shown in the changes of turn-on voltage and electron mobility of the thin-array transistors (Figure 2.15d and e). It is noted that the number of Ag per NC is measured from the elemental analysis, the real doping concentration is unknown.

The incorporation of dopants into NCs in the above two examples was conducted in solution synthesis. Metal atoms diffused into the preformed InAs NCs at room temperature in a solution mixture of metal salt and NCs[72]. Ag doping in CdSe was performed in a modified cation-exchange process[78,79]. However, dopants can also be incorporated in a NC array. Kagan and Murray demonstrated a new method to dope CdSe NC arrays through thermal diffusion of a dopant metal indium (In)[41]. In this method, In/Au electrodes were thermally deposited on the NC array, and devices were annealed at 250 °C for 10 min to achieve dopants diffusion.

So far, we only talk about the compound NCs produced from wet chemistry method, in which molecular precursors containing the constituent elements are injected into a hot bath with temperature typically below 350 °C. For group IV semiconductor (e.g., Si and Ge) NCs with high crystallization temperature, nonthermal plasma gas phase method provides a more favorable synthesis approach. Kortshagen *et al* demonstrated incorporation of P and B atoms in Si NCs[80] and observed localized surface plasmon resonance in heavily P-doped Si NCs[23]. Typically, silane is used as the precursor gas for Si NCs, and phosphine or diborane gases are introduced into the plasma as precursors for dopants. Nozaki *et al* explored the electronic activation of P- and B-doped Si NCs by field effect transistor analysis and showed that the dopant activation efficiency is only $\sim 10^{-2} - 10^{-4}$[81]. In this thesis work, doping effects on the electrical transport in Si NC arrays are investigated. Depending on the doping concentration, different transport mechanisms have been observed. When the doping concentration is very small, the number of donors per NC $\nu \ll 1$, the conduction is activated. The conductivity of NC arrays is dominated by the rare donor-electrons with concentration ~ 1 donor-electron per 1000 NCs. When the doping concentration $\nu \gg 1$, ES-VRH becomes dominant. Indeed, doping concentration plays a critical role in the electrical transport. The location of dopants is also important in the NC systems, as will be discussed in the B doping case. It is found that the film conductance of B-doped Si NCs can be tuned by the manipulation of the surface states. Moreover, the air stability of Si NC films can be significantly improved through a post-synthesis approach.

Chapter 3

Plasma Synthesis of Silicon Nanocrystals

3.1 Introduction

Nonthermal plasma synthesis has emerged as an alternative method to produce nanocrystal materials, especially for group IV semiconductors with high crystallization temperature. For Si NCs with diameter of 4 nm, the crystallization temperature is as high as 773 K[82]. In a nonthermal plasma, there are two unique features which make it an outstanding synthesis method for NCs:

- In nonthermal plasmas, electrons are accelerated to temperatures between 20000 and 50000 K ($\sim 2-5$ eV)[83] while positive ions and neutral species remain close to room temperature, resulting in a nonequilibrium environment. These hot electrons can effectively dissociate precursor molecules to assemble NCs. Energetic surface reactions, such as electron-ion recombination, also provide intense heating for nucleation and growth of NCs[84,85].
- Due to the dramatic difference in mobility between electrons and ions, nanoparticles in plasmas tend to be unipolarly negatively charged[86]. This charging strongly reduces agglomeration of NCs and leads to a narrow size distribution[87,88].

Different from solution synthesis, gas phase nonthermal plasma method produces clean materials without organic ligands, and also opens opportunities for scalable high-yield production. After decades of research, solution-based colloidal synthesis has developed into a new branch of synthesis chemistry, and a broad range of nanomaterials have been successfully synthesized with excellent control over size and shape. Organic ligands, typically long-chain carboxylic and phosphonic acids (e.g., oleic acid and *n*-octadecylphosphonic acid), are necessary for NCs synthesis in the solution phase. They dynamically adhere to the surface of growing nanocrystals[32,89] and play the key role in controlling the kinetics of nucleation and growth[48,90]. Because of the insulating nature of these ligands, further processes like ligand exchange for shorter ones, need to be performed to allow electronic coupling between NCs and make conductive films. In gas-phase nonthermal plasmas, unipolar negative charging keeps NCs apart by electrostatic repulsion and enables well-controlled particle growth with narrow size distribution. Therefore, ligand-free NCs can be obtained from the nonthermal plasma method. Further surface treatment may apply, depending on the desired applications of NCs.

3.2 Plasma synthesis of silicon nanocrystals

Si NCs used in this thesis work were produced from two different reactors. One is located in L122, primarily designed to synthesize photoluminescent Si NCs. They were used in the electrical transport study for lightly doped Si NCs, and were synthesized by the author. The other one resides in Nano Fabrication Center, mainly for P-/B-doped Si NCs; these particles were provided by Nicolaas Kramer, a graduate student in Kortshagen's group. We are focusing on synthesis of photoluminescent Si NCs in this chapter, and details for synthesis of P-/B-doped Si NCs will be introduced later. Figure 3.1 shows a schematic of L122 plasma reactor as well as a cartoon for NC formation in the plasmas.

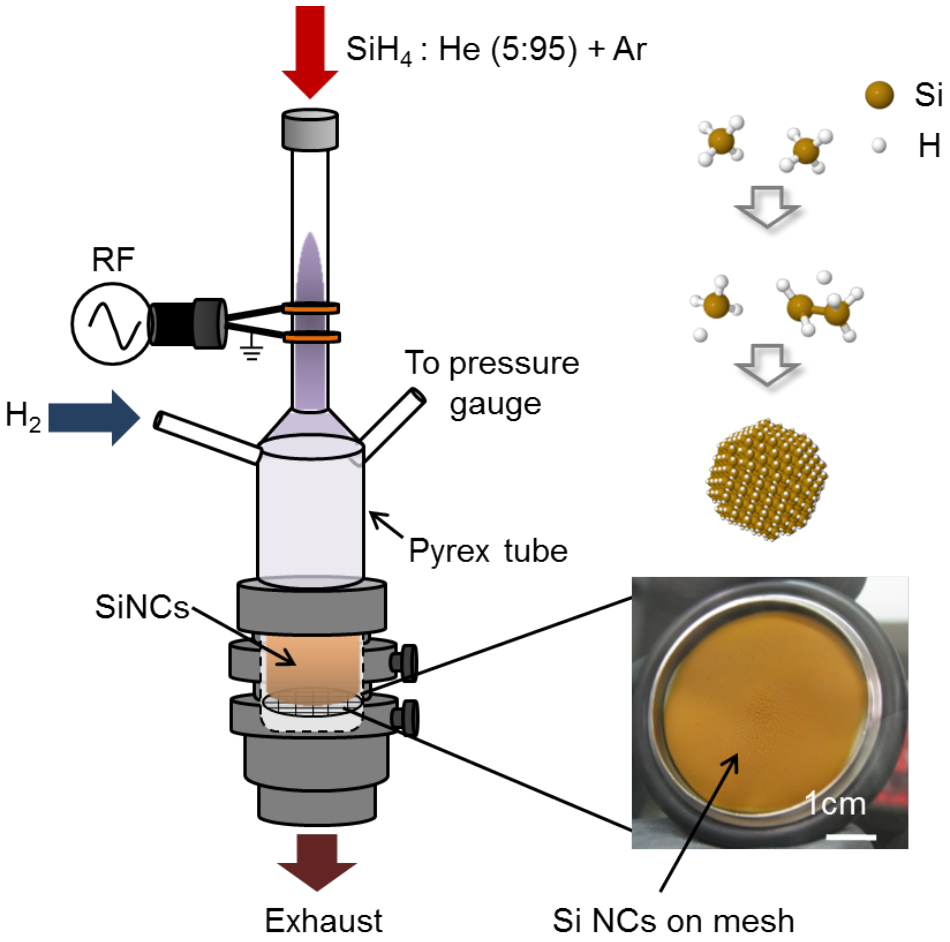

Figure 3.1: A schematic of the plasma reactor in L122 and a cartoon for NC formation in the plasma. The Si NCs are collected on a stainless steel mesh, and appear as orange powder.

The precursor gas for Si NCs is 5% silane diluted in helium, and argon as carrier gas are flowing into the system from the top. Hydrogen gas is injected into the plasma from one side arm, and the importance of this hydrogen injection on NC surface passivation has been illustrated in previous work[91]. A typical plasma for Si NCs synthesis is run at pressure $\sim$ 1.4 Torr and a butterfly valve is used to keep constant pressure during synthesis. The particle size can be tuned by the residence time in the plasma, which is usually achieved by changing the argon flow rate while maintaining the same reactor

pressure. The residence time for typical 4 nm Si NCs is about 27 ms. The crystallinity of nanocrystals can be controlled through the power delivered into the plasma, a typical nominal power used for 4 nm Si NCs is 50 $\sim$ 65 W.

Three different sizes of Si NCs were made with various argon flow rates at the same pressure $\sim$ 1.4 Torr . For 2.8 nm Si NCs, the nominal power was kept same at $\sim$ 60 W but the plasma was longer than 4 nm Si NCs. For 4.7 nm Si NCs, the plasma length was kept same as 4 nm Si NCs, but the nominal power was higher. These adjustments for plamsa conditions were made to produce crystalline Si NCs. Figure 3.2a shows the X-ray diffractions (XRD) spectra from the Si NCs synthesized with argon flow rates of 10 standard cubic centimeters (sccm), 30 sccm and 75 sccm. The well-defined peaks indicate diamond structure of Si and the sizes of particles are estimated from Scherrer equation[92]. The crystallite size of spherical particles is underestimated in XRD and this effect has been taken into account by multiplying a factor of 4/3[93]. With the argon flow rate increasing, the particle diameter shrinks from 4.7 nm to 2.8 nm. The as-produced Si NCs are usually collected on a stainless steel mesh as shown in Figure 3.1, and hydrosilylation reaction is performed to attach organic ligands onto the NC surface, rendering colloidal stability and surface passivation for photoluminescent applications. Details of this reaction can be found in experimental method section. The photoluminescence of these three sizes of Si NCs is shown in Figure 3.2b. As the NC size increases, the PL peak position shifts from 754 nm towards 939 nm, correpsonding to bandgap change from 1.6 eV to 1.3 eV. This is consistent with the bandgap values calculated from quantum confinement. The photoluminescent quantum yield (PLQY) is defined as the ratio of the number of emitted photons and the number of absorbed photons. For typical 4 nm Si NCs, an ensemble QY higher than 60% can be achieved after thermal hydrosilylation with 1-dodecene[17]. Figure 3.2b compares the PLQYs for the Si NCs with three different sizes, and 4 nm Si NCs exhibit the highest efficiency.

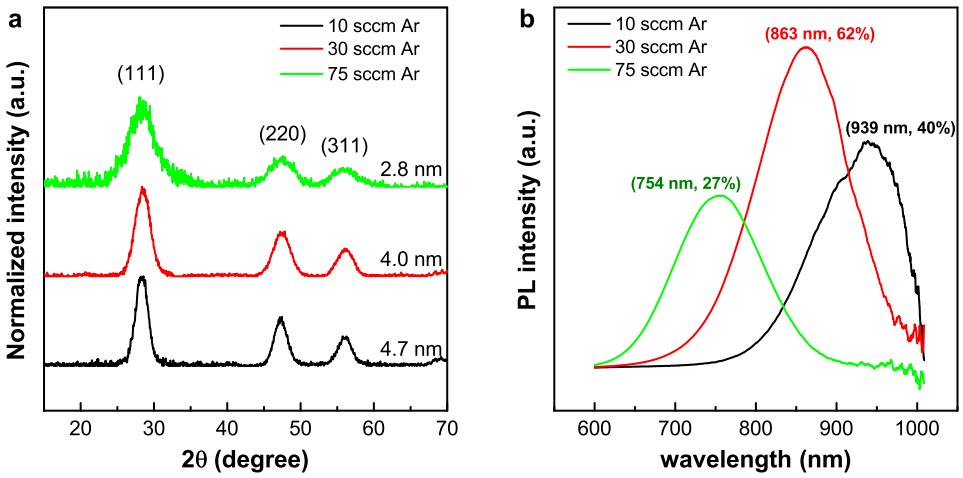

Figure 3.2: (a) XRD spectra of Si NCs with three different sizes. (b) Photoluminescence of Si NCs with corresponding sizes.

It should be noted that the PLQY has a dependence on the concentration of NCs in solution. Figure 3.3 shows the PLQYs of Si NCs measured in chloroform at various concentrations. As solution concentration decreases from 20 mg/ml to 0.0001 mg/ml, the PLQY of Si NCs shows a plateau at $\sim$ 40% until 5 mg/ml, and goes up with decreasing concentration, reaching the maximum $\sim$ 75% at 0.1 mg/ml, then dramatically decreases with further dilution. If we assume a random close packing model, the inter-particle spacing at 20 mg/ml is estimated to be $\sim$ 15.5 nm, which indicates that the coupling between particles is quite weak. Thus the low QYs for solutions denser than 5 mg/ml is probably due to the inefficient absorption of excitation source light. When the solution concentration gets lower than 0.1 mg/ml, the emission intensity of NCs is very weak and the collection of emitted photons could be an issue. Therefore, the QYs is decreasing as solution concentration is reduced. Due to this concentration dependence, the PLQY measurements for Si NCs are usually taken at a solution concentration $\sim$ 0.1 mg/ml.

Hydrosilylated Si NCs have been successfully integrated into hybrid NC-organic LEDs[18], and the external quantum efficiency $\sim$ 9% has been achieved. To further improve the device performance for future commercial use, a fundamental understanding of electrical transport is needed in the Si NCs, and it is one of the most important

motivation for this thesis work.

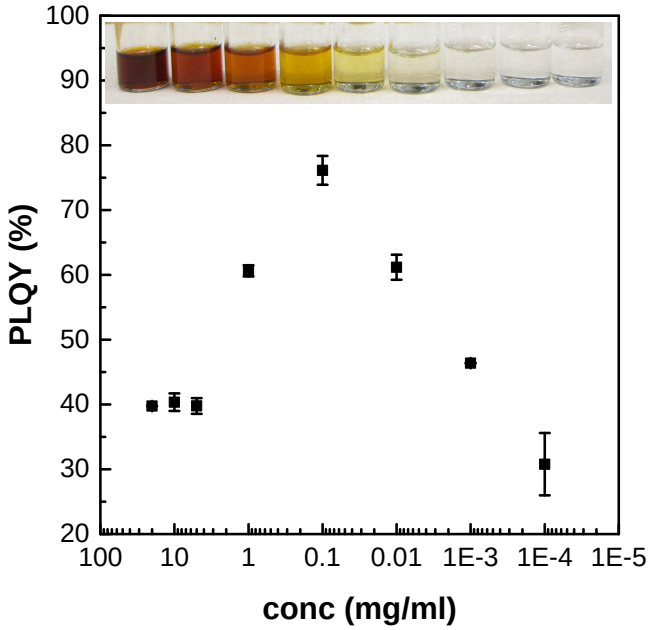

Figure 3.3: PLQYs of Si NCs in chloroform at various concentrations. The insert shows the picture of corresponding Si NC solutions. From left to right, the concentration of Si NCs in mg/ml is 20, 10, 5, 1, 0.1, 0.01, 0.001, 0.0001 and neat chloroform as reference, respectively. The Si NCs are $\sim$ 4 nm in diameter, and thermally hydrosilylated with 1-dodecence. The error bars show the standard deviation of PLQYs from 5 measurements for each concentration.

3.3 Self-assembled ordered Si NC arrays

Monodispersed colloidal NCs with controlled shape can self-assemble into long-range-ordered periodic structures, known as superlattices[48]. They have important technological uses as photonic materials[94,95], and also provide convenient model systems for studying fundamentals of crystallization and melting[96,97]. Also, the ordering of NCs is related to the electrical transport in NC solids. As we discussed in the last chapter, one of the typical disorders in NC systems is the packing disorder.

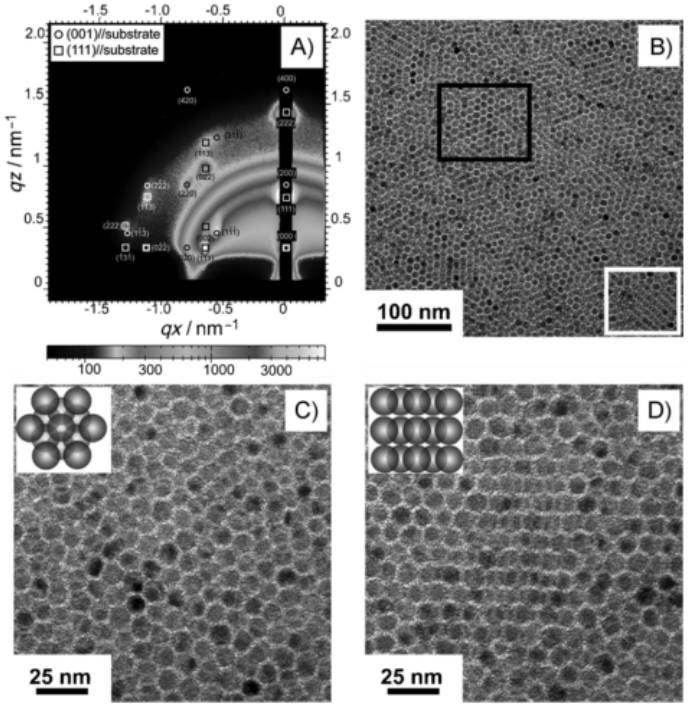

Figure 3.4: (a) GISAXS pattern from a Si NC superlattice. The pattern indexes to a FCC superlattice structure. (b-d) TEM images of Si NC superlattices. In (b), highlighted area with black rectangle corresponds to a (111)-oriented FCC superlattice, highlighted area with white rectangle corresponds to a $(11\bar{2})$ superlattice. (c) TEM image of a (111)-orientated domain, inset: depiction of a [111] projection. (d) TEM image for a $(11\bar{2})$-oriented domain, inset: depiction of a $[11\bar{2}]$ projection[98].

Most of the NC films used in the electronic devices are glassy films produced from spin coating or dip coating process. To minimize the packing disorder, a superlattice of NCs is a desired structure. Superlattices have been demonstrated in various NC systems[99,100] and mixtures of NCs (binary systems)[96,97]. Details about preparation of locally ordered NC solids (colloidal glasses) and NC superlattices can be found in the review[48]. Si NC superlattices have also been reported[98]. These particles were synthesized from thermal decomposition of hydrogen silsesquioxane (HSQ) followed by HF etching. Organic ligands of 1-dodecene were attached onto Si NC surface through thermal hydrosilylation, and a size-selective precipitation was performed to produce monodispersed Si NCs. The superlattices were formed by drop casting from a chloroform solution, as shown in Figure 3.4.

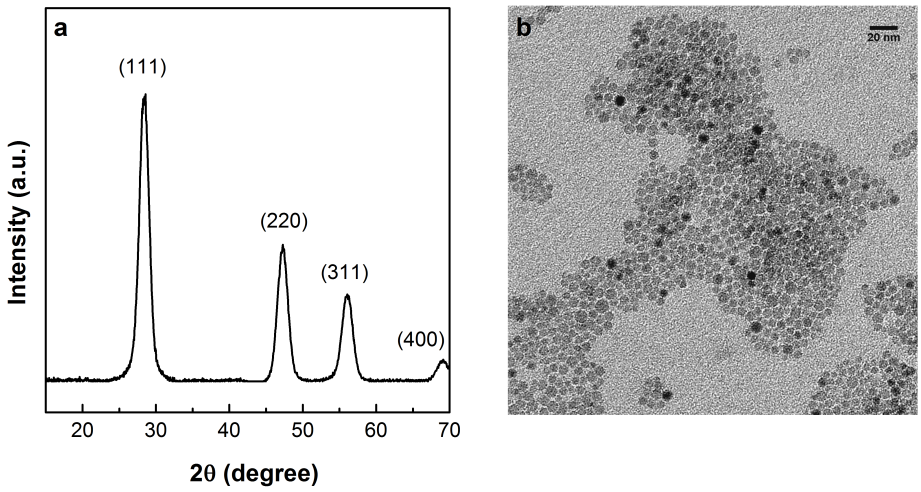

Figure 3.5: (a) XRD spectra of Si NCs with average diameter 6.7 nm. (b) TEM image for Si NCs hydrosilylated with 1-dodecene.

Initial attempts have been made to form ordered Si NC arrays in this thesis work. For easy imaging, large Si NCs with diameter $\sim$ 6.7 nm were synthesized with pressure $\sim$ 1.7 Torr. Figure 3.5 shows the XRD spectrum for as-produced Si NCs and TEM image for hydrosilylated Si NCs with 1-dodecene. The TEM sample was simply made by drop-casting from a dilute Si NC solution in chloroform. As shown in Figure 3.5, a submonolayer of Si NCs is formed on the lacey carbon grid, and the film exhibits local

ordering. Further optimization for film preparation is needed to obtain a superlattice from these Si NCs.

3.4 Conclusions

Si NCs with H termination can be produced from the nonthermal plasma method, and the particle size can be easily tuned by varying the argon flow rate. Organic ligands are attached onto NC surfaces to achieve colloidal stability as well as strong photoluminescence. As will be discussed in the following chapters, these organic ligands inhibit the electrical transport and other surface engineering techniques need to be developed in Si NCs to passivate NC surface and improve the electrical conductivity.

3.5 Experimental methods

Plasma conditions. Si NCs shown in the Figure 3.2 were synthesized from L122 reactor as shown in Figure 3.1. The plasma reactor is a Pyrex tube with a 10 mm outer diameter which then expands to a 25 mm outer diameter. Precursor gas silane (5% in helium) of 13 sccm and carrier gas argon were introduced into the reactor from the top. Argon gas flow rates of 10 sccm, 30 sccm, and 75 sccm were used for 4.7 nm, 4.0 nm and 2.8 nm Si NCs, respectively. Hydrogen gas of 100 sccm was injected from one side arm into the afterglow region of the plasma. The pressure used for all samples was 1.4 Torr. Plasma was excited in the upper portion of the Pyrex tube by applying 50 $\sim$ 65 W power to a pair of copper ring electrodes. The bottom electrode was grounded and the other was connected via a matching network to a 13.56 MHz radiofrequency power supply. Si NCs shown in Figure 3.5 with diameter $\sim$ 6.7 nm were produced with 16 sccm SiH_4, 16 sccm Ar, and 130 sccm H_2. The pressure was 1.7 Torr, and the nominal power was 75 W.

Hydrosilylation reaction. Thermal hydrosilylation reaction was carried out in a 5:1 (v:v) mixture of mesitylene and 1-dodecene in a glass bulb with refluxing at 215 °C for 2 h until clear colloids were obtained. The excess solvent was evaporated after reaction and hydrosilylated Si NCs were redispersible in nonpolar solvents (e.g., chloroform). All solvents used in the synthesis were well dried and degassed to avoid oxidation of NCs.

XRD. XRD was performed using a Bruker-AXS microdiffractometer with a 2.2 kW sealed Cu X-ray source at 40 kV and 40 mA (wavelength 0.154 nm). The XRD patterns were recorded for Si NC films impacted on glass substrates.

PL spectroscopy. The PLQYs of these Si NCs were measured in a custom-built system consisted of a light-emitting diode (LED) with excitation source at 395 nm, an integrating sphere and a USB2000 spectrometer from Ocean Optics. PL samples were made in air-free environment.

TEM. The bright field TEM employed FEI Tecnai T12 operated at 120 kV accelerating voltage. The TEM sample was prepared by drop casting a submonolayer of Si NCs directly onto a copper lacey carbon grid covered with a continuous carbon film (5 nm thick).

Chapter 4

Carrier Transport in Films of Alkyl-Ligand-Terminated Si NCs[†]

Si NCs have shown great promise for electroluminescent and photoluminescent applications. In order to optimize the properties of Si NC devices, however, electronic transport in Si NCs films needs to be thoroughly understood. Here we present a systematic study of the temperature and electric field dependence of conductivity in films of alkyl-ligand-terminated Si NCs, which to date have shown the highest potential for device applications. Our measurements suggest that the conductivity is limited by the ionization of rare NCs containing donor impurities. At low bias, this ionization is thermally activated, with an ionization energy equal to twice the NC charging energy. As the bias is increased, the ionization energy is reduced by the electric field, as determined by the Poole-Frenkel effect. At large bias and sufficiently low temperature, we observe cold ionization of electrons from donor-containing NCs, with a characteristic tunneling length of about 1 nm. The temperature- and electric-field-dependent conductance measurements presented here provide a systematic and comprehensive picture for electron transport in lightly doped nanocrystal films.

[†]Portions of this chapter have been published in the manuscript by Ting Chen, Brian Skinner, Wei Xie, Boris I. Shklovskii and Uwe R. Kortshagen in Journal of Physical Chemistry C (doi:10.1021/jp5051723)

4.1 Introduction

Semiconductor nanocrystals (NCs) have great potential for thin-film optoelectronics, such as solar cells[101] and light emitting diodes[102] due to their size-tunable electronic properties[103,104] and solution processability[48]. Among the different materials for semiconductor NCs, silicon (Si) has attracted substantial interest because of its abundance and low toxicity. Significant progress has been made in developing synthetic methods to prepare high quality Si NCs[14], achieving controllable doping[23,80,105], and integrating NCs into high performance optoelectronic devices. Such devices include hybrid organic-Si NC solar cells[106] and light emitting devices with external quantum efficiency approaching 9%[18]. Since most device applications rely on electrical conduction through films of NCs, understanding the fundamental mechanisms of the carrier transport in NC films is necessary to improve device performance.

While a number of studies have examined electrical conduction in group II-VI semiconductor NCs[19,54,107], the electronic transport in Si NC films is still poorly understood. Most transport studies thus far have focused on Si NCs embedded in an oxide matrix or covered by an oxide shell, and Fowler-Nordheim tunneling[108], space-charge-limited current (SCLC)[108,109], and hopping[110] transport mechanisms have been identified in these systems. Electrical conduction in H-terminated Si NCs has also been studied, and SCLC[111] and hopping[112] conduction mechanisms have been considered to describe the experimental results. However, for alkyl-ligand-terminated Si NCs, which to date have exhibited the best performance in photoluminescent and electroluminescent applications[17,18], the fundamental electronic transport mechanisms have not yet been studied. A fundamental study of the electronic transport mechanisms in this system is therefore needed.

In this work, we investigate the electronic transport in thin films of alkyl-ligand-terminated Si NCs by studying the temperature- and electric-field-dependent conductance. A vertical two-terminal structure is employed, and the electrical transport in the NC films is examined over a range of temperatures (300 $\sim$ 10 K). While these studies have been performed with a focus on films of Si NCs, we expect that many of our conclusions apply to other nanocrystal materials as well.

4.2 Structural characterization of Si NCs

The crystallinity and particle size of the alkylated (hydrosilylated) Si NCs were examined using X-ray diffraction (XRD) and a high resolution transmission electron microscope (HRTEM). Figure 4.1a shows a typical wide-angle out-of-plane 2θ - ω diffraction pattern (coupled scan) for drop-cast 1-dodecene alkylated Si NCs. Well-defined peaks indicating silicon diamond structure were observed, and the mean NC diameter was estimated to be ~ 4 nm using the Scherrer equation[92]. The NC size was also confirmed from HRTEM image as shown in Figure 4.1b, and the standard deviation of the size distribution is within $\sim 10\%$ of the peak size. Clear lattice fringes indicate that particles are single crystalline.

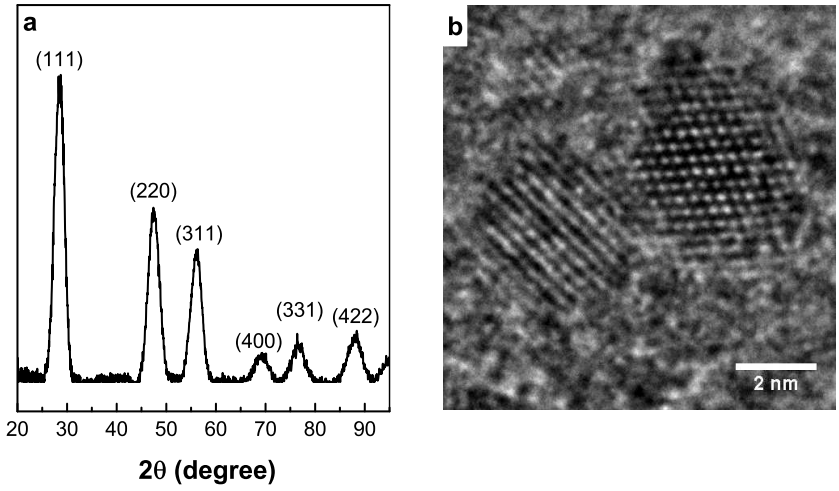

Figure 4.1: (a) XRD pattern and (b) High Resolution TEM image for Si NCs alkylated with 1-dodecene in a solution mixture of 5:1 mesitylene:1-dodecene.

4.3 Time and temperature dependence of conductance

NC films spin-coated onto glass substrates pre-patterned with bottom Al electrodes were smooth, continuous, and devoid of pinholes, as shown in the atomic force microscopy (AFM) image Figure 4.2a. Electrical measurements were conducted with the two-point probe geometry as shown in Figure 4.2b. A cross-sectional scanning electron microscopy

(SEM) image of the device is displayed in Figure 4.2c, in which the electrodes and Si NC film are labeled. The thickness of the Si NC film is about 180 nm. At low bias, the current-voltage (I-V) characteristics show ohmic behavior, so that the conductance $G = I/V$ is voltage-independent. The presence of a measurable ohmic response suggests that, even though our films are not intentionally doped, there is a noticeable concentration of carriers in the system independent of the drive voltage. This indicates the presence of a certain level of unintentional doping in the film. This picture is confirmed by measurements of the temperature dependence of the conductance, presented below.

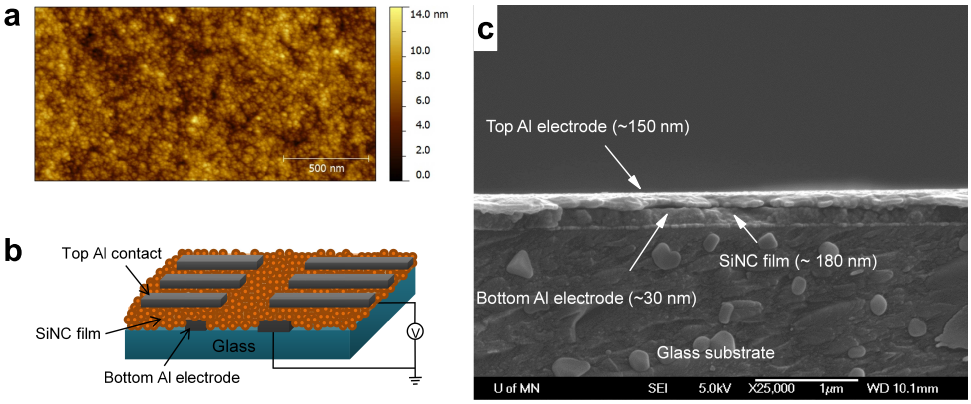

Figure 4.2: (a) AFM height image of 1-dodecene alkylated Si NC films. (b) Schematic cross-sectional diagram of the two-terminal vertical structure of our devices (not to scale). The active areas are square 2 mm^2 and 4 mm^2, respectively. (c) SEM image of the device cross section.

The measured conductance of our films at room temperature is plotted in Figure 4.3a as a function of time. During these measurements, the film was kept inside the nitrogen-filled glovebox with oxygen and water levels less than 0.1 ppm and I-V curves were recorded at different times t (with $t = 0$ corresponding to freshly made films). The NC film conductance exhibits a clear aging effect, with G increasing by more than two orders of magnitude over the course of the first 2 week and then remaining almost constant over several months. Freshly made films show conductance that varies from 10^{-9} to 10^{-8} S and the conductance of completely-aged films reaches 10^{-7} to 10^{-6} S. Figure 4.3b displays the current-voltage characteristics of films measured as freshly

made and after aging for two months; ohmic behavior can be seen in both curves. We attribute the aging effect to an increase in the tunneling rate between NCs, likely caused by a slow physical rearrangement of NCs or adsorption of water molecules, as we discuss in more detail below.

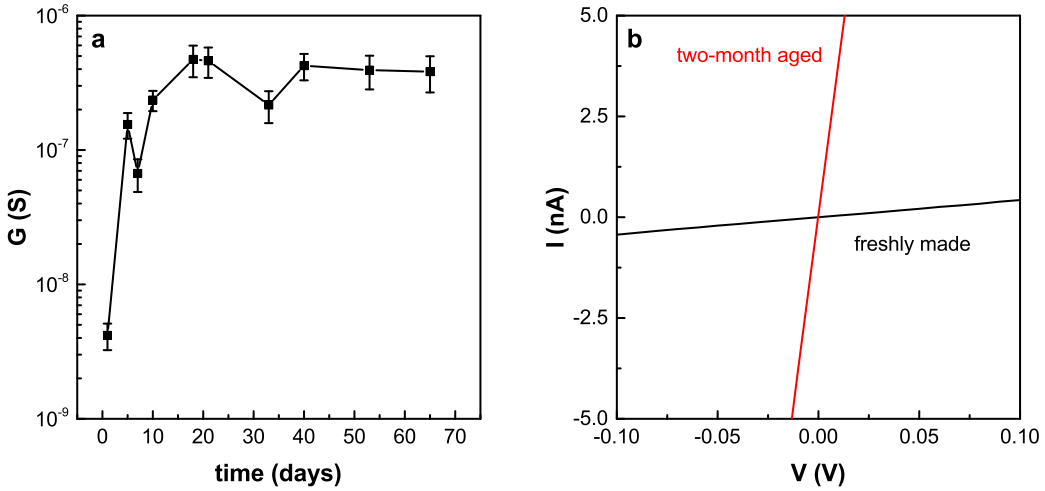

Figure 4.3: (a) Time dependence of electrical conductance for thin films of 1-dodecene alkylated Si NCs at room temperature as the films were kept inside a nitrogen-filled glovebox (oxygen and water level below 0.1 ppm). Black squares represent the average conductance of five devices at each time point, with error bars indicating the standard deviation. (b) Current-Voltage (I-V) characteristics measured for a typical Si NC film as freshly made ($t = 0$) and after aging at room temperature after two months ($t = 65$ days).

The temperature dependence of the ohmic conductance was measured for each film when it was freshly made, and after storing inside the glovebox for 1 week and for 2 weeks, since these time periods represented three typical stages of aging. For the following discussion, we refer to these three stages as freshly made, 1-week-aged and 2-week-aged. The ohmic conductance was measured with a fixed low voltage bias ($\sim$ 100 mV) while cycling the temperature from 300 to 120 K. For each sample, we find that the temperature-dependent conductance data is reversible: the conductance returns to its original values after warming up to 300 K, indicating that the sample remains stable during the temperature cycling. In general, the conductance of an insulating disordered

system, like our NC films, decreases with decreasing temperature and can typically be described by

$$G \propto \exp\left[-\left(\frac{T_0}{T}\right)^{\gamma}\right] \tag{2.19}$$

where the temperature exponent γ depends on the transport mechanism and T_0 is a characteristic temperature[55]. Situations with $\gamma = 1$, in general, correspond to nearest-neighbor hopping (NNH), where the conductance arises primarily from tunneling events between neighboring NCs. On the other hand, $\gamma = 0.5$ and $\gamma = 0.25$ correspond to Efros-Shklovskii variable-range hopping (ES-VRH) and Mott variable-range hopping (M-VRH), respectively. These mechanisms arise in situations where the current is carried primarily by cotunneling events between non-neighboring NCs. In different temperature regimes, different charge transport mechanisms can dominate[55].

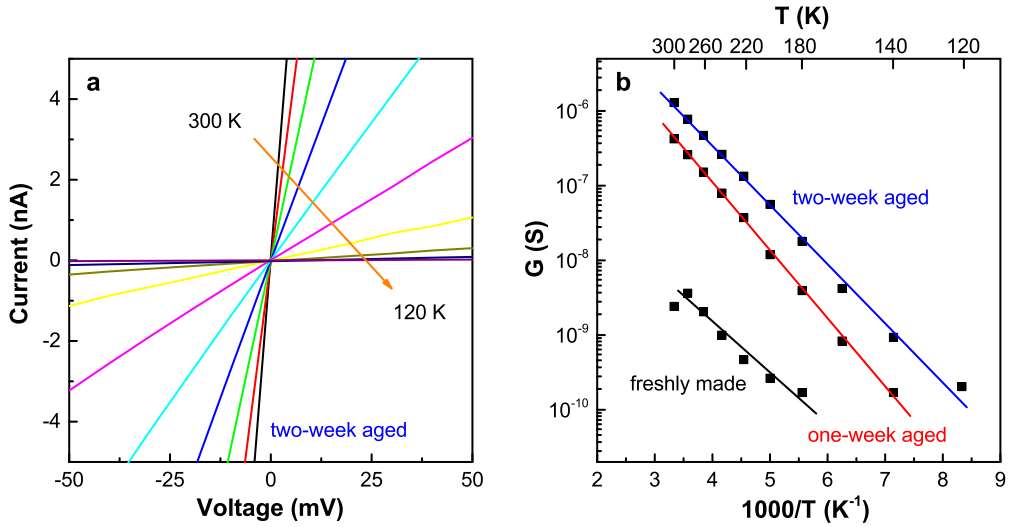

Figure 4.4: (a) Current-voltage (I-V) curves in the low bias regime (bias = 100 mV) at variable temperatures from 300 to 120 K for a typical film of 1-dodecene alkylated Si NCs after aging at room temperature for 2 weeks. Conductance decreases as temperature decreases. (b) Temperature dependence of the ohmic conductance when the film was freshly made, 1-week-aged and 2-week-aged in the range $120 < T < 300$ K. The data are displayed in log-linear scale and the error bar for the measurement of each data point is smaller than the symbol size used in this figure. Solid lines are linear fits for each aging stage.

I-V curves in the low bias regime for the 2-week-aged film are displayed in Figure 4.4a for a range of different temperatures. No hysteresis is observed between the forward and reverse voltage sweeps, and *I-V* curves are highly symmetric around the origin, implying that the ohmic behavior persists for all measured temperatures. Similar behavior is observed in the films that were freshly made and 1-week-aged. For all films, the conductance decreases with decreasing temperature, and we observe a linear dependence of ln G on T^{-1}, suggesting $\gamma = 1$, for all three aging stages. The data can, in principle, be plotted against either T^{-1} or $T^{-1/2}$ in order to compare which of these dependencies gives a more consistent fit. In our case, however, these plots alone are not enough to make clear the power of T because the temperature range is limited by the very small current, as seen in Figure 4.4b. Here we interpret our data with an Arrhenius dependence. As we show below, this interpretation is consistent with the electric field dependence of the conductivity.

Figure 4.4b displays Arrhenius plots of the conductance versus temperature for the same Si NC film measured at each of the three stages. As discussed above, the observation of $\gamma = 1$ in these plots suggests that the carrier transport corresponds to NNH throughout the measured interval of temperature. In this case, the temperature T_0 in equation 2.19 can be associated with an activation energy $E_a = T_0/k_B$, where k_B is Boltzmann constant, so that

$$G \propto \exp\left[-\frac{E_a}{k_B T}\right] \tag{2.11}$$

The value of the activation energy is obtained by measuring the slope of the Arrhenius plot of conductance. This process gives $E_a = 135 \pm 13$ meV, 180 ± 2 meV and 165 ± 2 meV for the freshly made, 1-week-aged and 2-week-aged stages, respectively. These activation energies are much smaller than the Si band gap, which indicates that the current is carried by a finite, temperature-independent concentration of electrons within the conduction band rather than by electrons activated from the valence band. In other words, our films have a noticeable amount of unintentional doping, as mentioned above. The source of this doping remains unclear, although, as we discuss below, it is apparently at the level of less than about one donor (or acceptor) per NC. Below we will assume that we deal with donors.

The activation energy of ~ 160 meV that appears in our films is associated with the

energy required to ionize a donor-containing NC. To understand the activation energy that arises from this ionization process, consider first that in the ground state of the system every conduction band electron resides in one of the rare NCs that contain a positive donor charge, and so every NC is electro-neutral. When such a donor-containing NC is ionized and its conduction band electron is removed to a distant NC that does not contain a donor (an empty NC), the electron becomes free from donors and is able to hop freely between nearest-neighboring NCs. Such free electrons are responsible for the films conductivity. In this ionized state the system has two charged NCs, one with a positive donor and another with a negative electron, and so the ionization process costs an energy $2E_c$, where E_c is the charging energy associated with adding a net charge e to an electrically neutral NC. In equilibrium, such ionization processes occur with the same rate as electron-donor recombination processes. The latter rate is proportional to n^2, where n is the concentration of free electrons on empty NCs. As a result of this equilibration the activation energy associated with the concentration n and the conductance G is equal to E_c.

The value of E_c can be estimated by noting that when a charge is introduced to the interior of an NC, it causes dielectric polarization of the interior of the NC and the surrounding dielectric environment. Since the internal dielectric constant ε_{NC} is much larger than the external dielectric constant ε_i, the great majority of a given internal charge is distributed at the surface of the NC by the dielectric response. The resulting Coulomb self-energy of the NC can therefore be thought of as equivalent to that of a metallic sphere in a uniform dielectric medium[29]. This allows one to estimate the charging energy as

$$E_c = \frac{e^2}{4\pi\varepsilon_0\varepsilon_r d} \tag{4.1}$$

where d is the particle diameter, ε_0 is the permittivity of vacuum and ε_r is the effective dielectric constant for the NC film. It has been pointed out that ε_r of the NC array is not simply the dielectric constant ε_i of the insulating medium between NCs, but that the effect of neighboring NCs polarization response to an applied field should also be considered. In this case, the effective dielectric constant of the NC film can be estimated

from the canonical Maxwell-Garnett formula[44]

$$\varepsilon_r \approx \varepsilon_i \frac{\varepsilon_{NC} + 2\varepsilon_i + 2\phi\left(\varepsilon_{NC} - \varepsilon_i\right)}{\varepsilon_{NC} + 2\varepsilon_i - \phi\left(\varepsilon_{NC} - \varepsilon_i\right)} \tag{2.8}$$

where ϕ is the volume fraction of NCs and $\varepsilon_{NC} = 11.7$ is the dielectric constant of Si. Since the dielectric constant of organic ligands is much lower than that of Si and these ligands fill a relatively small fraction of the system volume, we can safely neglect the dielectric response of these ligands and set $\varepsilon_i = 1$. From the refractive index measurement, the film density ϕ was determined as 42%, and this gives $\varepsilon_r = 2.46$. If one assumes that NCs within our film are arranged in a random close packing, then the spacing δ between the surfaces of neighboring particles is about 0.6 nm. This separation between particles is reasonable because the 1.4 nm-long organic ligands on the particle surface should largely lie flat against the surface in order to achieve lower energy states. Inserting $\varepsilon_r = 2.46$ into equation 4.1 gives an estimate for the charging energy of $E_c =$ 146 meV, which is in good agreement with the experimentally measured value of the activation energy.

Our observation of NNH conduction for all films, regardless of age, suggests that for all of these films the level of (unintentional) doping is less than about one donor per NC. Indeed, in the opposite case of large doping, NCs become charged in the ground state to avoid electron occupation of energetically expensive $1P$ quantum states of the NC[29], and the activated behavior is replaced by ES-VRH with temperature exponent $\gamma = 1/2$. Our films show no sign of this $\gamma = 1/2$ behavior, and so we conclude that the level of doping is small.

We now turn our attention to the aging effect of the conductance. As shown above, the activation energies for the films as freshly made and 2-week-aged are close, while the conductance at these two stages varies by two orders of magnitude. In general, such an increase in the conductance could arise either from an increase in the number of carriers or from a reduction of the tunneling barrier between neighboring NCs, which enhances the characteristic frequency of electron tunneling events. An increase in the donor concentration with film age seems unlikely, since chemical changes in the NCs can occur only at the surface, and surface states generally create deep mid-gap states rather than shallow donor levels. There is also no evidence that our films are heavily compensated by any such deep surface states, since this compensation would lead to a pinning of

the chemical potential to the donor levels and therefore to an activation energy $2E_c$ rather than E_c[55]. We therefore conclude that the increase in conductivity comes from a reduction in the tunneling gaps between neighboring NCs. Such a reduction could arise, for example, if the spacing between NCs were gradually reduced as leftover interstitial solvent molecules evaporate and NCs readjust. The tunneling barrier could also be reduced without rearrangement of NCs, for example by adsorption of water molecules in the interstitial gaps, which would provide easier tunneling pathways for electrons. The effects of adsorbed water on film conductivity for semiconductors and oxides have been reported previously[113], and Rastgar *et al.* observed conductivity increase by up to an order of magnitude due to water adsorption in thin films of Si NCs[112].

As mentioned above, the origin of the free carriers in our films is not clear yet. The incorporation of impurities during synthesis is one possible source, but further work is needed to confirm this hypothesis.

The aging effect may also be accelerated by the weak exposure to sunlight, which is known to produce charge separation of carriers. A detailed exploration of the effect of light exposure on device aging is left for a later work.

4.4 Electric field dependence of conductance

As discussed above, thermally activated NNH provides a good description of our data at low bias voltage, within the regime of ohmic response. Here we present results for conductivity at larger bias, focusing our attention on films that have been aged for 2 weeks. At a temperature of 300 K, the *I-V* curve for bias voltage between 0 and 20 V shows significant hysteresis, as displayed in Figure 4.5a. The forward scan is also plotted in log-log scale in Figure 4.5b. This hysteretic behavior is generally observed in systems where injected charge carriers become trapped. In our measurements this hysteresis was dramatically suppressed at lower temperatures (below 260 K), which suggests that carrier trapping is thermally activated. The nearly complete disappearance of hysteresis at low temperatures indicates that the electron transport is not affected by traps at these low temperatures, and that below 260 K the electron transport mainly occurs through the interior quantum states of each particle rather than through particle surface trap states[107].

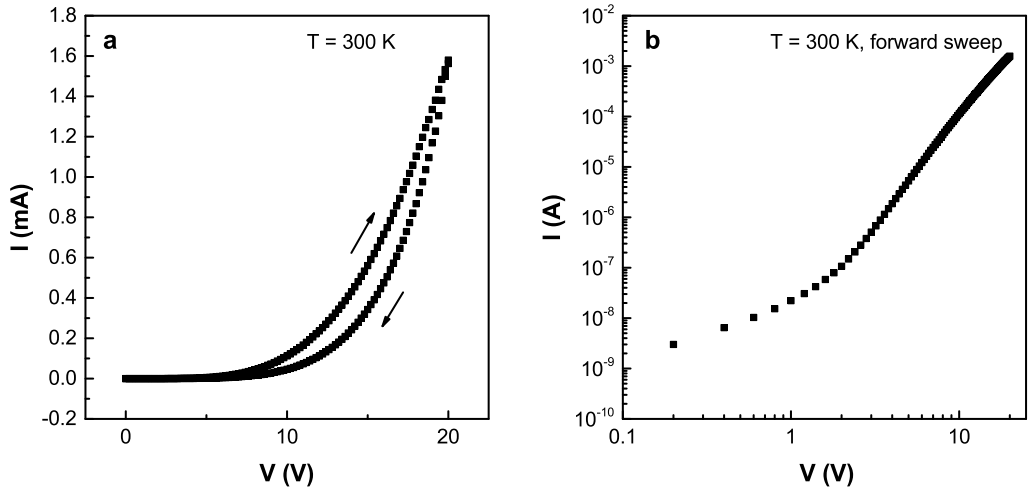

Figure 4.5: (a) Current-voltage (I-V) curves in the high bias regime at 300 K for a typical Si NC thin film after aging at room temperature for 2 weeks. Hysteresis can be seen from the forward and backward sweeps. (b) Forward sweep for I-V at 300 K in log-log scale.

The temperature dependence of the film I-V characteristics at high bias is shown in Figure 4.6a for temperatures ranging from 260 to 80 K. Below 80 K, the I-V curves are temperature independent within the measurable voltage range and coincide with the curve corresponding to 80 K. To interpret our measurements, we first consider the temperature range of 260 to 80 K. In the low field regime (below 1 V), the slope of the I-V curves in log-log scale is close to 1, which indicates ohmic behavior. As the temperature is decreased, the current in the ohmic regime decreases according to the Arrhenius law, as described in the previous section.

For high electric fields (bias voltage above 1 V), the current acquires a stronger dependence on voltage until about 16 V, when the I-V curves for different temperatures converge. In the regime between 1 and 16 V, the I-V characteristics are strongly non-ohmic, but retain an Arrhenius-like dependence on temperature. Figure 4.6b displays the conductance G versus T at various voltages from 300 to 10 K. Activation energies in the temperature range 300 to 80 K at each voltage point can be extracted from the slope of each curve, and are plotted in Figure 4.6c.

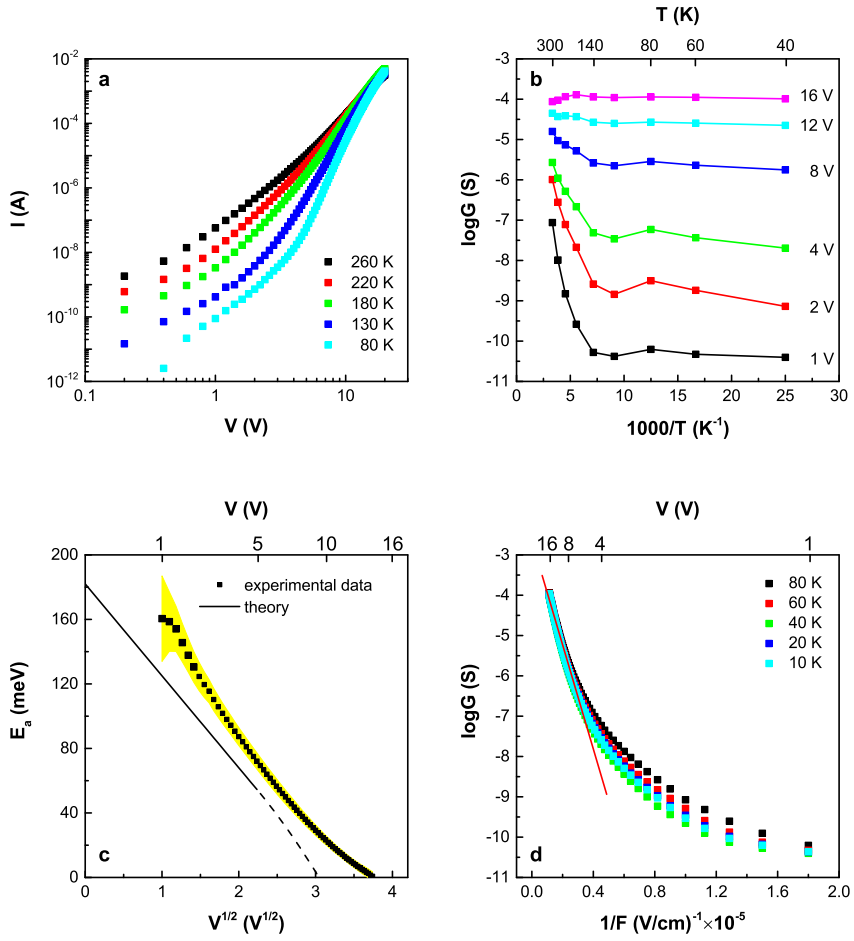

Figure 4.6: (a) Current-voltage (I-V) curves in the high bias regime at variable temperatures from 260 to 80 K for a typical Si NC thin film after aging at room temperature for 2 weeks. (b) Arrhenius plot of the temperature dependence of the film conductance at different voltages from 1 to 16 V. With voltage increasing, the slope of curves in the range of 300 to 140 K decreases. (c) Activation energy E_a for the temperature range $140 < T < 300$ K at various voltages from 1 to 16 V. The black square is the activation energy fit from ln G versus $1/T$ at each voltage point, and the yellow shadow represents the uncertainty of the activation energy caused by the linear fit. The solid black line shows the theoretical result up to 5 V described in equation 4.2 and the dash line indicates the linear dependence on voltage above 5 V. (d) Semi-log plot of conductance versus inverse electric field ($1/F$) for the same device in the temperature range $10 < T < 80$ K and at bias voltages below 16 V. The red solid line is the linear fit for data from 5 to 16 V.

With increasing voltage, the activation energy is seen to decrease. This behavior is likely a manifestation of the Poole-Frenkel effect[114,115], which describes the reduction of the ionization energy for a donor-containing NC by application of an electric field F (see Figure 4.7a and b). In particular, such an electric field creates an addition to the Coulomb potential of the donor that depends linearly on distance, so that the electric potential has a maximum in the direction opposite the electric field at a distance $r_{max} = (e/4\pi\varepsilon_0\varepsilon_r F)^{1/2}$. The value of this potential maximum determines the energy necessary to ionize the donor, which becomes $2E_c - 2(e^3F/4\pi\varepsilon_0\varepsilon_r)^{1/2}$ as shown in Figure 4.7b. Consequently, at large enough voltage that the reduction in the ionization energy is much larger than k_BT, the conductance follows[115]

$$G \propto \frac{k_BT}{\sqrt{e^3F/4\pi\varepsilon_0\varepsilon_r}} \exp\left[\frac{-E_c + \sqrt{e^3F/4\pi\varepsilon_0\varepsilon_r}}{k_BT}\right] \tag{4.2}$$

where, again, the activation energy is equal to half the donor ionization energy. This reduction in the apparent activation energy by an amount proportional to the square root of the applied voltage indeed provides a good description of our data, as shown in Figure 4.6c. We note that at sufficiently large fields, r_{max} becomes smaller than the spacing $d + \delta$ between neighboring NCs, and equation 4.2 should lose its validity. At such large fields the ionization energy is determined by the energy required to activate the electron to the nearest-neighboring NC in the direction opposite the field as shown in Figure 4.7c, and the activation energy decreases linearly with the applied voltage as shown by the dash line in Figure 4.6c. This large-voltage regime can be called the Poole limit of Poole-Frenkel effect and corresponds to V larger than $\sim$ 5 V in our samples.

At even larger bias voltages, V greater than $\sim$ 16 V, the ionization energy is completely overwhelmed by the downstream electric potential, and the activation energy for the conductance is eliminated, so that the current becomes essentially temperature-independent. As one can see, at such large fields the conductance at $T = 80$ K is enhanced by more than 6 orders of magnitude relative to its value at 1 V.

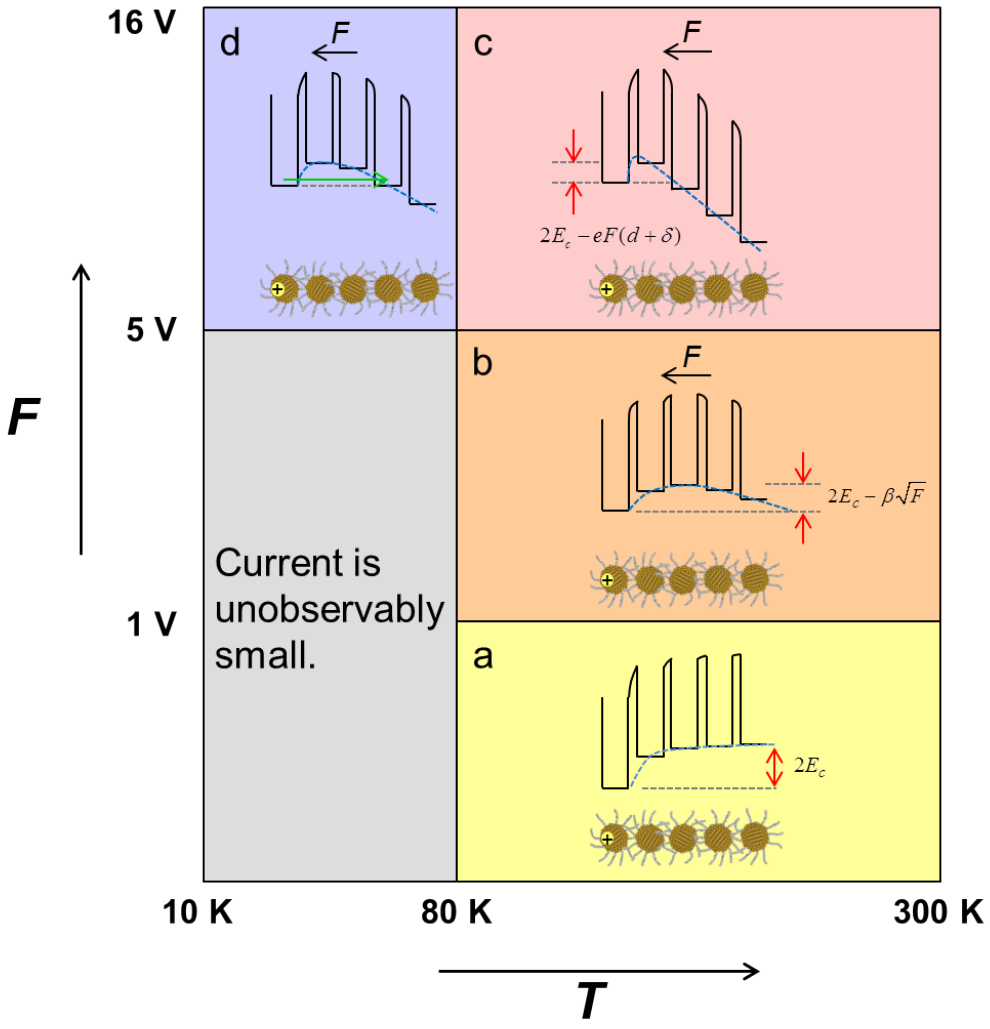

Figure 4.7: Ionization of a rare donor-containing NC. (a) $T > 80$ K and very weak electric field F ($V < 1$ V). The ionization energy $2E_c$, necessary to create two charged NCs is shown. (b) $T > 80$ K and strong electric field F (1 V $< V <$ 5 V), which facilitates ionization, reducing ionization energy $2E_c$ by Poole-Frenkel mechanism ($\beta = \sqrt{e^3/4\pi\varepsilon_0\varepsilon_r}$). (c) $T > 80$ K and strong electric field F (5 V $< V <$ 16 V), the ionization energy linearly depends on the electric field. (d) $T < 80$ K and strong electric field F (5 V $< V <$ 16 V) when ionization happens by tunneling directly between non-neighboring NCs (cold ionization).

We now turn our attention to the low temperature regime, $T < 80$ K, where the observed current is essentially independent of temperature at all bias voltages for which the current is measurable. At such small temperatures the thermal energy is insufficient to ionize donor-containing NCs. Instead, cold ionization processes dominate the conductance. In particular, at small enough biases that the electric field F is much smaller than a critical field $F_0 = 2E_c/e(d+\delta)$, the electron tunnels directly from donor-containing NC to an empty NC at a distance $x \sim 2E_c/eF$[116]. This tunneling distance depends on the applied electric field, with higher electric field implying shorter tunneling distance, as illustrated in Figure 4.7d (For example, at a bias voltage of 4 V, the tunneling distance $x \sim 14.4$ nm, which is about three NC spacings.) The resulting ionization rate is proportional to $\exp(-2x/\xi)$, where x is the hopping distance and ξ is the characteristic tunneling length (localization length). As a result, the conductance is

$$G \propto \exp\left[-\frac{x}{\xi}\right] \tag{4.3}$$

Rewriting equation 4.3 with $x \sim 2E_c/eF$ gives

$$G \propto \exp\left[-\frac{2E_c}{e\xi F}\right] \tag{4.4}$$

Therefore, the characteristic tunneling length ξ can be extracted from a linear fit of ln G versus $1/F$. In Figure 4.6d, ln G is shown to depend linearly on $1/F$ in the range of $5 < \text{V} < 16$ V, and the corresponding characteristic length ξ is determined to be 1.1 ± 0.1 nm. This characteristic tunneling length describes the typical distance over which the electron wave function is localized spatially, and is related to the decay length a of the electron wave function in the gap between two NCs. In particular, when an electron tunnels to a distant, non-neighboring NC at a distance x, its tunneling trajectory involves passing through a chain of intermediate NCs (see Figure 4.7c), and the decay of the electron tunneling amplitude is dominated by passage through the gaps between neighboring NCs along the chain. As a consequence, the tunneling amplitude is suppressed by a factor $\sim \exp[(-2\delta/a) \times (x/(d+\delta))]$, so that the characteristic tunneling length is given by $\xi \sim (a(d+\delta)/\delta)$[117]. From this relation we estimate that the decay length a for the hydrosilylated SiNC film is ~ 0.14 nm, which is similar in magnitude to previous measurements of the tunneling decay length in PbSe NCs[39] and simple

estimates using the work function of Si.

At lower electric field ($V < 5$ V), the film conductance G deviates from the linear relation of ln G versus $1/F$ at large electric field, which could be caused by the presence of rare, atypical NC pairs with very close spacing. Such bridges may play a role in our geometry because we drive current across a thin film between large area contacts[118].

As is the case for larger temperatures, at sufficiently large electric fields that $F > F_0$, which corresponds to $V \geq 16$ V, the bias voltage is strong enough to generate electrons by inducing tunneling directly between neighboring NCs.

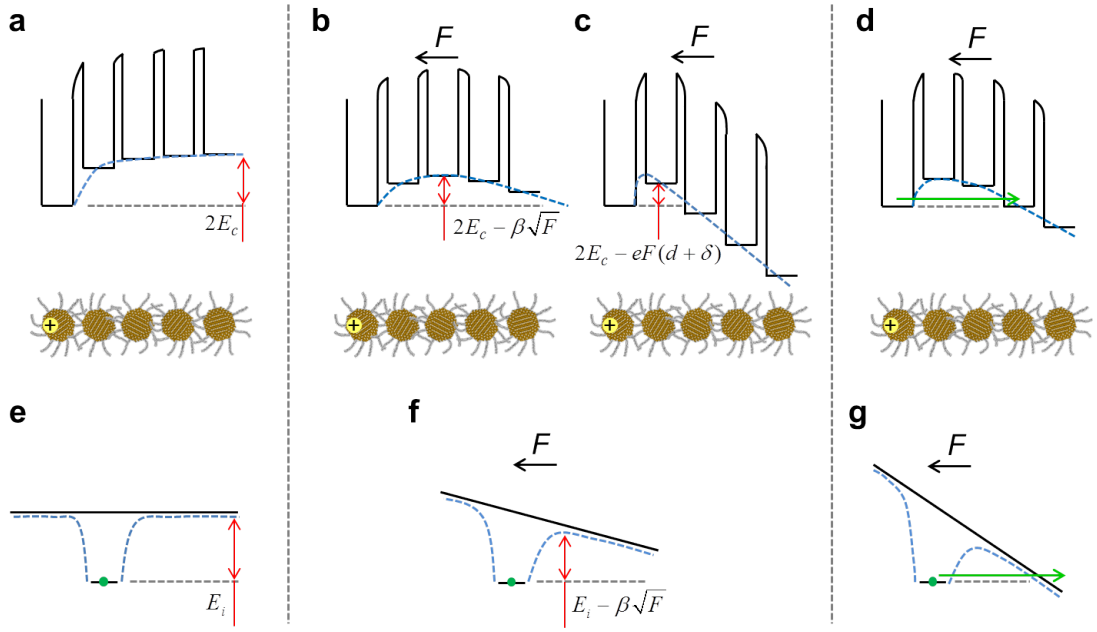

Figure 4.8: Analog of electrical transport in NC arrays and bulk semiconductors.

By way of analogy, we note that if one compares the NC array described above with a lightly doped n-type bulk semiconductor, then empty NCs play the role of the conduction band, in the sense that they provide the states through which free electrons carry the system current. Donor-containing NCs play the role of conventional donors, and the ionization energy $2E_c$ is analogous to the donor binding energy E_i as shown in Figure 4.8a. The concentration of electrons on empty NCs, n, plays the role of the

electron concentration in the conduction band. Aslo, the applied external electric field lowers the activation barrier by Poole-Frenkel effect in both cases (see Figure 4.8b), but there is a critical value at which Poole-Frenkel loses its validity in NC arrays. Cold ionization is also similar in bulk and NC semiconductors as displayed in Figure 4.8c.

Even though our explanation of the experimental data has used the language of donors and conduction electrons in our films, the analysis applies to acceptors and conducting holes as well. Unfortunately, due to the extremely low mobility of carriers in Si NCs[81], it is probably not easy to verify the type of dopants from Hall measurements or transistor measurements. To further investigate this unintentional doping in our materials, one could introduce a small amount of intentional n-type or p-type dopants into the Si NCs and deduce the carrier type for the unintentionally doped sample from the change in the film conductivity.

4.5 Conclusions

In summary, we have investigated the temperature and electric field dependent electron transport in thin films of alkyl-ligand-terminated Si NCs. Our interpretation of the data is based on assumption that a small fraction of NCs contains a donor. At low bias, the film conductance is determined by electrons activated from donor-containing NCs to empty NCs, between which they move via nearest neighbor hopping. As the bias is increased, the conductance is enhanced by the electric field, which causes a reduction in the activation energy as determined by Poole-Frenkel effect. At large bias and sufficiently low temperature, we observe cold ionization of donor-containing NCs via electron tunneling to distant empty NCs with characteristic tunneling length 1 nm. Compared with other Si NCs used in electrical measurements, the light doping and good surface passivation of our alkyl-ligand-terminated Si NCs provide a good platform to study carrier transport in a lightly doped nanocrystal film, which, to the best of our knowledge, has not been explored previously. The unintentional doping that appears in our Si NCs enables us to probe the electronic transport under low electric field, and the good surface passivation ensures that the measurements were not hindered by surface defects. Our work constitutes the first thorough study of carrier transport in a lightly doped nanocrystal film, and we believe that many of the results obtained here for Si

NCs apply to other NC materials as well.

4.6 Experimental methods

Synthesis of Si NCs. The Si NCs for which data are shown were synthesized in a nonthermal rf (13.56 MHz) plasma reactor, as described previously[91]. The reactor was a Pyrex tube with 10 mm outer diameter which then expands to 25 mm outer diameter, and the reactor pressure was held constant during synthesis at 1.4 Torr. The flow rates of precursors were 13 sccm (standard cubic centimeters per minute) of silane and 35 sccm of argon. Hydrogen gas was injected at 100 sccm in the 25 mm expansion region of the reactor tube. Particle size was controlled by adjusting the argon flow rate. The nanoparticles have spherical shape and are virtually 100% crystalline. To achieve stable colloids, the Si NC surfaces were functionalized with alkyl ligands in a liquid-phase thermal hydrosilylation reaction with a 5:1 mixture of mesitylene and 1-dodecene[119]. A clear colloidal dispersion of particles was obtained after a 2 h refluxing period at 215 °C. After functionalization, the alkyl ligands were covalently bonded to the particle surface and individually dispersed Si NCs were produced[15]. Before device fabrication, the alkylated Si NCs were purified by dispersion/precipitation for three rounds. It is well known that the introduction of a nonsolvent that is miscible with the original dispersing solvent can destabilize the NC dispersion and cause NCs to aggregate and precipitate[48]. Therefore, the synthetic by-products or unreacted ligands are left in the solution, helping to produce a clean NC material. For alkylated Si NCs, anhydrous chloroform and acetonitrile were used as the solvent and nonsolvent, respectively, and a centrifugation process at 4600 rpm for 15 min was performed after each precipitation. After purification the Si NCs were redispersible in nonpolar solvents (e.g., chloroform). All solvents used in the synthesis and functionalization process were well dried and degassed to avoid oxidation of NCs.

XRD, TEM, AFM and SEM. The crystallinity and the size of Si NCs were characterized by XRD using a Bruker-AXS microdiffractometer with a 2.2-kW sealed Cu X-ray source at 40 kV and 40 mA (wavelength 0.154 nm). The XRD pattern was recorded for drop-cast films of 1-dodecene alkylated Si NCs on a glass substrate. The HRTEM employed FEI Tecnai G2 F-30 TEM with a Schottky field-emission electron gun operated

at 100 kV accelerating voltage. The sample for TEM was prepared by drop casting a submonolayer of Si NCs directly onto a copper lacey carbon TEM grid covered with a continuous carbon film (5 nm thick). The morphology of the spin-coated Si NC films was studied by a Bruker NanoScope V Multimode scanning probe microscope working in tapping mode. The probes used were silicon cantilevers with integrated tapping mode tips fabricated by NanoWorld AG (Arrow^{TM} NCR, resonant frequency 285 kHZ, spring constant 42 N/m). Cross-sectional SEM images were obtained by a field emission gun JEOL 6500 with accelerating voltage 5 kV and working distance 10 mm.

Device fabrication. Vertical two-terminal devices were constructed on microscope glass slides in a nitrogen-filled glovebox. The glass substrates were pre-cleaned by sequential ultrasonication for 10 min each in acetone, methanol and isopropyl alcohol, and were dried by nitrogen blow. The glass was then placed in a M. Braun thermal evaporator and 30 nm thick Al strips were deposited through a shadow mask on the glass to serve as the bottom electrodes. Following the deposition of the electrodes, Si NCs films were spin-coated from a 50 mg/ml dispersion in anhydrous chloroform at 1500 rpm for 60 s. The resulting film thickness was about 180 nm, determined from the cross-sectional SEM images. Finally, Al top electrodes with 150 nm thickness were thermally evaporated through another shadow mask on top of the Si NC films with 2 mm^2 and 4 mm^2 active areas, thus finishing the devices. The deposition rates used for both electrodes were controlled at 0.5 Å/s. The devices were then transferred into another nitrogen-filled glovebox for subsequent electrical measurements without any air exposure.

Current-voltage Measurement. The current-voltage (*I-V*) characteristics of the NC films were recorded in a Desert Cryogenics (Lakeshore) probe station in a nitrogen-filled glovebox with Keithley 236 and 237 source measuring units and homemade LabVIEW programs. Low temperature measurements employed a Lakeshore 331 temperature controller with a fixed ramp rate of 2 K/min. All measurements were carried out in the dark and under vacuum at pressure $\sim 10^{-3}$ Torr.

4.7 Future work

To improve the film conductivity, one can minimize the activation energy E_a which can be reduced by increasing the size of NCs or the effective dielectric constant of the NC film. Generally speaking, large NCs conduct better than small ones since they have smaller charging energy. Regarding to the effective dielectric constant, it can be tuned by the film density ϕ and the surrounding medium. Using shorter ligands can decrease the inter-particle spacing, and thus denser films can be achieved. The surrounding medium (voids between NCs) can be changed with infilling a high dielectric constant material through atomic layer deposition method, such as HfO_2 or ZnS. Careful considerations need to be taken when choosing the infilling materials because the deposition process may introduce surface defects on the NCs or the infilled material may build up an even higher tunneling barrier between NCs, impeding the conductivity of NC film. Also, the nucleation of the infilled materials could be an issue because of the hydrophobic ligands on the NC surface.

We deduce that this system is probably lightly doped with some unknown source of dopants during the plasma synthesis process. The most probable impurity is oxygen. In the bulk Si, O can occupy an donor-like impurity level ~ 0.16 eV below conduction band. Compared with P ~ 0.045 eV below conduction band, B ~ 0.045 above valence band in bulk Si, O is not a shallow donor. However, different from the bulk semiconductor, dopants in nanocrystals can be auto-ionized without thermal activation[8]. The energy level of the electronic states increases with decreasing nanocrystal size due to the quantum confinement effects, the energy difference between nanocrystal and bulk material leading to a confinement energy. This confinement energy can exceed the Coulomb interaction between the ionized impurity and the carrier when the nanocrystal size is below a critical radius. This can also be seen from another way. Assume the radius $d/2$ of a NC is smaller than or comparable to the effective Bohr radius $a_B = \hbar^2\kappa_{NC}/me^2$ of the semiconductor, where $\kappa_{NC} = 4\pi\varepsilon_0\varepsilon_{NC}$, for Si, $a_B \approx 2.4\ nm$ and the Si NCs used in this work have an average size ~ 4 nm. Under this condition, the wavefunction of a donor electron is extended over the entire NC rather than localized around the impurity as in the bulk semiconductor. The energy of this delocalized donor electron is strongly affected by quantum confinement within the NC, and it sits at $1S$ level if assume only

one donor electron per NC. A single donor in a NC has a delocalized electron state when $d < 6a_B$ [120,121].

To verify this hypothesis, one can intentionally introduce minimum oxygen into the plasma reactor. The doping level needs to be controlled at less than 1 donor per 5000 NCs. This is based on a calculation assume an electron mobility $\mu \sim 10^{-6}$ $cm^2V^{-1}s^{-1}$ [81]. If we use the doping efficiency found in P-/B-doped Si NCs $\eta \sim 10^{-2} - 10^{-4}$ [81], we can estimate the required O_2 flow rate $\sim$ 0.13 sccm - 13 sccm. This can be easily achieved in the experiment with 1% O_2 diluted in Ar or pure O_2. It should be noted that the delivery of silane and oxygen needs to separated, otherwise oxygen would be consumed before reaching the reactor. Side arm injection with hydrogen may be one option. It is expected that the as-produced particles have tiny Si-O-Si peak (around 1030 cm^{-1}) and after hydrosilylation with 1-dodecene, PL quantum yields reach above 50%. This minimum amount doping should not affect PL at all.

We focus on 1:5 (v:v) dodecene in mesitylene capping ratio in this work, 1:1000 and 1:2000 have also been studied. The different ratios of dodecene in mesitylene lead to different ligands coverage on the NC surface. Unfortunately, there is no good way to precisely measure the ligand coverage on single NC so far. It has been shown that the ligand coverage has an effect on the LED performance from previous study, Si NCs with 1:5 capping ratio exhibited the best device performance. Therefore, Si NCs with capping ratio 1:5, 1:1000 and 1:2000 were examined in this work.

As shown in Figure 4.9, the transport mechanism in these three samples follows Arrhenius behavior and the activation energy E_a for each sample is calculated to be 165 $\pm$ 2 meV, 156 $\pm$ 1 meV and 118 $\pm$ 2 meV for 1:5, 1:1000 and 1:2000 sample, respectively. According to results obtained here, it seems like the capping ratio does not affect transport behavior in the Si NC films. Further work is needed to explore the reason behind the different device performance.

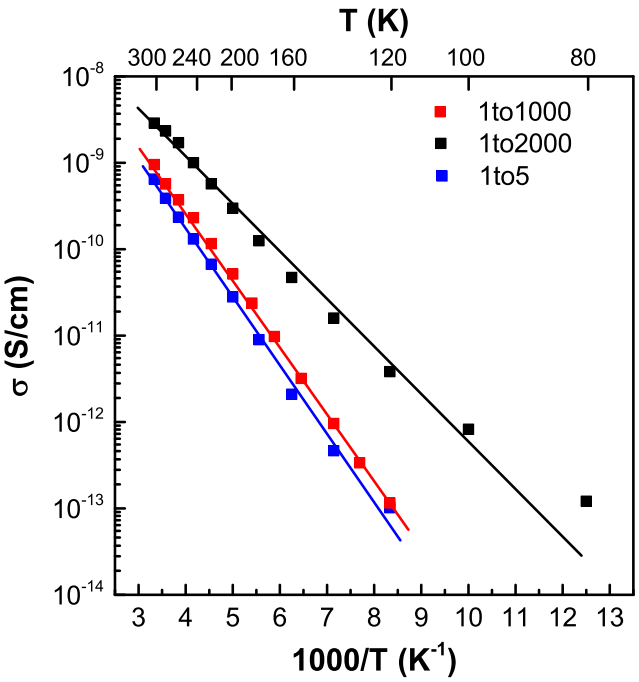

Figure 4.9: Temperature dependence of the ohmic conductivity for Si NC films with capping ratio of 1:5, 1:1000 and 1:2000 in the temperature range from 300 K to 80 K. The data are displayed in log-linear scale and the error bar for the measurement of each data point is smaller than the symbol size used in this figure. Solid lines are linear fits for each sample.

Chapter 5

How Many Electrons Make Semiconductor NC Films Metallic?

5.1 Introduction

During the past decades, significant efforts have been attempted to explore doping of semiconductor nanocrystals (NCs), which have shown great potential in optoelectronics applications, such as solar cells[122] and light emitting diodes[102] by virtue of their size-tunable optical and electrical properties[104] and low-cost solution-based processing techniques[123,124]. For these applications, conducting films are usually required, and the introduction of extra carriers can enhance the electrical conduction in NC films. Several strategies have been developed to introduce extra carriers in NCs. Remote doping, the use of donors as binding ligands in the vicinity of NC surface, has proved to increase conductivity by 12 orders of magnitude in PbSe NC films[1]. Electrochemical doping, with application of external gate voltage to tune the carrier concentration accurately and reversibly, has achieved success in conducting NC films[40,125]. Lately, stoichiometric control has been shown to dope lead chalcogenide NCs and switch majority carriers from n-type to p-type[71]. Additionally, electronic impurity doping in NCs, impeded by the synthetic challenges[8], also has seen some success in InAs[72] and CdSe[77] NCs. Still,

only a few carriers could be introduced into a single NC.

While many experimental studies have been directed towards increasing conductivity of NC films, there is still no answer to the fundamental question[19,126,127]: what is the condition for the metal-insulator transition (MIT) in a NC film? In a bulk semiconductor, the critical electron concentration n for the MIT depends on the Bohr radius a_B by the well-known Mott criterion[128]:

$$n_c a_B^3 \simeq 0.02, \tag{5.1}$$

where $a_B = 4\pi\varepsilon_0\varepsilon\hbar^2/m^*e^2$ is the effective Bohr radius, ε_0 is the vacuum permittivity, ε is the dielectric constant of the semiconductor, and m^* is the effective electron mass. It is obvious that a dense film of undoped semiconductor NCs in contact is an insulator, while a film of metallic NCs with the same geometry is a conductor. Therefore, a phase transition from insulator to metal occurs in the semiconductor NC films when the concentration of electrons n is above a critical value n_c. In other words, there exists an analog of the Mott criterion in a dense film of spherical semiconductor NCs. In this paper, we show that for Si NCs with $d = 8$ nm this criterion is

$$n_c a_B^2 a \simeq 0.5, \tag{5.2}$$

where $a \ll a_B$ is the decay length of an electron wave function outside of the NC. In other words, a much smaller distance, $0.3(a_B^2 a)^{1/3}$, plays the role of a_B in equation 5.1. This is a natural result. At the MIT, electrons inside a heavily doped NC, must be delocalized between neighboring NCs. For $a = 0.1$ nm, equation 5.2 gives $n_c = 9 \times 10^{20}$ cm^{-3}. Of course, this simple criterion for the MIT in NC films is valid only when NCs are in contact. Any insulating barrier between NCs leads to an exponential growth of n_c.

To verify our theory, we investigate the electron transport in dense films of phosphorus-doped, ligand-free Si NCs over a wide range of doping concentration. The Si NCs are produced from a gas phase nonthermal plasma method, which provides the opportunity to synthesize ligand-free NCs with low defect density[14] as well as achieve tunable doping[23,81].

In a lightly doped Si NC film with the average number of donors per NC, $N \ll 1$, the electron transport is activated[25], and the conductance G of the NC film follows the

Arrhenius law: $G \propto \exp(-E_c/k_BT)$, where $E_c = e^2/4\pi\varepsilon_0\varepsilon_r d$ is the charging energy, $\varepsilon_r \sim 3$ is the effective dielectric constant of the NC film[25,29].

For NC films with a few donors per NC, variable range hopping (VRH) has been observed[24,60,129], which agrees with theoretical predictions[24,29]. In this work, we explore even larger doping concentration with N up to 50 per NC or $n \lesssim 3\times10^{20}$ cm^{-3}. Over the entire range of doping concentrations under investigation, the film conductance follows Efros-Shklovskii (ES) law:

$$G \propto \exp\left[-\left(\frac{T_{ES}}{T}\right)^{1/2}\right], \tag{2.15}$$

where

$$T_{ES} = \frac{Ce^2}{4\pi\varepsilon_0\varepsilon_r k_B \xi}, \tag{2.16}$$

$C \simeq 9.6$ for semiconductor NCs[29]. With increasing doping concentration n, the localization length increases and exceeds the diameter of a NC, which indicates the approach to the MIT in the NC film. At $n \simeq 3\times10^{20}$ cm^{-3} the localization length is three times larger than the diameter of a NC. This experimental observation is in qualitatively good agreement with our theoretical prediction equation 5.2. Indeed, our equation 5.2 gives $n_c \simeq 9\times10^{20}$ cm^{-3}.

Additionally, we also study the dependence of localization length on the separation δ between NCs through controlled oxidation, and demonstrate that the localization length ξ decreases with increasing δ as $\xi \simeq ad/\delta$, consistent with theoretical work reported previously[117].

5.2 Critical doping concentration at MIT

In this section, we focus on calculation of the minimal concentration of electrons in a NC n_c, which makes arrays of semiconductor NCs metallic. First, we consider an isolated spherical NC with diameter d in vacuum. We assume that the electron concentration is so large that $na_B^3 \gg 0.02$. Therefore, each NC is filled by degenerate weakly interacting electron gas. It is characterized by the Fermi wave vector $k_F = (3\pi^2/g)^{1/3}n^{1/3}$, where

g is the number of equivalent minima in the conduction band. The Fermi velocity is $v_F = \hbar k_F/m^*$, and the density of states is

$$\nu(k_F) = \frac{g}{\pi^2}\frac{m^*}{\hbar^2}k_F. \tag{5.3}$$

Inside a NC, electrons are scattered by the ionized donors and the mean free path of an electron is[130]:

$$l = \frac{3\pi}{2g}a_B^2 k_F \tag{5.4}$$

(we omitted the logarithmic term which in our range of n is close to 1.)

In this paper, we consider the case $l \ll d$ when electrons move diffusively inside the NC (see Figure 5.1). The diffusion coefficient of electrons in a NC is $D_{NC} = v_F l/3$, and the characteristic time to reach the surface is

$$\tau_1 = \frac{d^2}{D_{NC}} = 3\frac{d^2}{v_F l} = 3\frac{m^*}{\hbar}\frac{d^2}{lk_F}. \tag{5.5}$$

The presence of the work function barrier U_0 leads to an exponential decay of the electron wave function outside a NC with the decay length $a = \left(\hbar^2/2mU_0\right)^{1/2}$, where m is the electron mass.

Now we focus on two NCs in contact (see Figure 5.1). There is only a small contact disc with radius $\rho = \sqrt{da/2} \ll d$ near the contact point of two NCs where tunneling between them easily happens (here we ignore facets of a NC, which strictly speaking is possible for a larger than lattice constant). We show below that at the critical doping concentration, $\rho k_F \simeq 1$, so that when an electron hits the contact disc along a classical trajectory it moves from one NC to another. Therefore, the tunneling probability is proportional to the ratio of the area of the contact disc $\pi\rho^2$ and the surface area of the NC πd^2. As a result, the typical time to move from one NC to another is:

$$\tau = \tau_1\frac{d^2}{\rho^2} = 6\frac{m^* d^2}{\hbar}\frac{1}{k_F l}\frac{d}{a}. \tag{5.6}$$

Now, let us consider a NC array in which identical spherical NCs are in contact and form a cubic lattice (see Figure 5.1). In ideal close-packed array of spherical NCs, each NC touches 12 neighbors. In reality, there is always some dispersion of NC diameters. It is known that in this case the average number of contacts per NC is required by

system stability to be 6[131]. Therefore, we assume that the number of contacts between neighboring NCs is always six. Thus, the time to escape from a NC is $\tau/6$ and the macroscopic diffusion coefficient D is:

$$D = \frac{1}{3}\frac{d^2}{(\tau/6)} = \frac{1}{3}\frac{\hbar}{m^*}\frac{l}{d}k_F a. \tag{5.7}$$

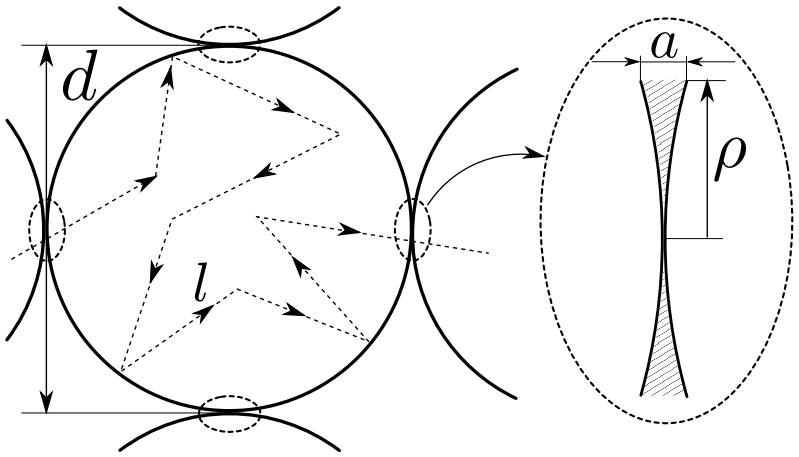

Figure 5.1: Quasiclassical transport of electrons in the lattice of spherical NCs with diameter d. NCs are touching each other. Tunneling between neighboring NCs occurs only in contact discs (see a thin tunneling barrier shaded in the enlarged contact disc). The radius of the disc is $\rho = \sqrt{ad/2}$ and the width of the disc is equal to the decay length a. Inside a NC, electrons are scattered by the ionized donors so that the mean free path $l < d$. An electron moves diffusively inside the NC, and tunnels from one NC to another once it reaches the contact discs.

The Einstein relation gives a the macroscopic conductivity $\sigma = e^2\nu D$ and the conductance between two neighboring NCs is

$$G(k_F) = d\sigma = \frac{e^2}{\hbar}\frac{k_F^3}{2\pi}a_B^2 a = \frac{e^2}{\hbar}\frac{3\pi n}{2g}a_B^2 a \tag{5.8}$$

(we use equations 5.3, 5.4, 5.7). The MIT occurs if the average conductance between two neighboring NCs G is equal to the minimal conductance G_m [49]:

$$G(k_F) = G_m \equiv \frac{e^2}{\hbar}\frac{1}{3\pi}L(k_F), \tag{5.9}$$

where

$$L(k_F) = \ln\left[\frac{\pi}{6} d^3 \nu(k_F) E_c\right] = \ln\left[\frac{g}{6\pi} k_F d \frac{d}{a_B} \frac{\varepsilon}{\varepsilon_r}\right]. \tag{5.10}$$

Here $(\pi/6)d^3\nu(k_F)$ is inverse spacing between NC energy levels near Fermi level. Equation 5.9 originates from the physical condition that the width of levels in each NC is large enough to eliminate charging energy E_c.

If we assume in zero approximation that $L = const$ we get from equations 5.8, 5.9: $n_c a_B^2 a = 0.02gL$. We show below that close to the critical concentration $L \simeq 4$. For Si this leads to equation 5.2.

To solve transcendental equation 5.9 more accurately for Si NCs we use $g = 6$, $m^* = 0.3m$, $\epsilon = 11.7$, $a_B = 2.4$ nm. Assuming that the electron affinity of Si is $U_0 = 4$ eV we get $a = 0.1$ nm in agreement with estimation from experimental results[25].

The effective dielectric constant ε_r of the NC array is estimated to be ~ 3 from the canonical Maxwell-Garnett formula[44] (the film density is assumed to be $\sim 50\%$). For touching Si NCs with diameter $d = 8$ nm in vacuum, solving equation 5.9 we get $n_c \simeq 9 \times 10^{20}\text{cm}^{-3}$ consistent with equation 5.2.

At the critical doping concentration n_c we get $k_F = 1.7$ nm^{-1}, $k_F\rho \simeq 1.0$, $L(k_F) = 4$ and $l = 7.6$ nm $< d$, which is consistent with experimental data $l = 3$ nm[132]. Thus, our assumptions are valid and equation 5.2 is a reasonable estimate for the critical concentration n_c.

Equation 5.2 was derived for $\delta = 0$. For a finite separation δ between NCs, conductance G acquires a factor $\exp(-2\delta/a)$, therefore:

$$n_c(\delta) = n_c \exp\left(\frac{2\delta}{a}\right) \tag{5.11}$$

In this case, MIT may prove to be unreachable. To improve chances to reach the MIT, one can design media between NCs with large a, which probably has been achieved.[41,53].

Let us return to the $\delta = 0$ case and discuss mobility μ in the metallic phase away from critical range of MIT, i.e. at $n > 2n_c$. There $\mu = 6/\pi Gned$, where factor $6/\pi$ accounts for difference between concentration of electrons inside NCs and average concentration

in the array. Using equation 5.8 we get the metallic mobility:

$$\mu = \frac{e}{\hbar}\frac{9}{g}\frac{a_B^2 a}{d}, \tag{5.12}$$

For chosen parameters, it is on the order of 1 $cm^2/V^{-1}s^{-1}$.

5.3 Characterization of P-doped Si NCs

Freestanding phosphorus (P)-doped Si NCs were synthesized in a nonthermal radio-frequency plasma reactor as reported previously[14]. We investigated six Si NC films with different P concentrations. We denote them using the nominal doping concentration $X_{P,nom}$, which is represented by the fractional flow rate, defined as $X_{P,nom} = [PH_3]/([PH_3] + [SiH_4]) \times 100\%$, where $[PH_3]$ and $[SiH_4]$ are the flow rates of phosphine and silane. The plasma synthesis conditions are shown in Table 5.1.

To quantify P incorporation in Si NCs, we utilized inductively coupled plasma optical emission spectroscopy (ICP-OES). Table 5.2 shows the P atomic fraction in Si NCs for each nominal doping concentration. We observe a monotonic increase in the incorporated P fraction with increasing nominal doping concentration, and the incorporation efficiency is about 50% when $X_{P,nom}$ is below 5%. However, this technique only measures the elemental composition, the concentration of active dopants or free electrons is still unknown.

Table 5.1: Plasma synthesis conditions for P-doped Si NCs

	units	**value**	**comments**
Ar	sccm	55	100%
SiH_4	sccm	0.4	100%
PH_3	sccm	0.028 - 0.66	15% in H_2
pressure	mTorr	900	actual
power	W	110	nominal
tube	inch	1	O. D., Pyrex
orifice	mm×mm	12×0.61	slit area

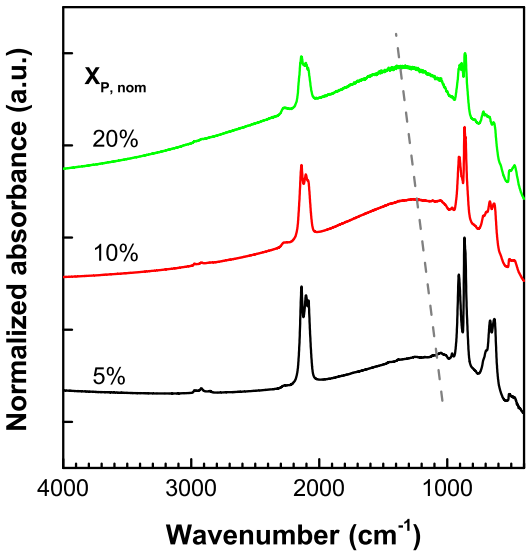

Figure 5.2: Fourier transform infrared (FTIR) spectroscopy spectra for nominally 5%, 10% and 20% P-doped Si NCs. The broad absorption feature is the localized surface plasmon resonance, and it shifts to higher wavenumbers with increasing nominal doping concentration (a dashed line is added as a guide to the eye). The electron concentration is estimated from the plasmonic peak position and shown in the Table 5.2. These Si NC films have been annealed at 125 °C overnight inside a nitrogen-filled glovebox before FTIR measurements. The annealing effect will be discussed in the next section.

For samples at sufficiently high doping concentration, we can determine the free electron concentration through localized surface plasmon resonance (LSPR). The position of the plasmonic peak depends on the free electron concentration n as described by the equation below[23]

$$f_{LSPR} = \frac{1}{2\pi}\sqrt{\frac{ne^2}{\varepsilon_0 m^*(\varepsilon + 2\varepsilon_m)}}, \tag{5.13}$$

where f_{LSPR} is the localized surface plasmonic resonance frequency, ε is the dielectric constant for bulk Si (11.7) and ε_m is the dielectric constant for the surrounding medium, taken as ~ 1 for nitrogen atmosphere in this study. As shown in Figure 5.2, the plasmonic peaks are at 1110, 1260 and 1360 cm^{-1} in the infrared absorption spectra and the free electron concentrations are $n = 1.9 \times 10^{20}, 2.3 \times 10^{20}$, and 2.8×10^{20} cm^{-3} for

5%, 10% and 20% P-doped Si NCs, respectively. No plasmonic peak for doping concentrations lower than nominal 5% can be seen in the measurement range. Based on Mott criterion, the MIT transition occurs if the electron concentration is above 1.4×10^{18} cm^{-3}. Therefore, P-doped Si NCs with $X_{P,nom} > 5\%$ are already metallic NCs.

We use XRD to estimate the diameters of NCs. Figure 5.3a shows well-defined XRD peaks corresponding to diamond cubic structure in P-doped Si NCs with nominal doping concentration $X_{P,nom}$ from 1% to 20%. The diameters of NCs shown in Table 5.2 are calculated from the peak broadening in XRD spectra with spherical correction[93]. As $X_{P,nom}$ increases from 1% to 20%, the NC diameter decreases from 8.1 nm to 7.1 nm. This size shrink is likely caused by H_2 etching[133], since PH_3 is diluted in H_2 with a volume fraction 15%.

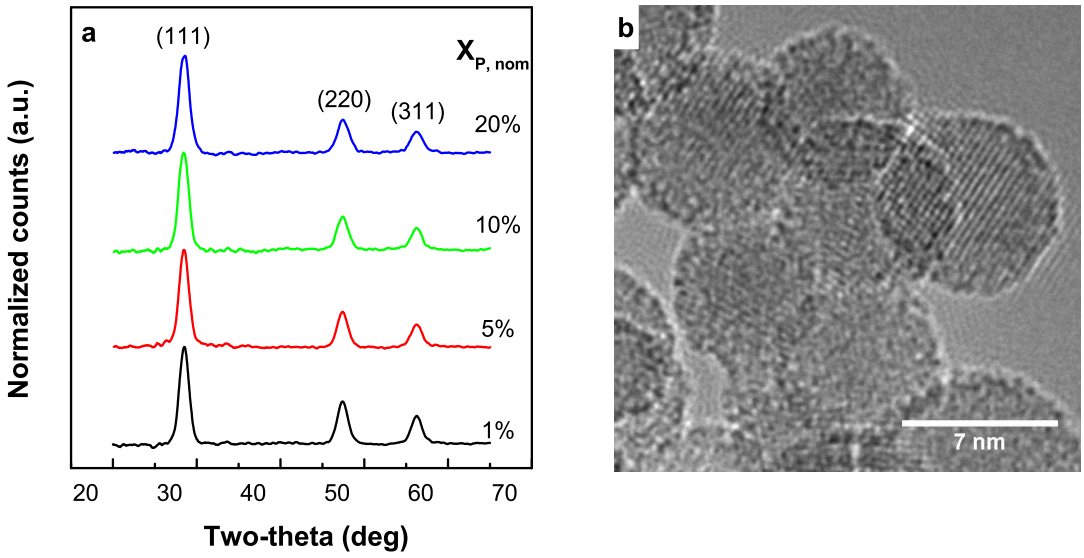

Figure 5.3: Structural characterization for P-doped Si NCs. (a) XRD spectra for P-doped Si NCs at $X_{P,nom}$ = 1%, 5%, 10% and 20%. (b) High resolution TEM image of nominally 10% P-doped Si NCs.

A typical bright field TEM image for nominally 10% P-doped Si NCs is shown in Figure 5.3b. The P doping does not alter the spherical shape of Si NCs and the NC size distribution is $\sim$ 15% for all NCs used in this study. With the diameter of NCs and the concentration of free electrons n, we can calculate the average number of electrons per

NC N. For $X_{P,nom} = 20$ %, we get $N \sim 50$ electrons per NC. All known parameters of Si NCs are summarized in Table 5.2.

Table 5.2: Parameters of Si NCs. $X_{P,nom}$ is the nominal doping, $X_{P,ICP}$ is the atomic fraction of P in Si NCs measured from ICP-OES, d is the average diameter of NCs, F is the plasmonic peak in cm^{-1} for Si NC films, n is the electron concentration estimated from the plasmonic peak for Si NC films, ξ is the localization length calculated from the electrical transport data.

$X_{P,nom}$%	$X_{P,ICP}$%	d, nm	F, cm^{-1}	n, $10^{20}cm^{-3}$	ξ, nm
1	0.46	8.1	-	-	1.4
2	0.82	8	-	-	1.9
3	1.56	8	-	-	6.1
5	2.38	8	1110	1.9	12.7
10	4.06	7.5	1260	2.4	20.6
20	6.98	7.1	1360	2.8	26.8

5.4 Hopping conductivity of P-doped Si NC films

Next, we examine the electrical transport in the P-doped Si NC films. Previous work has shown that low temperature annealing leads to an increase of the free carrier concentration in the P-doped Si NCs and this is primarily attributed to the reduction of dangling bond defects during the annealing process[23]. Figure 5.4a shows the IR absorption spectra of Si NCs at nominal 10% P doping concentration. The sample was measured as fresh-made, annealed at 125 °C for overnight, further annealed at 200 °C , 300 °C, and 400 °C for 10 min in each step. A weak plasmonic peak is observed in the fresh-made Si NCs and the peak position is located around 1000 cm^{-1}. With annealing at 125 °C for overnight, this broad absorption feature is enhanced and shifts to higher wavenumber $\sim$ 1260 cm^{-1}, indicating an increase in the free carrier concentration as reported before[23]. For the sample tested here, the N increases from about 26 to 50 per NC after annealing at 125 °C. Under further annealing at higher temperatures, the absorption peak stays at almost the same position but oxide peak (Si-O-Si) at $\sim$ 1045 cm^{-1} grows.

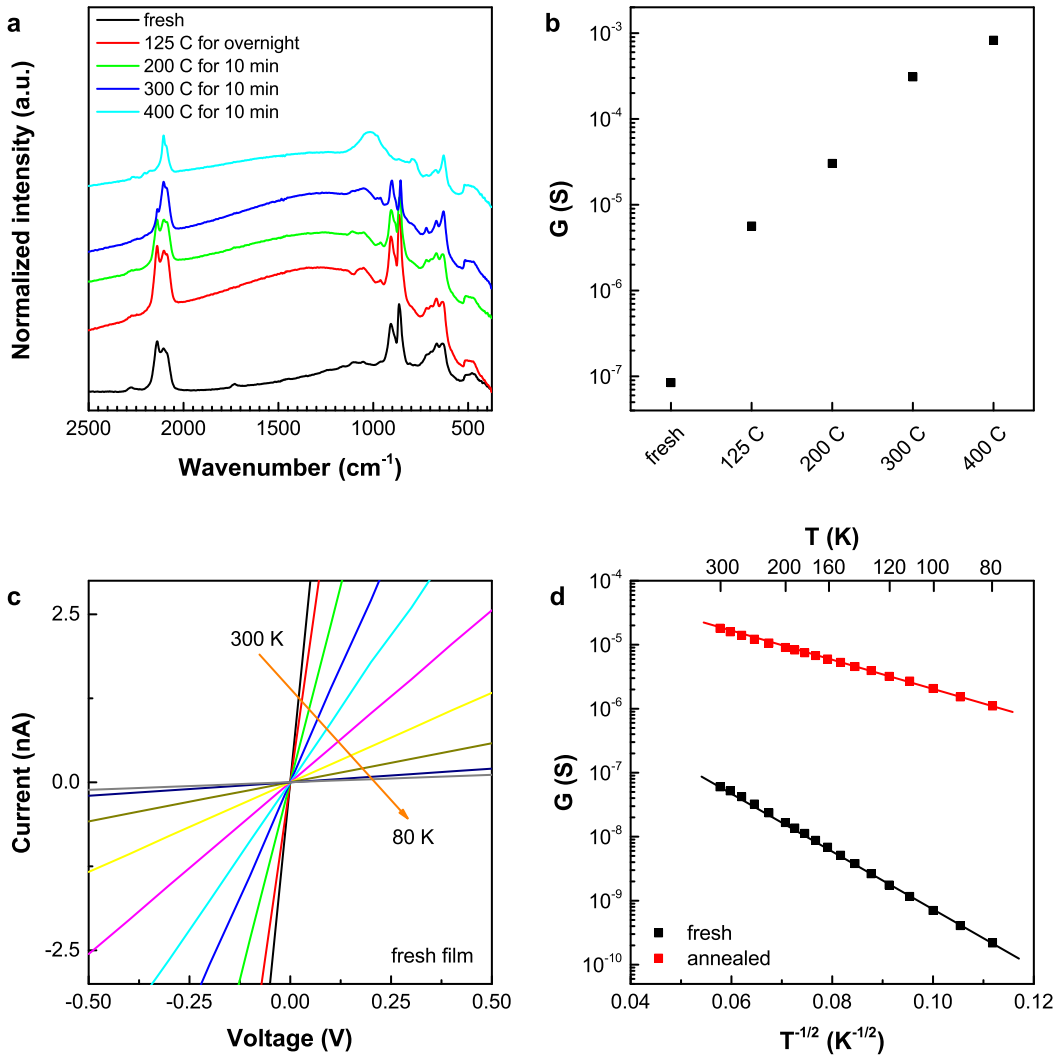

Figure 5.4: Structural characterization and electrical properties for nominally 10% P-doped Si NCs. (a) FTIR spectra for Si NCs as fresh-made, annealed at 125 °C for overnight, further annealed at 200 °C, 300 °C and 400 °C each for 10 min. (b) Ohmic conductance at room temperature for a typical Si NC film measured after corresponding treatment. (c) Current-voltage (I-V) curves in the ohmic regime at variable temperatures from 300 K to 80 K for a fresh-made film. (d) Temperature dependence of the ohmic conductance for a same film as fresh-made and annealed at 125 °C for overnight. The data are displayed in a log-linear scale, and the error bar for the measurement of each data point is smaller than the symbol size used in this figure. Solid lines are linear fits for each curve.

Oxidation of P-doped Si NCs still occurs even inside a nitrogen-filled glovebox with O_2 level less than 0.1 ppm, and the influence of oxidation on the electrical transport will be discussed later.

To study the annealing effects on the electrical properties, device films produced from nominally 10% P-doped Si NCs were treated under the identical annealing conditions as the IR samples. The current-voltage (I-V) characteristics exhibit ohmic behavior at low bias ($\sim$ 10 V), and the voltage-independent conductance $G = I/V$ is plotted against annealing temperature as shown in Figure 5.4b. Film annealed at 125 °C shows 100 times higher conductance compared with the fresh-made sample, and this is primarily attributed to the reduction of dangling bond defects upon annealing, consistent with the blue shift of the plasmonic peak. The increase in the free carrier concentration also helps transport between NCs as we show below. With further annealing at higher temperatures, the film conductance keeps increasing even though the plasmonic peak remains the same. We deduce that annealing could also cause physical rearrangement of NCs, reducing the tunneling gaps between neighboring NCs, and thus increasing the film conductance.

The electrical transport is examined over a range of temperature 300 $\sim$ 80 K. Figure 5.4c shows the highly symmetric I-V curves in the ohmic regime for fresh-made 10% P-doped Si NC film, implying that the ohmic behavior persists for all measured temperatures. Similar behavior is observed in the films after annealing treatment at 125 °C for overnight. The temperature dependence of the ohmic conductance for fresh-made and annealed films is displayed in Figure 5.4d. For both films, the conductance decreases with decreasing temperature, and we have a linear dependence of $\ln G$ on $T^{-1/2}$, suggesting ES-VRH conduction mechanism. The Zabrodskii reduced energy analysis[134] also indicates that our data are best fit with $T^{-1/2}$ and this interpretation is consistent with the rest analysis for our experiments. Compared with the fresh-made film, the annealed sample exhibits dramatic improvement in the film conductance, and a weaker temperature dependence is also observed. Moreover, the annealed sample demonstrates significantly improved stability. Fresh-made P-doped Si NC films show conductance degradation of 10 times within 24 hours even inside glovebox with O_2 level less than 0.1 ppm, while the annealed samples have stable conductance up to at least 2 weeks inside glovebox. As mentioned above, the enhanced conductance for annealed sample

is attributed to the reduction of surface defects as well as the shrink of tunneling gaps between NCs. Both of these two effects will lead to an increase in the localization length due to improved coupling between neighboring NCs. For the rest of electrical characterization, all P-doped Si NC films were annealed at 125 °C for overnight inside glovebox before measurement.

Figure 5.5 depicts the temperature dependence of the ohmic conductance G for P-doped Si NC films at nominal doping concentration from 1% to 20%. All P-doped Si NC films were produced from the same procedure and they exhibited similar film morphology regardless of nominal doping concentration. As shown in Figure 5.5a, the conductance of P-doped Si NC films monotonically increases with the nominal doping concentration. However, Si NC film at $X_{P,nom} = 20\%$ shows lower conductance than the film at $X_{P,nom} = 10\%$. The reason is not clear though. A linear dependence of $\ln G$ on $T^{-1/2}$ is observed for all doping concentrations suggesting ES-VRH conduction (equation 2.15). Zabrodskii analysis[58] (not shown here) confirms this result. The observation of ES-VRH indicates the presence of a strong disorder in our NC system so that a substantial fraction of NCs is charged in the ground state, otherwise nearest neighbor hopping behavior would be observed[25]. To have conduction in a NC system with majority neutral NCs in the ground state, one needs to activate an electron to jump from one NC to another. This process costs energy equal to twice charging energy, opening a hard gap centered at the Fermi level in the density of states. If the majority of NCs is randomly charged, the Coloumb potential will shift up and down the electron energy on NCs and the hard gap will be smeared and filled, resulting in a soft gap at the Fermi level[29,117].

We can extract the characteristic temperature T_{ES} and the localization length ξ from the slope of linear fits for $\ln G$ vs $T^{-1/2}$ using equation 2.16. We estimate the effective dielectric constant ε_r of the NC film from the canonical Maxwell-Garnett formula[44] (the film density is assumed to be $\sim 50\%$) and get $\varepsilon_r \simeq 3$. Close to the MIT, the dielectric constant may diverge. The character of this divergence in NC films is unknown. For the periodic array of metallic NCs which have diameter d and are separated at distance δ, the dielectric constant diverges logarithmically like $\ln d/\delta$ and at $d = 8$ nm, $\delta = 0.1$ nm, $\varepsilon_r \simeq 6$[135]. We assume that ε is constant and $\simeq 3$.

Knowing T_{ES}, the dielectric constant and using equation 2.16, we can get the localization length ξ. As the doping concentration increases, ξ grows from 1.4 nm at $X_{P,nom} = 1\%$ to 26.8 nm at $X_{P,nom} = 20\%$, as displayed in Figure 5.5b and shown in Table 5.2. This is the first time to observe doping-dependent localization length in a NC system. Liu *et al* reported a doping-independent localization length around 1 nm in CdSe NCs doped in electrochemical cell with highest doping level ~ 6 electrons per NC, and the insensitivity of localization length was attributed to high tunneling barrier of alkane ligands[24]. Numerical coefficient C ≈ 2.8 was used for calculating ξ in CdSe case, but ξ is only around 4 nm even with $C \approx 9.6$, still smaller than the diameter of a CdSe NC (6.2 nm).

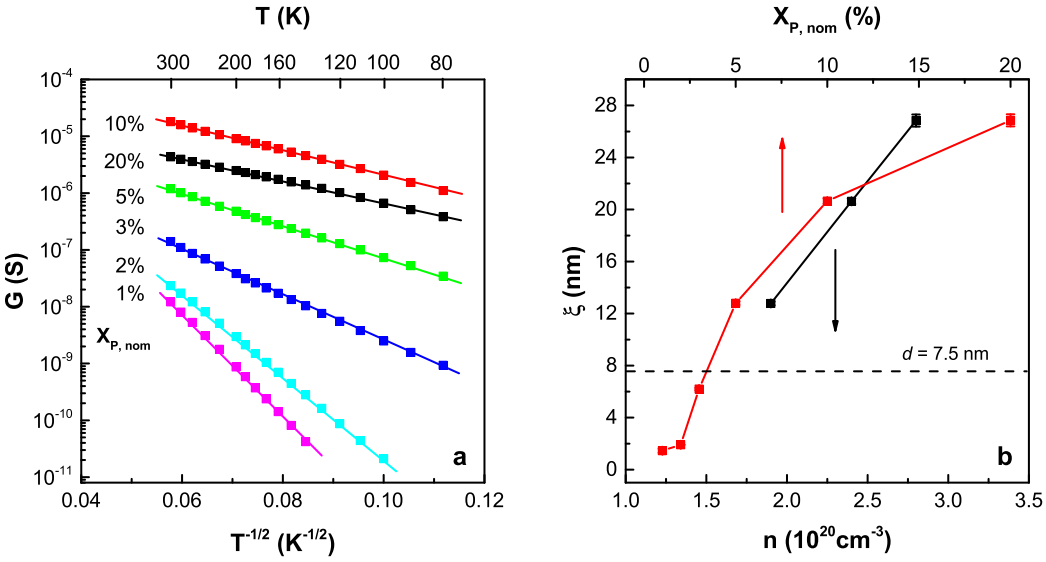

Figure 5.5: (a) Temperature dependence of the ohmic conductance for films made from Si NCs at different nominal P doping concentrations. Solid lines are linear fits for each doping concentration. (b) Localization length ξ versus the electron concentration in a NC n and nominal P doping concentration $X_{P,nom}$. Error bar for ξ comes from the uncertainty caused by the linear fit and it is as large as the symbol size.

For nominal doping larger than 5% and $n = 1.9 \times 10^{20}$ cm^{-3}, ξ exceeds the diameter of a NC. This indicates the approach to metal-insulator transition in the NC films. The data is in reasonable agreement with the predicted $n_c \simeq 9 \times 10^{20}$ cm^{-3} at the MIT.

5.5 Role of separation between NCs in electrical transport

The P-doped Si NCs are prone to oxidation if exposed to air. An oxide shell starts to grow from the outer surface towards the core by consuming the original Si lattice. The neighboring NCs are now separated by the oxide shells, which become thicker with time in the time scale we investigated. According to equation 5.11 the critical electron concentration of MIT exponentially increases, the system moves away from the MIT, leading to the reduction of ξ. Oxidation allows us to probe the dependence of the localization length on the separation δ between NCs.

Oxidation of intrinsic H-terminated Si NCs made from the same nonthermal plasma method has been studied in our previous work, and it was found to follow the Cabrera-Mott mechanism with a characteristic time $t_m = 14.4$ min[136]. Based on this oxidation mechanism, we can investigate the dependence of localization length on the separation between NCs.

The 10% P-doped Si NC film was exposed to the air for different periods of time. Temperature dependence of the ohmic conductance for films exposed to air from 1 min to 4 hrs is plotted against $T^{-1/2}$ in Figure 5.6a. The film conductance decreases with lowering temperature for all measurements, and ES-VRH has been observed for the majority of temperature range. T_{ES} is getting larger with increasing air exposure time, which indicates the decrease of the localization length with oxidation.

This effect can be understood as follows[29]. In ES-VRH, when an electron tunnels to a distant, non-neighboring NC at a distance x, its tunneling trajectory involves passing through a chain of intermediate NCs, and the decay of the electron tunneling amplitude is dominated by passage through the gaps between neighboring NCs along the chain. As a consequence, the tunneling amplitude is suppressed by a factor of $\sim \exp[-2\delta x/ad]$[117], so that the localization length is given by $\xi \simeq ad/\delta$, where δ is the separation between neighboring NCs. The oxide growth on the Si NC surface increases δ and reduces ξ.

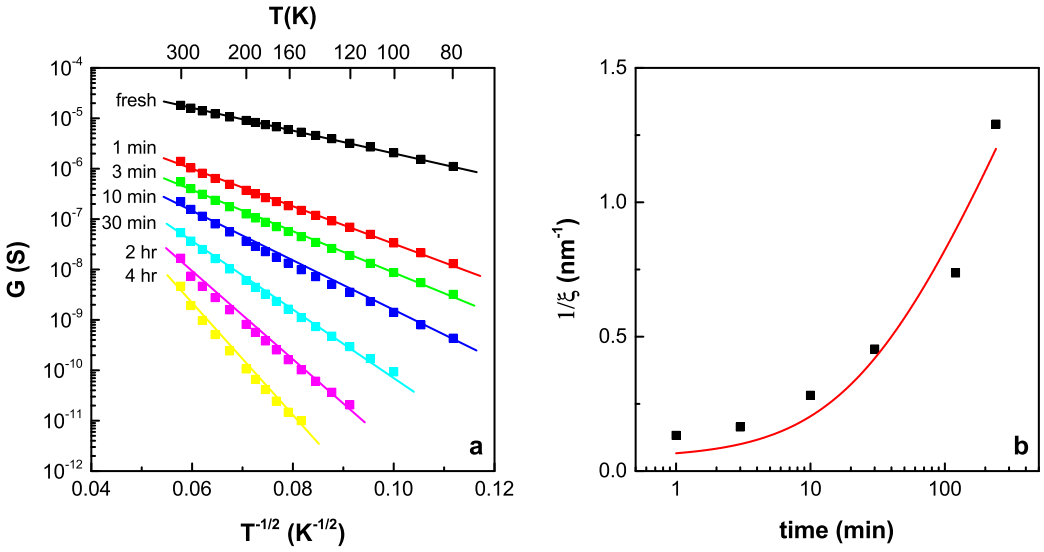

Figure 5.6: (a) Temperature dependence of the ohmic conductance for films exposed to air from 1 min to 4 hrs. The solid lines are linear fits for each curve. (b) Localization length ξ of Si NC films vs oxidation time. Error bar for ξ comes from the uncertainty caused by the linear fit and it is smaller than the symbol size. The solid red line is fit using equation 5.14.

The dynamics of the oxide growth on NC surface can be characterized by the Elovich equation[137]: $\delta = r_0 t_m \ln(1 + t/t_m)$, where r_0 and t_m are reaction rate and characteristic time, respectively. Now we have,

$$\frac{1}{\xi} = \frac{r_0 t_m}{ad} \ln\left(1 + \frac{t}{t_m}\right) \tag{5.14}$$

The inverse localization length for oxidized Si NC films is plotted against air exposure time in a linear-log scale as shown in Figure 5.6b, and the black solid line is the fit with equation 5.14. As can be seen here, the experimental data are in good agreement with Cabrera-Mott oxidation mechanism. The characteristic time t_m for P-doped Si NCs is fit to be 28 min, twice larger than the intrinsic H-terminated Si NCs[136]. In Cabrera-Mott mechanism, an electron from the cleaved Si-Si bond is transferred to an adsorbed O_2 molecule and the resulting O_2^- drifts toward the cleaved Si-Si bond with assistance of the electrostatic potential[138]. Since oxidation of Si NCs requires electron

tunneling, it is expected to observe faster oxidation in n-type doped Si NCs[80], like our system. In addition to the increase of separation between NCs, oxidation may also introduce defects which can cause reduction in the free carrier concentration and lead to the decrease in the localization length. Although the amplitude of the plasmonic peak decreases with oxidation, no clear red shift corresponding to the decrease in the free carrier concentration is observed. Therefore, we deduce that the increase of separation between NCs plays the dominant role in the decrease of localization length.

5.6 Conclusions

In summary, we have developed a theory which gives an analog of Mott criterion in films of semiconductor NCs. MIT occurs in NC films, when the concentration of electrons in a NC is $n \simeq 9 \times 10^{20}$ cm^{-3}. We investigated the electron transport in P-doped Si NCs to examine this theory, and ES-VRH conduction persists for all doping concentrations up to $n = 2.8 \times 10^{20}$ cm^{-3}.

The localization length increases with increasing doping and exceeds the diameter of a NC at $n > 1.9 \times 10^{20}$ cm^{-3}, what indicates the approach to the MIT in P-doped Si NC films. Additionally, the dependence of the localization length on the separation between NCs was studied with the assistance of controlled oxidation, and ξ decreases with increasing δ as $\xi \simeq ad/\delta$.

5.7 Experimental methods

P-doped Si NCs. Freestanding P-doped Si NCs were synthesized in a nonthermal radio-frequency plasma with a frequency of 13.56 MHz, and detailed description of synthesis can be found elsewhere[14,23]. The doping concentration is controlled by changing the flow rate of phosphine (PH_3) while maintaining constant Ar and SiH_4 flow rates. Typical flow rates used in this work are 0.4 standard cubic centimeters per minute (sccm) of SiH_4, 55 sccm of Ar, and $0.028 - 0.66$ sccm of PH_3 diluted to 15% in hydrogen. The plasma is operated at a pressure of 0.9 Torr with a nominal power of 110 W.

XRD and TEM. The crystallinity and the particle size of Si NCs were characterized

by XRD using a Bruker-AXS microdiffractometer with a 2.2 kW sealed Cu X-ray source at 40 kV and 40 mA (wavelength 0.154 nm). The XRD pattern was recorded for dry powders of Si NCs on a glass substrate. The HRTEM employed FEI Tecnai G2 F-30 TEM with a Schottky field-emission electron gun operated at 100 kV accelerating voltage. The TEM sample was prepared by collecting Si NCs directly onto a copper lacey carbon grid in the plasma reactor.

FTIR. FTIR measurements were performed using a Bruker Alpha IR spectrometer equipped with a diffuse reflectance (DRIFTS) accessory with a deuterated triglycine sulfate (DTGS) detector. All spectra were recorded from 375 to 7000 cm^{-1} at 2 cm^{-1} resolution, and averaged over 20 scans.

ICP-OES. The P incorporation in Si NCs was quantified by ICP-OES. Si NCs were digested in a mixture of hydrochloric acid (HCl), nitric acid (HNO_3) and hydrofluoric acid (HF). The elemental analysis was calibrated by the standards of Si and P samples.

Device fabrication. Lateral two-terminal devices were fabricated on SiO_2 substrates with prepatterned Au interdigitated electrodes inside a nitrogen-filled glovebox. The spacing of electrodes is 30 μm, and the aspect ratio is 5317. The substrates were pre-cleaned by sequential ultrasonication for 10 min each in acetone, methanol and isopropyl alcohol, and were treated in UV/Ozone for 20 min. As-produced Si NC powders were dissolved in anhydrous 1,2-dichlorobenzene (DCB), and cloudy stable suspensions were formed by ultrasonication. Si NC films were spin-coated from dispersions of 10 mg/ml.

Film annealing. Previous work has shown that low temperature annealing leads to an increase in the free electron concentration of the P-doped Si NCs and this is primarily attributed to the reduction of dangling bond defects during the annealing process[23]. We notice that the annealed Si NC films exhibit higher conductance and improved stability compared with fresh-made films. For this study, all P-doped Si NC films were annealed at 125 °C overnight inside the glovebox before measurement. The O_2 level was controlled less than 0.1 ppm to minimize the oxidation of NCs during annealing. The devices were then transferred into another nitrogen-filled glovebox for subsequent electrical measurements. All handling and testing of devices was performed without air exposure.

Current-voltage Measurement. The current-voltage (*I-V*) characteristics of the NC films were recorded in a Desert Cryogenics (Lakeshore) probe station in a nitrogen-filled glovebox with Keithley 236 and 237 source measuring units and homemade LabVIEW programs. Low temperature measurements employed a Lakeshore 331 temperature controller with a fixed ramp rate of 4 K/min. All electrical measurements were carried out in the dark and under vacuum at the pressure of $\sim 10^{-3}$ Torr.

Fabrication of patterned substrates. The silicon substrates with interdigitated pattern of gold are fabricated in the Nano Fabrication Center as follows:

- Deep clean the wafers (Si with 300 nm SiO_2) with piranha solutions (H_2SO_4: H_2O_2) for 15 $\sim$ 20 mins. Rinse with DI water and blow dry.
- Dehydration bake: 200 °C for 5 min.
- Spin coating LOR-3A (positive photoresist) at 3000 rpm for 45 s.
- Bake: 185 °C for 5 min.
- Spin coating S1813 (positive photoresist) at 4000 rpm for 30 s.
- Bake: 115 °C for 2 min.
- Exposure: low vacuum contact mode, air gap 35 μm, expose for 4 s.
- Develop with CR-26 developer for 30 s, rinse with DI water and blow dry.
- Bake: 125 °C for 60 s.
- Develop with CR-26 developer for 40 s (undercut), rinse with DI water and blow dry.
- Inspect under optical microscope.
- E-beam evaporate Cr/Au (30/300 Å), 1Å/s.
- Lift-off soak in Microposit remover 1165 overnight, followed by a thorough rinse with DI water and blow dry.

5.8 Future work

The critical doping concentration at the MIT in a semiconductor NC film is predicted to be 9×10^{20} cm^{-3}. It seems like not far away from the highest doping concentration 3×10^{20} cm^{-3} achieved in P-doped Si NCs. At such a high doping concentration, fractional flow rate for PH_3 is $X_{P,nom} = 20\%$ of the total flow rate for PH_3 and SiH_4. Also, it is noted that the P incorporation efficiency $\eta_P = X_{P,ICP}/X_{P,nom} \times 100\%$ is about 50% when $X_{P,nom}$ is below 5%, but decreases to 35% at $X_{P,nom} = 20\%$. Table 5.3 summarizes the some key parameters of P doping in Si NCs.

Table 5.3: Key parameters of P doping in Si NCs. N_{tot} is the total number of atoms in a Si NC, N_P is the number of P atoms and $N_{P,active}$ is the number of active P donors in a Si NC.

$X_{P,nom}\%$	$X_{P,ICP}\%$	$\eta_P, \%$	d, nm	N_{tot}	N_P	$N_{P,active}$	$N_{P,active}/N_P, \%$
1	0.46	46	8.1	14076	65	-	-
2	0.82	41	8	13396	110	-	-
3	1.56	52	8	13396	210	-	-
5	2.38	48	8	13396	320	51	16
10	4.06	41	7.5	10891	442	53	12
20	6.98	35	7.1	9233	644	52	8

As shown in Table 5.3, not only the P incorporation efficiency η decreases with increasing nominal doping, but also the ratio of active donors to all incorporated P atoms decreases with nominal doping. This is resulted from the synthesis process. Most P atoms are condensed on the NC surface, only a few of them can be incorporated into the core of a NC. The surface of NC is a mixed phase of Si and P, terminated with H atoms, or one can call it a P-contained amorphous Si shell. As nominal doping concentration goes up, it is expected to have more P atoms in this shell. Further high resolution TEM spectroscopy is needed to get more information about this shell, such as thickness and P concentration. In the theoretical model, the role of this shell in the electrical transport is not considered due to the lack of information about the shell. If this shell acts as an insulating barrier, the critical doping concentration for the MIT in Si NCs should be even larger (see equation 5.11). Further increase in the nominal

doping concentration may lead to a thicker shell, which will push the critical doping concentration to a even higher value. Also, there is a limit for doping. At sufficiently high $X_{P,nom}$, alloy or separate phase of P may appear.

On the other hand, one can manipulate the decay length a to achieve the MIT in NC films. The decay length primarily depends on the barrier height out of the NCs. In our calculation, 4 eV barrier from the work function of Si is assumed, and this is consistent with the experimental results[25]. By changing the surrounding medium of NCs in the film, one can reduce the barrier height, and thus increase the decay length. Atomic layer deposition could be one option. Inorganic material can be infilled into a NC film (density ~ 50 %) and coated onto internal surface to form a NC composite. Special consideration is required when choosing the inorganic material. The best material should have lower conduction band than Si, so that electrons can transport freely between two neighboring NCs. However, only a few oxides or sulfides can be deposited from atomic layer deposition method. Among the available materials, zinc sulfide (ZnS) will be the first choice. The conduction band offset between Si and ZnS is less than 1 eV. In this case, the decay length will be twice larger. ZnS coating on each NC surface may also passivate some surface defects, facilitating the electrical transport. The precursors for ZnS are typically oxygen free, therefore, oxidation of Si NCs will not be an issue.

In the theoretical model, we only consider an array of spherical NCs in point contact with each other. The transport is limited by the small area of "contact discs" resulted from this geometry. For faceted NCs, the contact area will be much larger, it is expected that the MIT will occur at a lower critical doping concentration.

Chapter 6

The Importance of Dopants Location

6.1 Introduction

The NC surface largely depends on the synthesis process. The introduction of B atoms into the Si NCs for doping results in a Lewis acidic boron surface which provides a more versatile surface for solution-based processing techniques. In this chapter, we will show that the location of dopants plays an important role in the electrical properties of the NC films. Similar to P doping, a precursor gas for dopants, diborane (B_2H_6), is introduced into the plasma and the majority of incorporated B atoms condense on the NC surface. According to our previous X-ray photoelectron spectroscopy (XPS) study, more than 60% B atoms are found to be trivalent and located near the NC surface. These B atoms can act as Lewis acid to interact with Lewis basic solvents[139] (e.g., dimethyl sulfoxide), resulting in the colloidal stability of B-doped Si NCs.

In this chapter, electrical measurements have been performed on the B-doped Si NC films to better understand the relationship between electrical properties and the surface of NCs. The bonding status of trivalent surface B atoms is found to be correlated with the film conductance. The carrier transport in B-doped Si NCs follows ES-VRH mechanism and the localization length shows weak dependence on the nominal doping. Moreover, B-doped Si NCs exhibit resistance to oxidation compared with P-doped Si NCs. Therefore, a modified atomic layer deposition (ALD) method is developed to

infill Si NC films, and excellent air stability is achieved with a thin layer of alumina deposition.

6.2 Characterization of B-doped Si NCs

B_2H_6 diluted in hydrogen with volume fraction 10% was used as the precursor gas for B dopants, and the nominal doping concentration is represented by the fractional flow rate of B_2H_6: $X_{B,nom} = 2[B_2H_6]/(2[B_2H_6]+[SiH_4])\times 100\%$, where $[B_2H_6]$ and $[SiH_4]$ are the flow rates of diborane and silane. Table 6.1 summarizes the plasma synthesis conditions for B-doped Si NCs at nominal doping concentration $X_{B,nom} = 4 \sim 30\%$ used in this study.

Table 6.1: Plasma synthesis conditions for B-doped Si NCs

	units	**value**	**comments**
Ar	sccm	55	100%
SiH_4	sccm	0.4	100%
B_2H_6	sccm	0.08-0.86	10% in H_2
pressure	mTorr	900	actual
power	W	110	nominal
tube	inch	1	O. D., Pyrex
orifice	mm×mm	12×0.61	slit area

Figure 6.1 shows the structural characterization for B-doped Si NCs. The cubic diamond structure (see Figure 6.1a) is observed in Si NCs at all doping concentrations from 4% to 30%, and the particle sizes are estimated from the XRD peak broadening with spherical correction[93]. The diameter of Si NCs is ~ 7 nm, with a standard deviation about $15\% \sim 18\%$ of the average size. Figure 6.1b shows a typical high resolution TEM image for nominally 10% B-doped Si NCs, and particles maintain the spherical shape at all doping concentrations. The B incorporation is quantified by ICP-OES. Some key parameters for B doping in Si NCs are given in Table 6.2.

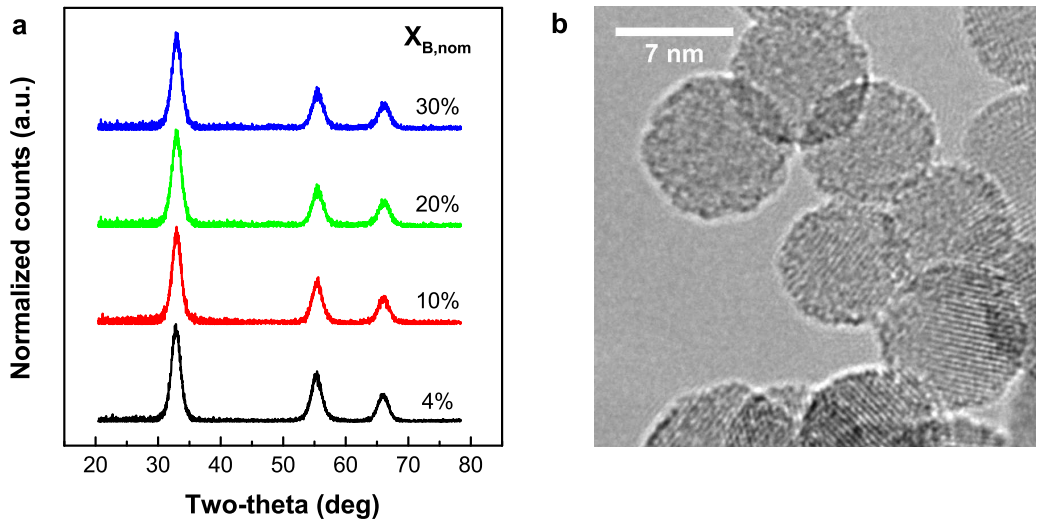

Figure 6.1: Structural characterization for B-doped Si NCs. (a) XRD spectra for B-doped Si NCs at nominal doping concentration $X_{B,nom} = 4, 10, 20$ and 30%, respectively. (b) High resolution TEM image for nominally 10% B-doped Si NCs. Particles have spherical shape and doping does not alter the particle shape.

$X_{B,nom}$%	$X_{B,ICP}$%	η_B, %	d, nm	N_{tot}	N_B	$N_{B,active}$	$N_{B,active}/N_B$, %
4	0.32	8	6.7	7869	26	66	-
10	1.03	10	6.7	7869	81	132	-
20	3.50	18	6.7	7869	276	132	48
30	6.35	21	6.7	7869	499	153	31

Table 6.2: Key parameters of B doping in Si NCs. $X_{B,nom}$ is the nominal doping, $X_{B,ICP}$ is the atomic fraction of B in Si NCs measured from ICP-OES, η_B is the B incorporation efficiency, defined as $\eta_B = X_{B,ICP}/X_{B,nom} \times 100\%$, d is the average diameter of NCs. N_{tot} is the total number of atoms in a Si NC, N_B is the number of B atoms calculated from $X_{B,ICP}$, and $N_{B,active}$ is the number of active B acceptors in a Si NC, estimated from plasmonic peaks of the corresponding Si NCs (see Figure 6.4c).

As the nominal doping concentration $X_{B,nom}$ increases, $X_{B,ICP}$ goes up and the number of incorporated B atoms N_B increases. However, the number of active B atoms $N_{B,active}$ does not change for $X_{B,nom} > 10\%$, which indicates a saturation of B doping

in Si NCs. It is noted that $N_{B,active} > N_B$ for $X_{B,nom} < 10\%$. This is probably caused by the poor resolution of ICP-OES measurement at extremely low concentration.

6.3 Role of surface B atoms

Significant improvement of conductance after low temperature annealing has been observed in P-doped Si NC films as studied in the last chapter. However, B-doped Si NC films exhibited a complicated behavior upon annealing. In Figure 6.2a, we show the annealing study for nominally 10% B-doped Si NC films cast from dimethyl sulfoxide (DMSO). The film conductance decreases more than 10 times after the initial annealing at 200 °C for 10 min, and it keeps decreasing with longer annealing time. After 30 min annealing, the minimum film conductance has been reached. Further annealing at the same temperature overnight increases the film conductance and it returns to the original value after another annealing step at 300 °C for 5 hrs. A similar trend is observed in the annealing study for films cast from n-methyl-2-pyrrolidone (NMP) as displayed in Figure 6.2b. Both of DMSO and NMP can provide colloidal stability for B-doped Si NCs, but the solubility of NCs is much higher in DMSO than NMP.

As we have shown in the previous study for B-doped Si NCs, the colloidal stability arises from the occupation of the vacant valence orbital of trivalent surface B atoms[139]. These trivalent surface B atoms act as electron-acceptors while O atoms in DMSO or NMP are electron-donors. Therefore, Lewis acid-base interaction between solvent and trivalent surface B atoms occurs. This may result in surface transfer doping[64] as discussed in Chapter 2. The NC device films were cast from DMSO or NMP solution, one may deduce that the evaporation of solvent at the initial stage of annealing process terminates the Lewis acid-base interaction and there is no doping effect. Further annealing induces oxidation of the NCs to form B-O bonds, which may again enable doping. Once the particles are oxidized, they cannot dissolve in solvents anymore, which suggests the absence of trivalent surface B atoms. The bonding status of the trivalent surface B atoms can tune the conductance of the NC films. This hypothesis is supported by the IR spectra of the nominally 10% B-doped Si NCs as shown in Figure 6.2c.

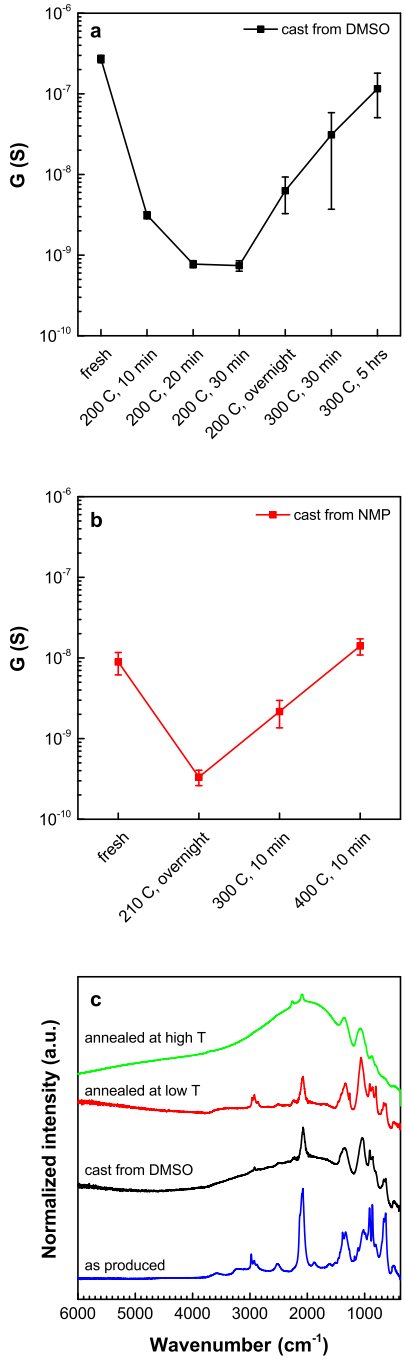

Figure 6.2: Electrical conductance and FTIR spectra for nominally 10% B-doped Si NCs. (a) Ohmic conductance for film cast from DMSO at different annealing conditions. (b) Ohmic conductance for film cast from NMP at different annealing conditions. (c) FTIR spectra for Si NC film as produced, cast from DMSO, annealed at around 150 °C for 1 hr and annealed at 200 °C for a few hours.

There is no plasmonic feature in the as-produced B-doped Si NCs. After these particles were dissolved in DMSO and a film was cast from the solution, a clear broad feature associated with a plasmonic peak can be seen. When this film was annealed at relatively low temperature (around 150 °C), the plasmonic peak slowly disappears. Further annealing at relatively high temperature (above 200 °C) brings back the plasmonic peak. The observation of appearance/disappearance of the plasmonic peak is an indication of increase/decrease of the free carrier concentration in the NC film, consistent with the presence/absence of interaction between trivalent surface B atoms and surface molecules (e.g. solvent or oxygen).

It seems like that all these experimental observations confirm the proposed picture of surface transfer doping. However, the carrier type indicated by the surface transfer doping contradicts the thermopower results. According to the Lewis acid-base interaction, trivalent surface B atoms draw electron density of O atoms in DMSO towards themselves, leading to n-type doping. The thermopower measurement performed on the same as-produced B-doped Si NC films cast from DMSO shows p-type conduction as indicated by the positive slope in Figure 6.3.

As will be discussed in the oxidation study, B-doped Si NCs exhibit much better air stability than P-doped Si NCs, which is consistent with behavior of p-type Si NCs. Here, we propose another hypothesis for the role of trivalent surface B atoms. It is clear that the trivalent surface B atoms are sitting on the NC surface, and the Si NC can be considered as a core-shell structure with a crystalline Si core and B-doped amorphous Si shell terminated by H. In amorphous hydrogenated Si (a-Si:H), trivalent B atoms can produce deep gap states which are electrically passive[140]. Assume that these trivalent B atoms act as hole traps, B-doped Si NCs are doped by four-fold coordinated B, which results in p-type doping. The as-produced B-doped Si NCs have a large number of trivalent B atoms, therefore, the free carrier concentration is fairly low and no plasmonic peak can be seen. In the B-doped Si NC films cast from DMSO, the trivalent surface B atoms are passivated by the DMSO molecules and the free carrier concentration in the NC film is high enough to support the plasmonic feature. As will be shown in this chapter, the plasmonic feature and the high conductance of B-doped Si NC films are dependent on the surface treatment which may change the bonding status of the trivalent B atoms, and the carriers are always p-type. At this point, it is not clear if

the free carriers are generated by the same mechanism for films cast from DMSO and oxidized films.

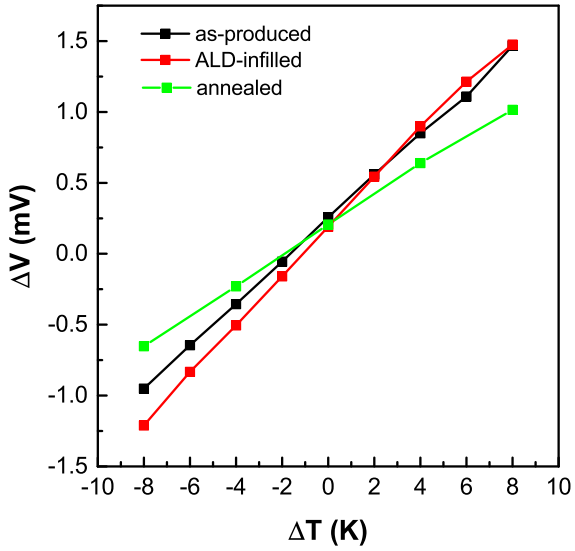

Figure 6.3: The induced thermoelectric voltage $\Delta V = V_2 - V_1$ vs the applied temperature gradient $\Delta T = T_1 - T_2$ for nominally 20% B-doped Si NC films cast from DMSO solution. The measurement has been performed on the as-produced, annealed and ALD-infilled Si NC films. The positive slope indicates p-type conduction.

The annealing study was conducted on a hot plate inside a nitrogen-filled glovebox, the oxidation of Si NCs during annealing process is limited by the available surrounding oxygen molecules. We speculate that there are two competing effects caused by oxidation. One is the passivation of trivalent surface B atoms, which increases the free carrier (holes) concentration in NC film as we discussed above. Again, thermopower measurement on annealed Si NC film shows p-type conduction (see Figure 6.3). The other one is oxide formation which may introduce interfacial defects to trap some free carriers or build thicker tunneling barriers. If the Si NC film is exposed to air for a few hours, the film conductance will still decrease.

It is noted that the fresh film cast from NMP shows lower conductance than film cast from DMSO, and the plasmonic peak is absent in film cast from NMP which indicates much less free carriers. This could be attributed to weaker interaction between trivalent

surface B atoms and NMP, thus less B atoms are passivated, or the energy levels of NMP and Si NCs are not well aligned for achieving doping effects. For the following measurements, all films are cast from DMSO.

6.4 Doping dependence of electrical transport

Due to the complicated annealing effects, the temperature experiments were performed for films before and after annealing. Films made from NCs at different nominal B doping concentrations were treated under the same annealing condition. As shown above, B-O bonds can form on the NC surface through oxidation even inside the glovebox. To keep consistency, all the samples here were annealed in the probe station chamber at 107 °C under vacuum $\sim 10^{-3}$ Torr for 1 hr and cooled down to room temperature for the next electrical measurements. Four different nominal doping concentrations were investigated for doping dependence study, 4%, 10%, 20% and 30%. The B-doped Si NCs can be directly dissolved in specific solvents due to the interaction between trivalent surface B atoms and solvent molecules, the solubility of NCs in solvent depends on the strength of this interaction. For DMSO solvent, minimum nominal doping 4% is needed to achieve good colloidal stability to produce high quality films. Only ohmic conductance is measured in this work.

The temperature data for Si NCs at all doping concentrations before and after annealing can be plotted as a function of $T^{-1/2}$, consistent with the ES-VRH conduction. For P-doped Si NC films, the film conductance increases monotonically with nominal doping concentration. As $X_{P,nom}$ increases, the film becomes more conductive and the localization length gets larger. However, there is no such trend for B-doped Si NC films, the difference between the lowest and highest conductance is within one order of magnitude. For the fresh-made samples, the film with 30% nominal doping shows the lowest conductance and the film with 10% nominal doping shows the highest conductance as displayed in Figure 6.4a. After annealing, the conductance for all films decreases by $5 \sim 20$ times due to the removal of bonded DMSO molecules as we discussed above. The film with 4% nominal doping has the lowest conductance while the film with 20% nominal doping gives the highest conductance (see Figure 6.4b).

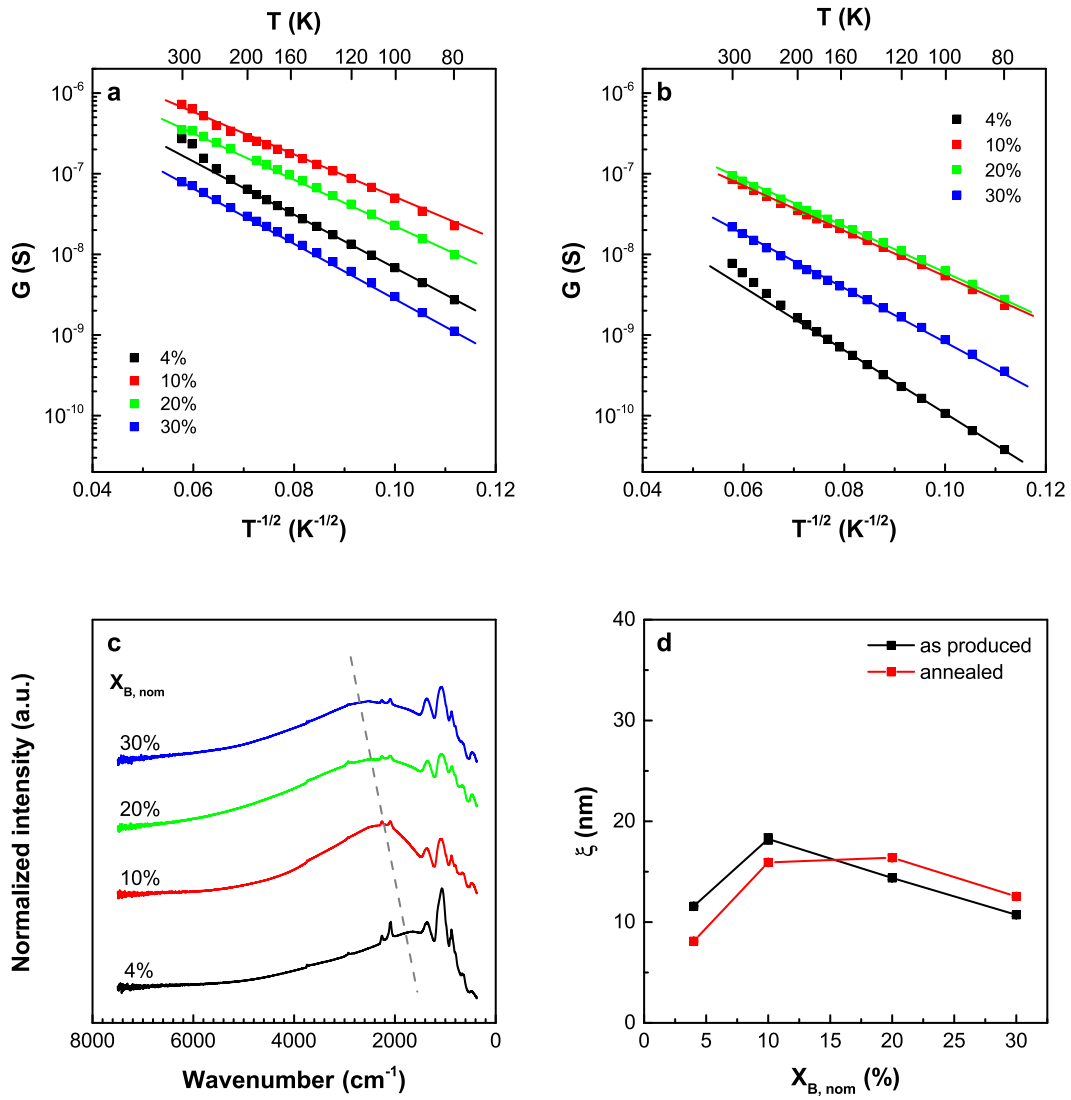

Figure 6.4: Doping dependence of electrical transport in Si NCs. (a-b)Temperature dependence of the ohmic conductance for as-produced films (a) and annealed films (b) cast from B-doped Si NCs with nominal doping concentration 4%, 10%, 20% and 30%. (c) Normalized FTIR spectra for as-produced Si NCs with different nominal doping concentrations. A dash line is added as a guide for the eye. The free carrier concentration is estimated from this plasmonic peak position using equation 5.13. (d) Localization length ξ as a function of nominal doping $X_{B,nom}$ for as-produced and annealed films. Error bar for each data point is smaller than symbol size.

Figure 6.4c shows the FTIR spectra for Si NC films cast from DMSO with different nominal doping concentrations. As B nominal doping concentration increases from 4% to 10%, a blue shift in the plasmonic peak is observed. However, the plasmon stays almost at the same position as more B_2H_6 is added into the plasma (sample with $X_{B,nom} = 30\%$ has a little bit more blue shift). The average free carrier concentration n_{fc} in each sample can be estimated from equation[23] 5.13. For 4% B-doped Si NCs, the free carrier concentration $n_{fc} = 4.2 \times 10^{20}$ cm^{-3} and this corresponds to 66 free carriers per NC; for 10% and 20% , we have $n_{fc} = 8.4 \times 10^{20}$ cm^{-3}, equivalent to 132 free carriers per NC; for 30%, we have $n_{fc} = 9.7 \times 10^{20}$ cm^{-3}, equal to 153 free carriers per NC.

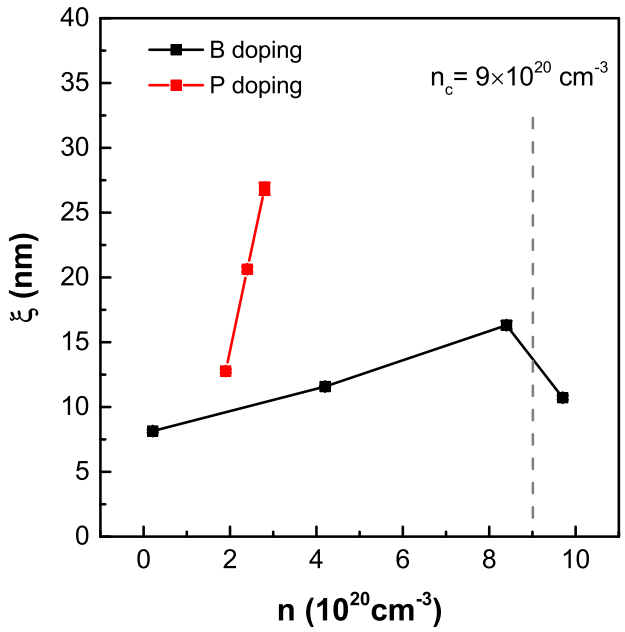

Figure 6.5: Comparison of localization length ξ vs doping concentration n in P- and B-doped Si NCs. The error bar for each data point is smaller than the symbol size. The dash line indicates the theoretical critical doping concentration for the MIT found in P-doped Si NCs.

The localization length ξ is extracted from the T_{ES} for each doping concentration using equation 2.16. The effective dielectric constant ε_r is calculated to be ~ 2.46 with equation 2.8 (the film density $\sim 42\%$ measured from ellipsometry). A weak dependence

on the nominal doping concentration is shown in Figure 6.4d, and the annealing does not really change ξ. To better understand the relationship between the localization length and the doping concentration, ξ is plotted against the real doping concentration n estimated from LSPR for both of P and B cases (see Figure 6.5). In B-doped Si NCs, the lowest doping concentration determined from plasmonic peak in FTIR spectra (see Figure 6.4c) is $n_{fc} = 4.2 \times 10^{20}$ cm^{-3}, but the annealed sample has at least 20 times lower free carrier concentration due to the absence of the plasmonic peak. Therefore, we include the estimated doping concentration in the annealed nominally 4% B-doped Si NCs, which is 2.1×10^{19} cm^{-3}. Based on the theory developed in Chapter 5, the critical doping concentration for the MIT in Si NCs is predicted to be $n_c = 9 \times 10^{20}$ cm^{-3}. It is shown as a dash line in Figure 6.5 for reference. As can be seen here, the highest doping concentration in B case is actually close to n_c, however, the localization length does not show a sign of divergence. Instead, it tends to be relatively constant in the range of investigated doping concentrations. This is completely different from P-doped Si NC films, in which the localization length ξ steeply increases with increasing doping concentration. The reason behind is not clear at this point, we propose that the carrier type can change the transport picture. In Si, there are six equivalent minima ($g = 6$) of the conduction band, but only one maximum ($g = 1$) of the valence band. As shown in Chapter 5, at the MIT, the mean free path l of carriers inside a Si NC depends on the carrier concentration and the degeneracy g. The mean free path of electrons is smaller than the diameter of Si NC, therefore, electrons move diffusively inside the NC and are scattered by the ionized donors. For holes, the mean free path can be comparable to the diameter of the NC, therefore, they can move ballistically inside the NC, and this will significantly change the picture of transport. In addition, the doping mechanism is not clear in the B-doped Si NCs, which may also dramatically change the carrier transport.

6.5 Oxidation of B-doped Si NCs

The oxidation of B-doped Si NCs is studied as shown in Figure 6.6. Again, nominally 10% B-doped Si NCs were used for this experiment. The Si NC film was annealed inside probe station vacuum chamber at 107 °C for 1 hr to remove the surface-bonded DMSO molecules, and cooled down to the room temperature for the following temperature

experiment. This film was referred to as-made NC film. After acquiring temperature data for the as-made NC film, the same film was exposed to air for oxidation and temperature experiments were repeated for the same film oxidized for 1 hr, 2 hrs and 4 hrs. In general, the data can still be plotted against $T^{-1/2}$ as displayed in Figure 6.6a, in agreement with ES-VRH conduction. In the high temperature regime (above 200 K), the curve deviates from $T^{-1/2}$ dependence, probably because of a transition to activated behavior. As the air exposure time increases, the film conductance decreases. The slope fit from data below 200 K is plotted in Figure 6.6b as a function of air exposure time t. As-made film was given $t = 0.1$ min for display. We have shown that the oxidation of P-doped Si NCs can be well described by Cabrera-Mott oxidation model, and the increase of $1/\xi$ is caused by the oxide growth (see equation 5.14).

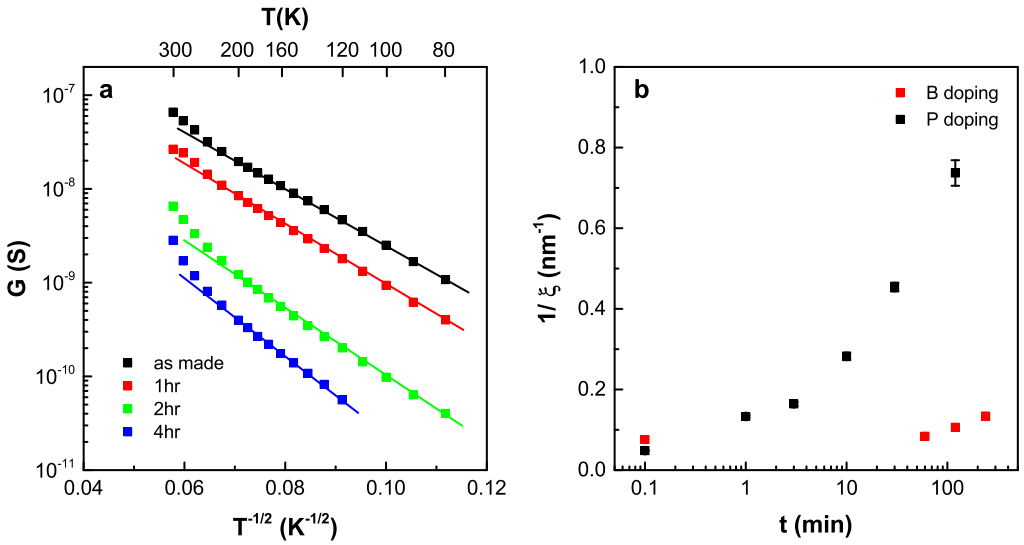

Figure 6.6: Oxidation of nominally 10% B-doped Si NCs. (a) Temperature dependence of the ohmic conductance for oxidized films. (b) Inverse localization length $1/\xi$ plotted as a function of air exposure time t for nominally 10% P-doped Si NC films and nominally 10% B-doped Si NC films. The error bar comes from the uncertainty of the slope T_{ES} caused by the linear fit. For B-doped Si NC films, the error bar is smaller than the symbol size.

Different from the dramatic effects of oxidation on the electrical properties of P-doped Si NC films, B-doped Si NC films exhibit resistance to oxidation. In P-doped Si NC films, the film conductance decreases by more than 4 orders of magnitude after 4 hrs of oxidation, and the localization length is reduced by about 30 times. In B-doped Si NC films, after oxidation for 4 hrs, the film conductance at room temperature decreases by about 10 times while the localization length is twice smaller. Compared with P-doped Si NCs, the oxide growth is much slower in B-doped Si NCs. Since Cabrera-Mott oxidation is assisted by electrons, one can see that the presence of P donors will accelerate the oxidation of Si NCs while the presence of B acceptors will suppress the oxidation process[80], which is consistent with our experimental observation.

6.6 Surface engineering through atomic layer deposition

We have shown that the film conductance depends on the bonding status of the trivalent surface B atoms, they can be passivated with the attachment of specific solvent molecules or surface oxidation. Now we are seeking for a more robust and well-controlled approach to passivate trivalent surface B atoms and maintain high conductivity at the same time. The enhanced resistance to oxidation in B-doped Si NCs provides more flexibility in the processing compared with P-doped Si NCs. A modified atomic layer deposition (ALD) infilling method is developed to coat alumina onto NC surface and form B-O bonds by alumina deposition. The B-doped Si NC film is cast from DMSO solution and the film thickness is $40 \sim 50$ nm with density around 40% as measured by ellipsometry. To infill alumina onto the internal surface of the NC film, the pulse time and purge time of the conventional ALD deposition are elongated. A typical process used in this work adopts 0.1 s pulses for water and trimethylaluminum (TMA) and 30 s nitrogen purges between pulses. The first pulse is water vapor. The ALD infilling process is operated at 200 °C and the film has been baked in the ALD chamber for half an hour before deposition in order to remove any surface-bonded DMSO molecules. Therefore, replacement with B-O bonds from alumina deposition will provide more robust passivation of surface B atoms.

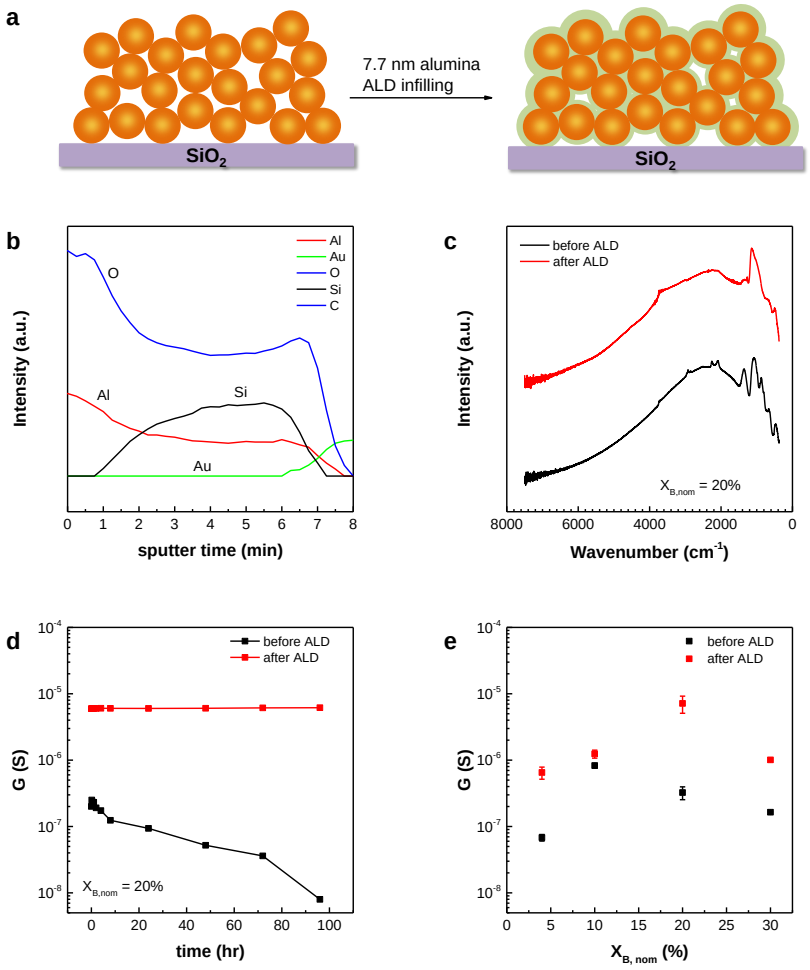

Figure 6.7: ALD infilling for B-doped Si NC films. (a) As-produced Si NC film was infilled with 7.7 nm alumina, the film density was increased by partially filling the pores between NCs and the deposition also occurred on the surface of NC film. (b) Auger elemental depth profile of a nominally 20% B-doped Si NC film infilled with ALD alumina at 200 °C. Intensities for Al and O are constant through the NC film. The sputtering rate used for this analysis is about 7 nm/min. (c) FTIR spectra for nominally 20% B-doped Si NCs before and after ALD infilling. (d) Air stability of film conductance for nominally 20% B-doped Si NC film as-produced and after ALD infilling. (e) Comparison of film conductance before and after ALD for nominal doping concentrations from 4% to 30%.

Thermopower measurements on the ALD-infilled B-doped Si NC films confirm p-type conduction, consistent with our previous hypothesis for the role of trivalent surface B atoms (see Figure 6.3).

Figure 6.7a illustrates the ALD infilling process. After 7.7 nm (70 cycles) alumina infilling, the NC composite exhibits $\sim 20\%$ increase in film density and a layer of about 8 nm alumina is overcoated on top of NC film. This is in agreement with ALD deposition mechanism, reaction occurs on the internal and external surfaces. If one imagines that this 20% alumina deposition is evenly distributed on each NC, it is equivalent to about 0.5 nm alumina coating. Assume that NCs are in direct contact of each other since the film is cast from DMSO solution without adding any organic ligands. Even if there are some residual DMSO molecules bonded to surface B atoms, they are too short to separate NCs far from each other. Moreover, the film has been baked for half an hour at 200 °C under nitrogen flow, we probably have pure inorganic NC solids when the deposition starts. Considering sealed-off space due to contact of NCs, the ALD deposition is likely to form a conformal layer around NCs and only partial filling can be achieved. On the other hand, ALD deposition can only occur on a limited number of surface sites. Indeed, longer pulse time does not show any improvement in the density of final NC composite, implying the saturation of ALD infilling. The alumina penetration is probed by Auger elemental depth profile as shown in Figure 6.7b. Constant intensities of aluminum and oxygen throughout the NC film indicate that alumina fills the pores between NCs to the gold surface of the substrate. Also, there is an extra layer of alumina on top of Si NC film. To understand how the ALD deposition modifies the NC surface, FTIR spectra for the same NC film are acquired before and after ALD process as displayed in Figure 6.7c. A clear plasmonic peak around 2350 cm^{-1} is present in the as-made film, the NC surface is terminated by SiH_x ($2000 - 2150$ cm^{-1}) and B-O bonds (~ 1350 cm^{-1}). After deposition of 7.7 nm alumina, all the surface SiH_x disappears but the plasmonic peak stays almost at the same position. As we have shown in equation 5.13, the plasmonic peak position is determined by the free carrier concentration n_{fc} and dielectric constant of surrounding medium ε_m. The infilling with alumina will slightly increase ε_m since the dielectric constant for amorphous ALD alumina is around 3, larger than nitrogen ($\varepsilon_m = 1$). Therefore, n_{fc} is actually increased after ALD, suggesting better activation of surface B atoms. The disappearance of SiH_x is likely

due to oxidation of Si NCs because ALD infilling was performed at 200 °C with water vapor as O precursor. We hypothesize that the passivation of trivalent surface B atoms is achieved by forming B-O bonds in ALD process, but it is hard to compare the height of B-O peak before and after ALD due to the presence of broad plasmonic peak. Also, no reference peak can be used in the spectra.

Film conductance was measured at room temperature before and after ALD infilling and air stability was also investigated. Figure 6.7d shows more than 10 times increase in conductance after ALD infilling for nominally 20% B-doped Si NC film. Moreover, the ALD-infilled NC film exhibits excellent stability for more than three months in the ambient environment while the as-produced NC film shows significant degradation with exposure to air for a couple of days. We speculate that the air stability is related to the absence of SiH_x since they participate in the oxidation of Si NCs[136]. Moreover, the outer alumina coating can also provide an oxidation barrier. It seems like so far oxidation is critical to improve film conductance and air stability, an ALD process with only water pulses has been performed to check if alumina deposition is needed. The conductance of the resulting film is too low for measurement, suggesting that alumina deposition is necessary for improving film conductance and air stability through the limited oxidation.

ALD infilling under the same condition was performed for Si NC films at nominal doping concentration from 4% to 30%, and a comparison of film conductance before and after ALD is shown in Figure 6.7e. The conductance for as-produced NC film increases first and then decreases as more B is added. Similar trend is observed in ALD-infilled film but the maximum conductance occurs at nominal 20% instead of 10% for as-produced films. Increase of $2 \sim 10$ times in conductance is observed after ALD infilling, 10% B-doped Si NC film shows the least improvement and 20% B-doped Si NC film has the strongest enhancement. All these films are air stable after ALD infilling.

To understand how this ALD process changes the carrier transport in NC film, low temperature experiment was conducted for samples infilled with ALD alumina. Again, four different doping concentrations are examined here, and the same ALD procedure with 7.7 nm deposition was adopted for these NC films. Due to the air stability obtained from ALD infilling, the low temperature experiment was conducted in a different instrument which allows a wider temperature range of 300 - 25 K.

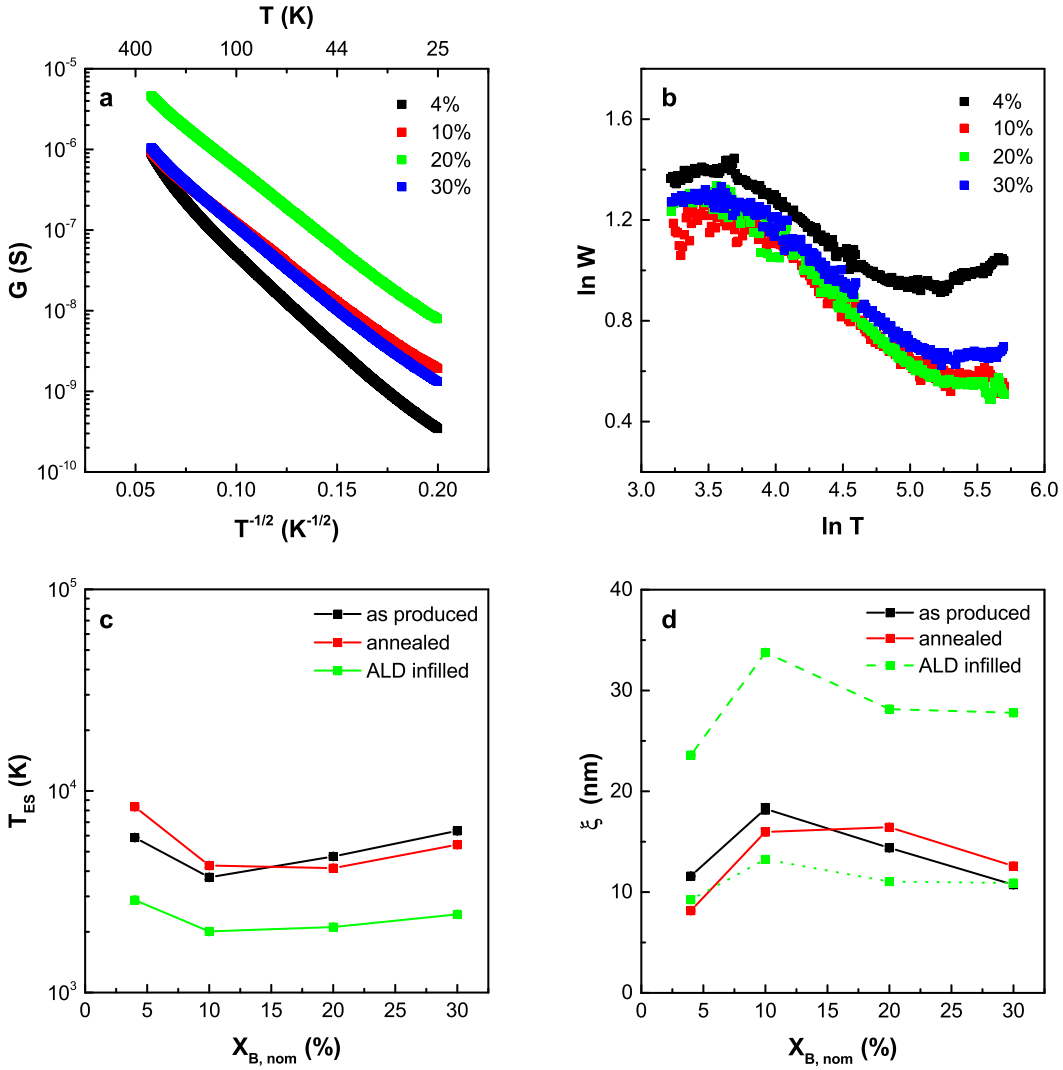

Figure 6.8: Temperature data for ALD-infilled Si NCs with different nominal doping concentrations. (a) Ohmic conductance vs temperature from 300 - 25 K. (b) Zabrodskii analysis for Si NCs films and slope of 0.5 is found for all samples. (c) Characteristic temperature T_{ES} vs nominal doping concentration. (d) Localization length ξ vs nominal doping concentration for as-produced, annealed and ALD-infilled NC films. The green dash line gives the highest estimate of localization length for ALD-infilled NC films with $\varepsilon_r = 2.46$ same as the as-produced films, and the green dot line shows the lowest estimate of ξ for ALD-infilled NC films by assuming $\varepsilon_r = 6$. The localization length of ALD-infilled Si NCs should lie in between these two green lines.

Figure 6.8a shows the ohmic conductance versus $T^{-1/2}$, and Zabrodskii analysis is shown in Figure 6.8b. The slopes for all doping concentrations determined from Figure 6.8b are very close to 0.5 for the majority of the temperature range. Therefore, the carrier transport in the ALD-infilled films still follows ES-VRH mechanism. The characteristic temperature T_{ES} is extracted from the slope of each curve in Figure 6.8a. In general, T_{ES} for ALD-infilled film is smaller than as-produced and annealed NC film at the same doping concentration (see Figure 6.8c). There is no strong dependence on the nominal doping concentration as observed in as-produced, annealed or ALD-infilled NC films. Moreover, T_{ES} is dependent on the effective dielectric constant ε_r for NC films and the localization length ξ as indicated by equation 2.16. As mentioned above, the infilling with alumina slightly increase the effective dielectric constant of NC films. Assume 100% density for final NC composite after ALD infilling, $\varepsilon_r \sim 6$[44]. As shown in Figure 6.8d, the highest and lowest estimates for localization length are given by green dash and dot lines. The true localization length is expected to lie in between these two lines for each doping concentration.

6.7 Conclusions

In summary, the relationship between the electrical transport and the surface engineering of B-doped Si NCs is explored in this chapter. The majority of B dopants are sitting on the NC surface, and the NC film conductance can be tuned by changing the bonding status of trivalent surface B atoms through the manipulation of NC surface. The electrical transport is also investigated in the B-doped Si NCs with different surface treatments. ES-VRH is observed in all B-doped Si NC films, and the localization length stays the same when the doping concentration is varied in a relatively large range of $2.1 \times 10^{19} - 9.7 \times 10^{20}$ cm^{-3}. A modified ALD infilling is applied to achieve the passivation of defect states in a robust way. Moreover, the air stability of Si NC films is significantly improved by a few nanometers of alumina coated on the NC surface.

6.8 Experimental methods

B-doped Si NCs. Colloidal stability of these B-doped Si NCs have been explored in our previous work[139]. As-produced Si NCs with doping concentration higher than a certain value can be directly dispersed in Lewis basic solvents, such as DMSO, and form clear colloids.

XRD and TEM. The crystallinity and the particle size of Si NCs were characterized by XRD using a Bruker-AXS microdiffractometer with a 2.2 kW sealed Cu X-ray source at 40 kV and 40 mA (wavelength 0.154 nm). The XRD pattern was recorded for dry powders of Si NCs on a glass substrate. HRTEM employed FEI Tecnai G2 F-30 TEM with a Schottky field-emission electron gun operated at 100 kV accelerating voltage. The sample for TEM was prepared by deposition of Si NCs directly onto a copper lacey carbon TEM grid in the plasma reactor.

FTIR. FTIR measurements were performed using a Bruker Alpha IR spectrometer equipped with a diffuse reflectance (DRIFTS) accessory with a deuterated triglycine sulfate (DTGS) detector. All spectra were recorded from 375 to 7000 cm^{-1} at 2 cm^{-1} resolution, and averaged over 20 scans.

ICP-OES. The incorporation of B in Si NCs was quantified by ICP-OES. Si NCs were digested in a mixture of hydrochloric acid (HCl), nitric acid (HNO_3) and hydrofluoric acid (HF). The elemental analysis was calibrated by the standards of Si and P samples.

Device fabrication. For electrical measurments, lateral two-terminal devices were fabricated on SiO_2 substrates with prepatterned Au interdigitated electrodes inside a nitrogen-filled glovebox. Au electrodes have thickness $\sim$ 30 nm, spacing 30 μm, and the aspect ratio is 5317. Details for patterning can be found in Chapter 5. The substrates were precleaned by sequential ultrasonication for 10 min each in acetone, methanol and isopropyl alcohol, and were treated in UV/Ozone for 30 min. Si NC films were spin-coated from dispersions of 10 mg/ml at 2000 rpm for 75 s, and three consecutive spins were performed to achieve good film coverage. The resulting film was $\sim$ 50 nm thick with density about 40% as measured from ellipsometry. Annealing study was performed on a hot plate inside a nitrogen-filled glovebox with O_2 level less than

0.1 ppm. The devices were then transferred into another nitrogen-filled glovebox for subsequent electrical measurements.

Current-voltage measurement. The current-voltage (I-V) characteristics of Si NC films were recorded in a Desert Cryogenics (Lakeshore) probe station in a nitrogen-filled glovebox with Keithley 236 and 237 source measuring units and homemade LabVIEW programs. Low temperature measurements for Si NC films without ALD infilling employed a Lakeshore 331 temperature controller with a fixed ramp rate of 4 K/min, and all electrical measurements were carried out in the dark and under vacuum at pressure of $\sim 10^{-3}$ Torr. For Si NCs with ALD infilling, the low temperature measurements were conducted in a Janis close-cycle refrigerator between measuring temperatures of 25 K and 300 K. The samples were contacted with silver paint, and current-voltage characteristics were measured using dc excitation with a Keithley 220 as a current source and Keithley 2002 as a voltage meter. Extensive checks for ohmicity, contact resistance, and self-heating were made at several measurement temperatures.

Thermopower measurement. Thermopower measurements were performed in a home-made system in Prof. Kakalios's lab. B-doped Si NC films were spin-coated onto glass substrates from NC colloids in DMSO with concentration 10 mg/ml. The glass substrates were pre-cleaned by ultrasonication for 10 min each in acetone, methanol and isopropyl alcohol, and dried by nitrogen blow. Prior to spin coating, the glass substrates were treated under UV/Ozone for 30 min. As shown in Figure 6.9, the sample is placed across two separate copper blocks and the electrodes made from silver paint are separated by 4 mm. The length of electrodes are $\sim$ 10 mm. The sample temperatures are measured with thermocouples T_1 and T_2, and the potential at each electrode is recorded by voltage meters V_1 and V_2. The applied temperature gradient $\Delta T = T_1 - T_2$ induces a thermoelectric voltage $\Delta V = V_2 - V_1$. The Seebeck coefficient, defined as $S = \Delta V/\Delta T$, is derived from the slope of the resulting linear plot of ΔV against ΔT. A positive slope indicates p-type conduction, while a negative slope indicates n-type conduction. For the measurement, T_1 and T_2 vary from 311 to 319 K.

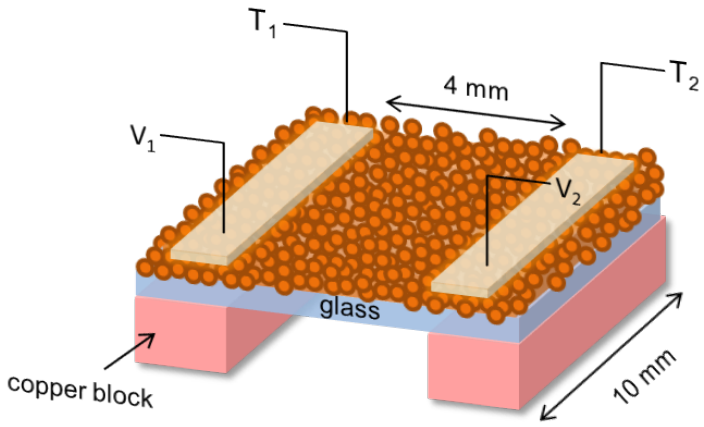

Figure 6.9: Schematic of thermopower measurement. The sample is placed across two copper blocks with embedded heaters. The temperatures of each block are independently controlled, and the sample temperatures are measured with thermocouples T_1 and T_2. The potential at each electrode is recorded by voltage meters V_1 and V_2.

6.9 Future work

The Lewis acidic boron surface has many advantages. First of all, the Si NCs can be directly dissolved into solvent which simplifies the solution processing. The ligand strategies developed for metal-based NCs can be applied to B-doped Si NCs. Second, B doping slows down the oxidation of Si NCs, which allows more flexibility of post-synthesis treatment and further device fabrication. Most importantly, the air stability problem of Si NCs can be easily solved by a thin layer ALD deposition of alumina on the NC surface. However, B doping concentration is not well controlled during synthesis since the B atoms tend to segregate onto the NC surface, leading to weak tunability of doping concentration. There exists a critical nominal doping concentration (nominal 4% for DMSO) above which the NCs can be well dissolved into the solvent. Also, above nominal 10%, the free carrier concentration does not shift with the nominal doping, suggesting a saturation of the number for trivalent surface B atoms. More work is needed to illustrate the doping mechanism in the B-doped Si NCs, it is related more to the NC surface instead of the conventional bulk substitutional doping.

The electrical transport in B-doped Si NCs still follows ES-VRH mechanism, same as the P-doped Si NCs. However, the localization length does not change with doping concentration. According the theory developed in the last chapter, there is a critical doping concentration at which the MIT occurs in the P-doped Si NC films. This result is based on the assumption that donors are located inside the NC and electrons will be scattered by the ionized donors. In the B-doped Si NCs, the carriers are holes, which have different degeneracy of valence band maxima. The carrier motion inside the NC can be completely different. The critical doping concentration derived in the P case can not be applied to the B case. Moreover, the majority of B atoms are sitting on the NC surface, carriers will move ballistically inside the NC and this will change the transport picture. Indeed, this model has been widely observed in the metal-based NCs, in which the doping is typically achieved through the surface manipulation. More theoretical work is needed to explore the MIT in these NC films. On the other hand, further high resolution spectroscopy will be helpful to probe the location of the dopants in the B-doped Si NCs and confirm the proposed model.

Another phenomenon observed in B-doped Si NCs is the light enhanced conductivity. The film conductance of B-doped Si NCs shows a dependence on the light illumination. As shown in Figure 6.10, the films stored in dark exhibit typically lower conductance than films exposed to the room light. When the films exposed to the room light were stored in dark, their conductance decreased. The shaded area represents the time period when all these samples were stored in dark. After re-exposing to the room light, the film conductance can be restored. It is a reversible process. For films infilled with ALD, there is no dependence on the light illumination for the film conductance. This effect has been observed in Si NC films with all doping concentrations.

The reason for this light effect is not clear, it is probably due to some long-lived traps for the carriers. It appears that the ALD process helps passivation of these defects. All the B-doped Si NC films studied in this chapter were exposed to the room light. Further work is needed to understand more about this light effect, and deep-level transient spectroscopy (DLTS) could be one option.

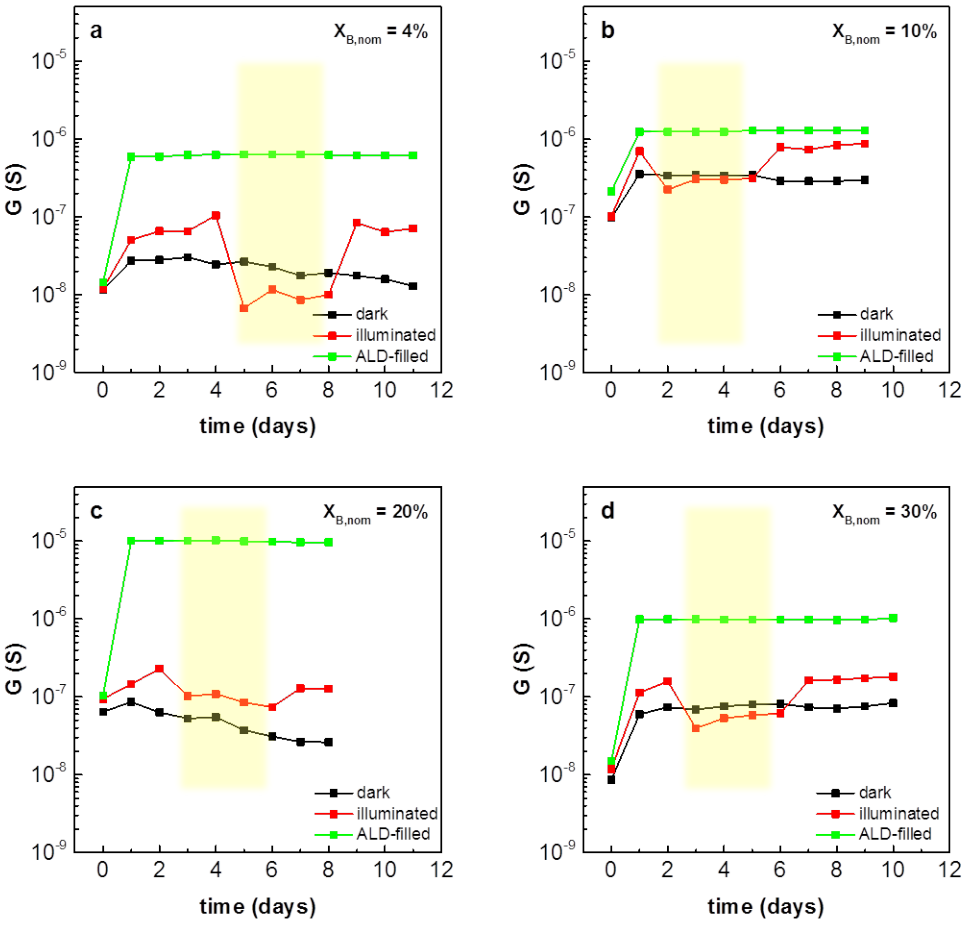

Figure 6.10: The comparison of conductance for films stored in dark, exposed to room light (photo) and infilled with ALD. The shaded area represents the time period in which all samples were stored in dark. For photo samples, they were exposed to the room light; for dark samples, they were stored inside an opaque container. Si NCs with four different doping concentrations were studied (a) $X_{B,nom} = 4\%$, (b) $X_{B,nom} = 10\%$, (c) $X_{B,nom} = 20\%$, (d) $X_{B,nom} = 30\%$.

References

[1] Dmitri V. Talapin and Christopher B. Murray. PbSe nanocrystal solids for n- and p-channel thin film field-effect transistors. *Science*, 310(5745):86–89, 2005.

[2] Jiang Tang, Kyle W. Kemp, Sjoerd Hoogland, Kwang S. Jeong, Huan Liu, Larissa Levina, Melissa Furukawa, Xihua Wang, Ratan Debnath, Dongkyu Cha, Kang Wei Chou, Armin Fischer, Aram Amassian, John B. Asbury, and Edward H. Sargent. Colloidal-quantum-dot photovoltaics using atomic-ligand passivation. *Nature Materials*, 10(10):765–771, 2011.

[3] Alexander H. Ip, Susanna M. Thon, Sjoerd Hoogland, Oleksandr Voznyy, David Zhitomirsky, Ratan Debnath, Larissa Levina, Lisa R. Rollny, Graham H. Carey, Armin Fischer, Kyle W. Kemp, Illan J. Kramer, Zhijun Ning, Andre J. Labelle, Kang Wei Chou, Aram Amassian, and Edward H. Sargent. Hybrid passivated colloidal quantum dot solids. *Nature nanotechnology*, 7(9):577–582, 2012.

[4] Robert Y. Wang, Joseph P. Feser, Jong-Soo Lee, Dmitri V. Talapin, Rachel Segalman, and Arun Majumdar. Enhanced thermopower in PbSe nanocrystal quantum dot superlattices. *Nano letters*, 8(8):2283–2288, 2008.

[5] Matt Law, Joseph M. Luther, Qing Song, Barbara K. Hughes, Craig L. Perkins, and Arthur J. Nozik. Structural, optical, and electrical properties of PbSe nanocrystal solids treated thermally or with simple amines. *Journal of the American Chemical Society*, 130(18):5974–5985, 2008.

[6] Maksym V. Kovalenko, Marcus Scheele, and Dmitri V. Talapin. Colloidal nanocrystals with molecular metal chalcogenide surface ligands. *Science*, 324(5933):1417–1420, 2009.

[7] Angshuman Nag, Maksym V. Kovalenko, Jong-Soo Lee, Wenyong Liu, Boris Spokoyny, and Dmitri V. Talapin. Metal-free inorganic ligands for colloidal nanocrystals: S^{2-}, HS^{-}, Se^{2-}, HSe^{-}, Te^{2-}, HTe^{-}, TeS_3^{2-}, OH^{-}, and NH^{2-} as surface ligands. *Journal of the American Chemical Society*, 133(27):10612–10620, 2011.

[8] David J. Norris, Alexander L. Efros, and Steven C. Erwin. Doped nanocrystals. *Science*, 319(5871):1776–1779, 2008.

[9] F. Lacour, O. Guillois, X. Portier, H. Perez, N. Herlin, and C. Reynaud. Laser pyrolysis synthesis and characterization of luminescent silicon nanocrystals. *Physica E: Low-dimensional Systems and Nanostructures*, 38(12):11–15, 2007.

[10] P. E. Batson and J. R. Heath. Electron energy loss spectroscopy of single silicon nanocrystals: The conduction band. *Physical Review Letters*, 71(6):911–914, 1993.

[11] K. A. Littau, P. J. Szajowski, A. J. Muller, A. R. Kortan, and L. E. Brus. A luminescent silicon nanocrystal colloid via a high-temperature aerosol reaction. *The Journal of Physical Chemistry*, 97(6):1224–1230, 1993.

[12] L. T. Canham. Silicon quantum wire array fabrication by electrochemical and chemical dissolution of wafers. *Applied Physics Letters*, 57(10):1046–1048, 1990.

[13] A. G. Cullis and L. T. Canham. Visible light emission due to quantum size effects in highly porous crystalline silicon. 1991.

[14] L. Mangolini, E. Thimsen, and U. Kortshagen. High-yield plasma synthesis of luminescent silicon nanocrystals. *Nano Letters*, 5(4):655–659, 2005.

[15] L. Mangolini, D. Jurbergs, E. Rogojina, and U. Kortshagen. High efficiency photoluminescence from silicon nanocrystals prepared by plasma synthesis and organic surface passivation. *physica status solidi (c)*, 3(11):3975–3978, 2006.

[16] Z. C. Holman and U. R. Kortshagen. A flexible method for depositing dense nanocrystal thin films: Impaction of germanium nanocrystals. *Nanotechnology*, 21(33):335302, 2010.

[17] David Jurbergs, Elena Rogojina, Lorenzo Mangolini, and U. Kortshagen. Silicon nanocrystals with ensemble quantum yields exceeding 60%. *Applied Physics Letters*, 88(23):233116–233116–3, 2006.

[18] Kai-Yuan Cheng, Rebecca Anthony, Uwe R. Kortshagen, and Russell J. Holmes. High-efficiency silicon nanocrystal light-emitting devices. *Nano Letters*, 11(5):1952–1956, 2011.

[19] Philippe Guyot-Sionnest. Electrical transport in colloidal quantum dot films. *The Journal of Physical Chemistry Letters*, 3(9):1169–1175, 2012.

[20] Jillian M. Buriak. Organometallic chemistry on silicon and germanium surfaces. *Chemical reviews*, 102(5):1271–1308, 2002.

[21] Zachary C. Holman, Chin-Yi Liu, and Uwe R. Kortshagen. Germanium and silicon nanocrystal thin-film field-effect transistors from solution. *Nano Letters*, 10(7):2661–2666, 2010.

[22] Lance M. Wheeler, Nathan R. Neale, Ting Chen, and Uwe R. Kortshagen. Hypervalent surface interactions for colloidal stability and doping of silicon nanocrystals. *Nature Communications*, 4, 2013.

[23] David J. Rowe, Jong Seok Jeong, K. Andre Mkhoyan, and Uwe R. Kortshagen. Phosphorus-doped silicon nanocrystals exhibiting mid-infrared localized surface plasmon resonance. *Nano Letters*, 13(3):1317–1322, 2013.

[24] Heng Liu, Alexandre Pourret, and Philippe Guyot-Sionnest. Mott and Efros-Shklovskii variable range hopping in CdSe quantum dots films. *ACS Nano*, 4(9):5211–5216, 2010.

[25] Ting Chen, Brian Skinner, Wei Xie, B. I. Shklovskii, and Uwe R. Kortshagen. Carrier transport in films of alkyl-ligand-terminated silicon nanocrystals. *The Journal of Physical Chemistry C*, 118(34):19580–19588, 2014.

[26] Research and markets: Global quantum dots market in solid state lighting, solar cells and display applications market opportunities forecasts 2013 - 2018, 2014.

[27] Danil Vanmaekelbergh and Peter Liljeroth. Electron-conducting quantum dot solids: Novel materials based on colloidal semiconductor nanocrystals. *Chemical Society Reviews*, 34(4):299–312, 2005.

[28] X. D. Pi, R. W. Liptak, J. Deneen Nowak, N. P. Wells, C. B. Carter, S. A. Campbell, and U. Kortshagen. Air-stable full-visible-spectrum emission from silicon nanocrystals synthesized by an all-gas-phase plasma approach. *Nanotechnology*, 19(24):245603, 2008.

[29] Brian Skinner, Tianran Chen, and B. I. Shklovskii. Theory of hopping conduction in arrays of doped semiconductor nanocrystals. *Physical Review B*, 85(20):205316, 2012.

[30] F. Remacle, K. C. Beverly, J. R. Heath, and R. D. Levine. Gating the conductivity of arrays of metallic quantum dots. *The Journal of Physical Chemistry B*, 107(50):13892–13901, 2003.

[31] C. P. Collier, R. J. Saykally, J. J. Shiang, S. E. Henrichs, and J. R. Heath. Reversible tuning of silver quantum dot monolayers through the metal-insulator transition. *Science*, 277(5334):1978–1981, 1997.

[32] Yadong Yin and A. Paul Alivisatos. Colloidal nanocrystal synthesis and the organicinorganic interface. *Nature*, 437(7059):664–670, 2005.

[33] Franoise Remacle and Raphael D. Levine. Quantum dots as chemical building blocks: Elementary theoretical considerations. *ChemPhysChem*, 2(1):20–36, 2001.

[34] Louis Brus. Electronic wave functions in semiconductor clusters: Experiment and theory. *The Journal of Physical Chemistry*, 90(12):2555–2560, 1986.

[35] R. E. Chandler, A. J. Houtepen, J. Nelson, and D. Vanmaekelbergh. Electron transport in quantum dot solids: Monte Carlo simulations of the effects of shell filling, Coulomb repulsions, and site disorder. *Physical Review B*, 75(8):085325, 2007.

[36] Kittel, C. *Introduction to solid state physics*. Wiley, New York, 8th ed edition, 2004.

[37] Roger H. Terrill, Timothy A. Postlethwaite, Chun-hsien Chen, Chi-Duen Poon, Andreas Terzis, Aidi Chen, James E. Hutchison, Michael R. Clark, and George Wignall. Monolayers in three dimensions: NMR, SAXS, thermal, and electron hopping studies of alkanethiol stabilized gold clusters. *Journal of the American Chemical Society*, 117(50):12537–12548, 1995.

[38] W. Peter Wuelfing, Stephen J. Green, Jeremy J. Pietron, David E. Cliffel, and Royce W. Murray. Electronic conductivity of solid-state, mixed-valent, monolayer-protected Au clusters. *Journal of the American Chemical Society*, 122(46):11465–11472, 2000.

[39] Yao Liu, Markelle Gibbs, James Puthussery, Steven Gaik, Rachelle Ihly, Hugh W. Hillhouse, and Matt Law. Dependence of carrier mobility on nanocrystal size and ligand length in PbSe nanocrystal solids. *Nano letters*, 10(5):1960–1969, 2010.

[40] Dong Yu, Congjun Wang, and Philippe Guyot-Sionnest. N-type conducting CdSe nanocrystal solids. *Science*, 300(5623):1277–1280, 2003.

[41] Ji-Hyuk Choi, Aaron T. Fafarman, Soong Ju Oh, Dong-Kyun Ko, David K. Kim, Benjamin T. Diroll, Shin Muramoto, J. Greg Gillen, Christopher B. Murray, and Cherie R. Kagan. Bandlike transport in strongly coupled and doped quantum dot solids: A route to high-performance thin-film electronics. *Nano Letters*, 12(5):2631–2638, May 2012.

[42] Soong Ju Oh, Nathaniel E. Berry, Ji-Hyuk Choi, E. Ashley Gaulding, Hangfei Lin, Taejong Paik, Benjamin. T. Diroll, Shin Muramoto, Christopher B. Murray, and Cherie R. Kagan. Designing high-performance PbS and PbSe nanocrystal electronic devices through stepwise, post-synthesis, colloidal atomic layer deposition. *Nano Letters*, 14(3):1559–1566, 2014.

[43] William J. Baumgardner, Kevin Whitham, and Tobias Hanrath. Confined-but-connected quantum solids via controlled ligand displacement. *Nano Letters*, 13(7):3225–3231, 2013.

[44] James Clerk Maxwell. *A treatise on electricity and magnetism*, volume 1. Clarendon press, 1881.

[45] S.-H. Kim, G. Medeiros-Ribeiro, D. A. A. Ohlberg, R. Stanley Williams, and J. R. Heath. Individual and collective electronic properties of Ag nanocrystals. *The Journal of Physical Chemistry B*, 103(47):10341–10347, 1999.

[46] G. Medeiros-Ribeiro, D. A. A. Ohlberg, R. Stanley Williams, and James R. Heath. Rehybridization of electronic structure in compressed two-dimensional quantum dot superlattices. *Physical Review B*, 59(3):1633–1636, 1999.

[47] N.F. Mott. Introductory talk: Conduction in non-crystalline materials. *Journal of Non-Crystalline Solids*, 810:1–18, 1972.

[48] C. B. Murray, C. R. Kagan, and M. G. Bawendi. Synthesis and characterization of monodisperse nanocrystals and close-packed nanocrystal assemblies. *Annual Review of Materials Science*, 30(1):545–610, 2000.

[49] I. S. Beloborodov, A. V. Lopatin, V. M. Vinokur, and K. B. Efetov. Granular electronic systems. *Reviews of Modern Physics*, 79(2):469–518, 2007.

[50] Nevill Mott. Conduction in non-crystalline materials. *Oxford University Press(UK), 1993,*, page 157, 1993.

[51] Amir Zabet-Khosousi, Paul-Emile Trudeau, Yoshinori Suganuma, Al-Amin Dhirani, and Bryan Statt. Metal to insulator transition in films of molecularly linked gold nanoparticles. *Physical Review Letters*, 96(15):156403, 2006.

[52] K. C. Beverly, J. L. Sample, J. F. Sampaio, F. Remacle, J. R. Heath, and R. D. Levine. Quantum dot artificial solids: Understanding the static and dynamic role of size and packing disorder. *Proceedings of the National Academy of Sciences*, 99(suppl 2):6456–6459, 2002.

[53] Jong-Soo Lee, Maksym V. Kovalenko, Jing Huang, Dae Sung Chung, and Dmitri V. Talapin. Band-like transport, high electron mobility and high photoconductivity in all-inorganic nanocrystal arrays. *Nature Nanotechnology*, 6(6):348–352, June 2011.

[54] Dong Yu, Congjun Wang, Brian L. Wehrenberg, and Philippe Guyot-Sionnest.

Variable range hopping conduction in semiconductor nanocrystal solids. *Physical Review Letters*, 92(21):216802, 2004.

[55] B. I. Shklovskii and A. L. Efros. *Electronic properties of doped semiconductors*. Springer-Verlag, 1984.

[56] H. Moreira, Q. Yu, B. Nadal, B. Bresson, M. Rosticher, N. Lequeux, A. Zimmers, and H. Aubin. Electron cotunneling transport in gold nanocrystal arrays. *Physical review letters*, 107(17):176803, 2011.

[57] Brian L. Wehrenberg, Dong Yu, Jiasen Ma, and Philippe Guyot-Sionnest. Conduction in charged PbSe nanocrystal films. *The Journal of Physical Chemistry B*, 109(43):20192–20199, 2005.

[58] A. G. Zabrodskii. The Coulomb gap: The view of an experimenter. *Philosophical Magazine Part B*, 81(9):1131–1151, 2001.

[59] T. B. Tran, I. S. Beloborodov, Jingshi Hu, X. M. Lin, T. F. Rosenbaum, and H. M. Jaeger. Sequential tunneling and inelastic cotunneling in nanoparticle arrays. *Physical Review B*, 78(7):075437, 2008.

[60] Arjan J. Houtepen, Daan Kockmann, and Danil Vanmaekelbergh. Reappraisal of variable-range hopping in quantum-dot solids. *Nano letters*, 8(10):3516–3520, 2008.

[61] Praket P. Jha and Philippe Guyot-Sionnest. Photoluminescence switching of charged quantum dot films. *The Journal of Physical Chemistry C*, 111(42):15440–15445, 2007.

[62] Christopher R. Newman, C. Daniel Frisbie, Demetrio A. da Silva Filho, Jean-Luc Brdas, Paul C. Ewbank, and Kent R. Mann. Introduction to organic thin film transistors and design of n-channel organic semiconductors. *Chemistry of Materials*, 16(23):4436–4451, 2004.

[63] Yao Liu, Jason Tolentino, Markelle Gibbs, Rachelle Ihly, Craig L. Perkins, Yu Liu,

Nathan Crawford, John C. Hemminger, and Matt Law. PbSe quantum dot field-effect transistors mobilities above 7 cm^2 V^{-1} s^{-1}. *Nano Letters*, 13(4):1578–1587, 2013.

[64] Jrgen Ristein. Surface transfer doping of semiconductors. *Science*, 313(5790):1057–1058, 2006.

[65] Moonsub Shim and Philippe Guyot-Sionnest. N-type colloidal semiconductor nanocrystals. *Nature*, 407(6807):981–983, 2000.

[66] I. Yu, B. A. E. Ravich, and I. A. Smirnov. *Semiconducting lead chalcogenides*. Plenum Press: New York, 1970.

[67] Robert S. Allgaier and Wayne W. Scanlon. Mobility of electrons and holes in PbS, PbSe, and PbTe between room temperature and 4.2 K. *Physical Review*, 111(4):1029, 1958.

[68] U. Schlichting and K. H. Gobrecht. The mobility of free carriers in PbSe crystals. *Journal of Physics and Chemistry of Solids*, 34(4):753–758, 1973.

[69] E. M. Logothetis and H. Holloway. Compensation and ionized defect scattering in PbTe. *Solid State Communications*, 8(23):1937–1940, 1970.

[70] Barbara K. Hughes, Daniel A. Ruddy, Jeffrey L. Blackburn, Danielle K. Smith, Matthew R. Bergren, Arthur J. Nozik, Justin C. Johnson, and Matthew C. Beard. Control of PbSe quantum dot surface chemistry and photophysics using an alkylselenide ligand. *ACS nano*, 6(6):5498–5506, 2012.

[71] Soong Ju Oh, Nathaniel E. Berry, Ji-Hyuk Choi, E. Ashley Gaulding, Taejong Paik, Sung-Hoon Hong, Christopher B. Murray, and Cherie R. Kagan. Stoichiometric control of lead chalcogenide nanocrystal solids to enhance their electronic and optoelectronic device performance. *ACS Nano*, 7(3):2413–2421, 2013.

[72] David Mocatta, Guy Cohen, Jonathan Schattner, Oded Millo, Eran Rabani, and Uri Banin. Heavily doped semiconductor nanocrystal quantum dots. *Science*, 332(6025):77–81, 2011.

[73] Narayan Pradhan, David Goorskey, Jason Thessing, and Xiaogang Peng. An alternative of CdSe nanocrystal emitters: Pure and tunable impurity emissions in ZnSe nanocrystals. *Journal of the American Chemical Society*, 127(50):17586–17587, 2005.

[74] R. N. Bhargava, D. Gallagher, X. Hong, and A. Nurmikko. Optical properties of manganese-doped nanocrystals of ZnS. *Physical Review Letters*, 72(3):416–419, 1994.

[75] Cynthia A. Stowell, Robert J. Wiacek, Aaron E. Saunders, and Brian A. Korgel. Synthesis and characterization of dilute magnetic semiconductor manganese-doped indium arsenide nanocrystals. *Nano Letters*, 3(10):1441–1447, 2003.

[76] Victor I. Klimov. *Nanocrystal quantum dots*. CRC Press, 2010.

[77] Ayaskanta Sahu, Moon Sung Kang, Alexander Kompch, Christian Notthoff, Andrew W. Wills, Donna Deng, Markus Winterer, C. Daniel Frisbie, and David J. Norris. Electronic impurity doping in CdSe nanocrystals. *Nano Letters*, 12(5):2587–2594, 2012.

[78] Dong Hee Son, Steven M. Hughes, Yadong Yin, and A. Paul Alivisatos. Cation exchange reactions in ionic nanocrystals. *Science*, 306(5698):1009–1012, 2004.

[79] Richard D. Robinson, Bryce Sadtler, Denis O. Demchenko, Can K. Erdonmez, Lin-Wang Wang, and A. Paul Alivisatos. Spontaneous superlattice formation in nanorods through partial cation exchange. *Science*, 317(5836):355–358, 2007.

[80] X.D. Pi, R. Gresback, R. W. Liptak, S.A. Campbell, and U. Kortshagen. Doping efficiency, dopant location, and oxidation of Si nanocrystals. *Applied Physics Letters*, 92(12):123102, 2008.

[81] Ryan Gresback, Nicolaas J. Kramer, Yi Ding, Ting Chen, Uwe R. Kortshagen, and Tomohiro Nozaki. Controlled doping of silicon nanocrystals investigated by solution-processed field effect transistors. *ACS Nano*, 8(6):5650–5656, 2014.

[82] Makoto Hirasawa, Takaaki Orii, and Takafumi Seto. Size-dependent crystallization of Si nanoparticles. *Applied physics letters*, 88(9):093119, 2006.

[83] Uwe Kortshagen. Nonthermal plasma synthesis of semiconductor nanocrystals. *Journal of Physics D: Applied Physics*, 42(11):113001, 2009.

[84] Lorenzo Mangolini and Uwe Kortshagen. Selective nanoparticle heating: Another form of nonequilibrium in dusty plasmas. *Physical Review E*, 79(2):026405, 2009.

[85] N. J. Kramer, R. J. Anthony, M. Mamunuru, E. S. Aydil, and U. R. Kortshagen. Plasma-induced crystallization of silicon nanoparticles. *Journal of Physics D: Applied Physics*, 47(7):075202, 2014.

[86] Robert N. Carlile, Sam Geha, John F. OHanlon, and John C. Stewart. Electrostatic trapping of contamination particles in a process plasma environment. *Applied Physics Letters*, 59(10):1167–1169, 1991.

[87] U. Kortshagen and U. Bhandarkar. Modeling of particulate coagulation in low pressure plasmas. *Physical Review E*, 60(1):887–898, 1999.

[88] Seung J. Choi and Mark J. Kushner. The role of negative ions in the formation of particles in lowpressure plasmas. *Journal of Applied Physics*, 74(2):853–861, 1993.

[89] Soon Gu Kwon, Yuanzhe Piao, Jongnam Park, Subramanian Angappane, Younghun Jo, Nong-Moon Hwang, Je-Geun Park, and Taeghwan Hyeon. Kinetics of monodisperse iron oxide nanocrystal formation by heating-up process. *Journal of the American Chemical Society*, 129(41):12571–12584, 2007.

[90] Elena V. Shevchenko, Dmitri V. Talapin, Heimo Schnablegger, Andreas Kornowski, rjan Festin, Peter Svedlindh, Markus Haase, and Horst Weller. Study of nucleation and growth in the organometallic synthesis of magnetic alloy nanocrystals: The role of nucleation rate in size control of $CoPt_3$ nanocrystals. *Journal of the American Chemical Society*, 125(30):9090–9101, 2003.

[91] Rebecca J. Anthony, David J. Rowe, Matthias Stein, Jihua Yang, and Uwe Kortshagen. Routes to achieving high quantum yield luminescence from gas-phase-produced silicon nanocrystals. *Advanced Functional Materials*, 21(21):4042–4046, 2011.

[92] P. Scherrer. Estimation of the size and internal structure of colloidal particles by means of rntgen. *Nachr. Ges. Wiss. Gttingen*, 2:96–100, 1918.

[93] Holger Borchert, Elena V. Shevchenko, Aymeric Robert, Ivo Mekis, Andreas Kornowski, Gerhard Grbel, and Horst Weller. Determination of nanocrystal sizes: a comparison of TEM, SAXS, and XRD studies of highly monodisperse $CoPt_3$ particles. *Langmuir*, 21(5):1931–1936, 2005.

[94] Willem L. Vos, Rudolf Sprik, Alfons van Blaaderen, Arnout Imhof, Ad Lagendijk, and Gerard H. Wegdam. Strong effects of photonic band structures on the diffraction of colloidal crystals. *Physical Review B*, 53(24):16231–16235, 1996.

[95] I. Inan Tarhan and George H. Watson. Photonic band structure of fcc colloidal crystals. *Physical Review Letters*, 76(2):315–318, 1996.

[96] Dmitri V. Talapin, Elena V. Shevchenko, Maryna I. Bodnarchuk, Xingchen Ye, Jun Chen, and Christopher B. Murray. Quasicrystalline order in self-assembled binary nanoparticle superlattices. *Nature*, 461(7266):964–967, 2009.

[97] Elena V. Shevchenko, Dmitri V. Talapin, Nicholas A. Kotov, Stephen O'Brien, and Christopher B. Murray. Structural diversity in binary nanoparticle superlattices. *Nature*, 439(7072):55–59, 2006.

[98] Yixuan Yu, Christian A. Bosoy, Colin M. Hessel, Detlef-M. Smilgies, and Brian A. Korgel. Silicon nanocrystal superlattices. *ChemPhysChem*, 14(1):84–87, 2013.

[99] C. B. Murray, C. R. Kagan, and M. G. Bawendi. Self-organization of CdSe nanocrystallites into three-dimensional quantum dot superlattices. *Science*, 270(5240):1335–1338, 1995.

[100] B. L. V. Prasad, C. M. Sorensen, and Kenneth J. Klabunde. Gold nanoparticle superlattices. *Chemical Society Reviews*, 37(9):1871, 2008.

[101] Prashant V. Kamat. Quantum dot solar cells. Semiconductor nanocrystals as light harvesters. *The Journal of Physical Chemistry C*, 112(48):18737–18753, 2008.

[102] Vanessa Wood and Vladimir Bulovi. Colloidal quantum dot light-emitting devices. *Nano Reviews*, 1(0):1–7, 2010.

[103] Victor I. Klimov. *Semiconductor and metal nanocrystals: Synthesis and electronic and optical properties*. CRC Press, 2003.

[104] A. P. Alivisatos. Semiconductor clusters, nanocrystals, and quantum dots. *Science*, 271(5251):933–937, 1996.

[105] A. R. Stegner, R. N. Pereira, R. Lechner, K. Klein, H. Wiggers, M. Stutzmann, and M. S. Brandt. Doping efficiency in freestanding silicon nanocrystals from the gas phase: Phosphorus incorporation and defect-induced compensation. *Physical Review B*, 80(16):165326, 2009.

[106] Chin-Yi Liu, Zachary C. Holman, and Uwe R. Kortshagen. Hybrid solar cells from P3ht and silicon nanocrystals. *Nano Letters*, 9(1):449–452, 2009.

[107] Moon Sung Kang, Ayaskanta Sahu, David J. Norris, and C. Daniel Frisbie. Size- and temperature-dependent charge transport in PbSe nanocrystal thin films. *Nano Letters*, 11(9):3887–3892, 2011.

[108] T. A. Burr, A. A. Seraphin, E. Werwa, and K. D. Kolenbrander. Carrier transport in thin films of silicon nanoparticles. *Physical Review B*, 56(8):4818–4824, 1997.

[109] M. A. Rafiq, Y. Tsuchiya, H. Mizuta, S. Oda, Shigeyasu Uno, Z. A. K. Durrani, and W. I. Milne. Charge injection and trapping in silicon nanocrystals. *Applied Physics Letters*, 87(18):182101, 2005.

[110] M. A. Rafiq, Y. Tsuchiya, H. Mizuta, S. Oda, Shigeyasu Uno, Z. A. K. Durrani, and W. I. Milne. Hopping conduction in size-controlled Si nanocrystals. *Journal of Applied Physics*, 100(1):014303, 2006.

[111] R. N. Pereira, S. Niesar, W. B. You, A. F. da Cunha, N. Erhard, A. R. Stegner, H. Wiggers, M.-G. Willinger, M. Stutzmann, and M. S. Brandt. Solution-processed networks of silicon nanocrystals: The role of internanocrystal medium on semiconducting behavior. *The Journal of Physical Chemistry C*, 115(41):20120–20127, 2011.

[112] Neema Rastgar, David J. Rowe, Rebecca J. Anthony, Brian A. Merritt, Uwe R. Kortshagen, and Eray S. Aydil. Effects of water adsorption and surface oxidation

on the electrical conductivity of silicon nanocrystal films. *The Journal of Physical Chemistry C*, 117(8):4211–4218, 2013.

[113] Enrico Traversa. Ceramic sensors for humidity detection: The state-of-the-art and future developments. *Sensors and Actuators B: Chemical*, 23(23):135–156, 1995.

[114] J. Frenkel. On pre-breakdown phenomena in insulators and electronic semiconductors. *Physical Review*, 54(8):647, 1938.

[115] J. L. Hartke. The three-dimensional Poole-Frenkel effect. *Journal of Applied Physics*, 39(10):4871–4873, 1968.

[116] B. I. Shklovskii. Hopping conduction in semiconductors subjected to a strong electric field. *Sov. Phys. Semiconduct*, 6:1964, 1973.

[117] Jingshan Zhang and Boris I. Shklovskii. Density of states and conductivity of a granular metal or an array of quantum dots. *Physical Review B*, 70(11):115317, 2004.

[118] E. I. Levin, I. M. Ruzin, and B. I. Shklovskii. Transverse hopping conductivity of amorphous films in strong electric fields. *Sov. Phys. Semiconduct*, 22:401–408, 1988.

[119] L. Mangolini, D. Jurbergs, E. Rogojina, and U. Kortshagen. Plasma synthesis and liquid-phase surface passivation of brightly luminescent Si nanocrystals. *Journal of Luminescence*, 121(2):327–334, 2006.

[120] A. I. Ekimov, I. A. Kudryavtsev, M. G. Ivanov, and Al. L. Efros. Spectra and decay kinetics of radiative recombination in CdS microcrystals. *Journal of Luminescence*, 46(2):83–95, 1990.

[121] Al. L. Efros and M. Rosen. The electronic structure of semiconductor nanocrystals. *Annual Review of Materials Science*, 30(1):475–521, 2000.

[122] Ilan Gur, Neil A. Fromer, Michael L. Geier, and A. Paul Alivisatos. Air-stable all-inorganic nanocrystal solar cells processed from solution. *Science*, 310(5747):462–465, 2005.

[123] Edward H. Sargent. Infrared photovoltaics made by solution processing. *Nature Photonics*, 3(6):325–331, 2009.

[124] C. B. Murray, D. J. Norris, and M. G. Bawendi. Synthesis and characterization of nearly monodisperse CdE (E = sulfur, selenium, tellurium) semiconductor nanocrystallites. *Journal of the American Chemical Society*, 115(19):8706–8715, 1993.

[125] Congjun Wang, Moonsub Shim, and Philippe Guyot-Sionnest. Electrochromic nanocrystal quantum dots. *Science*, 291(5512):2390–2392, 2001.

[126] Andrew Shabaev, Alexander L. Efros, and Alexei L. Efros. Dark and photoconductivity in ordered array of nanocrystals. *Nano Letters*, 13(11):5454–5461, 2013.

[127] Marcus Scheele. To be or not to be: Band-like transport in quantum dot solids. *Zeitschrift fr Physikalische Chemie*, 229(1-2):167–178, 2015.

[128] N. F. Mott. Metal-insulator transition. *Reviews of Modern Physics*, 40(4):677–683, 1968.

[129] Michael E. Turk, Ji-Hyuk Choi, Soong Ju Oh, Aaron T. Fafarman, Benjamin T. Diroll, Christopher B. Murray, Cherie R. Kagan, and James M. Kikkawa. Gate-induced carrier delocalization in quantum dot field effect transistors. *Nano Letters*, 14(10):5948–5952, 2014.

[130] R. Mansfield. Impurity scattering in semiconductors. *Proceedings of the Physical Society. Section B*, 69(1):76, 1956.

[131] Matthieu Wyart. Marginal stability constrains force and pair distributions at random close packing. *Physical Review Letters*, 109(12):125502, September 2012.

[132] G. Masetti, Maurizio Severi, and Sandro Solmi. Modeling of carrier mobility against carrier concentration in arsenic-, phosphorus-, and boron-doped silicon. *IEEE Transactions on Electron Devices*, 30(7):764–769, 1983.

[133] John A. Glass Jr., Edward A. Wovchko, and John T. Yates Jr. Reaction of atomic hydrogen with hydrogenated porous silicon detection of precursor to silane formation. *Surface Science*, 348(3):325–334, 1996.

[134] Andrei G. Zabrodskii. Coulomb gap and metalinsulator transitions in doped semiconductors. *Physics-Uspekhi*, 41(7):722, 1998.

[135] William T. Doyle. The Clausius-Mossotti problem for cubic arrays of spheres. *Journal of Applied Physics*, 49(2):795–797, 1978.

[136] R. N. Pereira, D. J. Rowe, R. J. Anthony, and U. Kortshagen. Oxidation of freestanding silicon nanocrystals probed with electron spin resonance of interfacial dangling bonds. *Physical Review B*, 83(15):155327, 2011.

[137] C. Aharoni and F. C. Tompkins. Kinetics of adsorption and desorption and the Elovich equation. In Herman Pines and Paul B. Weisz D.D. Eley, editor, *Advances in Catalysis*, volume 21, pages 1–49. Academic Press, 1970.

[138] G. F. Cerofolini, D. Mascolo, and M. O. Vlad. A model for oxidation kinetics in air at room temperature of hydrogen-terminated (100) Si. *Journal of Applied Physics*, 100(5):054308, 2006.

[139] Lance Wheeler. Surface engineering of colloidal group IV nanocrystals for optoelectronics, 2014.

[140] John Robertson. Dopant states in a-Si: H. III. Triply coordinated boron. *Physical Review B*, 28(8):4666–4670, October 1983.

Appendix A

Copyright permissions

Chapter 3 was published open access in an American Chemical Society (ACS) journal. The ACS copyright policy states: "ACS extends blanket permission to students to include their theses and dissertations their own articles, or portions thereof, that have been published in ACS journals or submitted to ACS journals for publication, provided that the ACS copyright credit line is noted on the appropriate page(s)."